Synthesis and Physical Properties Study on Mixed Metal Oxynitrides

Minghui Yang

For the Degree of Doctor of Philosophy
School of Chemistry
University of Edinburgh

March 2010

Declaration

This work described in this thesis was carried out at the Department of Chemistry and Centre for Science at Extreme Conditions (CSEC), University of Edinburgh during the period September 2006 to March 2010. This thesis represents the author's original work, except where otherwise stated, and no part of it has been submitted for a degree at any other university. Prior to the submission of this thesis, some work has been published as described in the relevant chapters herein.

Minghui Yang

Acknowledgements

I would like to express my deepest thanks and respect to my supervisor, Professor John Paul Attfield, for his outstanding guidance, constant support, encouragement and extraordinary patient in the pass three and half years. Without him, I wouldn't have this great opportunity to work as a Ph.D student at the University of Edinburgh; I wouldn't be trained as a chemist; I wouldn't have the expectation to be a scientist for my career in my life. Second, I would like to express my heartfelt gratitude to Professor Amparo Fuertes, who led me into the oxynitride field, also give me guidance and support at all the stages of my research.

I would also like to thanks all the members of Attfield group, in particular, very deep thanks to Mark Senn and Alex Sinclair for their help, time and patience in correcting my thesis, also thank Tony and Wei-tin for teaching me GSAS, Jenny for teaching me to use the Walker press, Mark for the help with XRD, Alex for help with RME students. Thanks to all my friends in Edinburgh for a happy time during my study.

I am thankful to the Professors and lectures at the Department of Chemistry: Dr. Jan-Willem Bos, Dr. Serena Margadonna and Professor Simon Parsons who have helped me a lot during my Ph.D study. I am also greatly indebted to the post-docs in CSEC, Dimitry and Javier for illuminating instruction of the SQUID and PPMS. Additional thanks to Judith in Amparo's group in Spain, for the help with TEM. I acknowledge the research scientists in ISIS, Diamond and ILL for their help with neutron and synchrotron experiments. Thanks also to EaStChem for funding.

Lastly my thanks go to my beloved family for their loving considerations and great confidence in me all through these years. A special thanks to my wife, Xinyue, for all her support in the last three years and her love for life!

Abstract

Mixed metal oxynitrides have attracted attention due to their interesting chemical and physical properties in the past twenty years. In this thesis, four series of mixed metal oxynitrides have been investigated. The samples have been synthesized by both thermal ammonolysis and high pressure high temperature methods. The structural exploration covers perovskite, scheelite and pyrochlore types. The structural studies were carried out using powder X-ray and neutron diffraction, and magnetic and conducting properties have been explored.

A series of new $RZrO_2N$ (R = Pr, Nd and Sm) perovskites were synthesized using high pressure high temperature methods (HPHT) via a direct solid state reaction of R_2O_3 with Zr_2ON_2. All three new phases crystallize in the orthorhombic Pnma perovskite superstructure, and the structural distortion increases with decreasing R^{3+} ionic radius. $RZrO_2N$ contains both R^{3+} and d^0 Zr^{4+} and thus shows a potential for multiferroic properties.

$EuWO_{1-x}N_{2+x}$ perovskites with a wide range of nitrogen contents ($-0.16 \leq x \leq 0.46$) were synthesized by thermal ammonolysis of an oxide precursor $Eu_2W_2O_9$. Ferromagnetic ordering below a Curie temperature T_C =12 ± 1 K and negative colossal magnetoresistances (CMR) have been discovered in these samples. In particular, for the lowest doped sample, $EuWO_{0.96}N_{2.04}$, CMR ≥ 99.7% was observed at 7 K. The possibility of tuning the physical properties by altering the chemical composition has been demonstrated. A linear relationship between the lattice parameter and nitrogen content of $EuWO_{1+x}N_{2-x}$ was observed.

An investigation has been made of the Eu-Mo-O-N system. A new pyrochlore oxynitride series $Eu_2Mo_2O_{6-x}N_{2+2x/3}$ ($0.20 \leq x \leq 2.25$) was synthesized by

ammonolysis of $Eu_2Mo_2O_7$. A ferrimagnetic ordering and semiconducting behavior has been observed in these samples.

A detailed structural study of $SrMO_2N$ (M = Nb, Ta) has been performed using variable temperature neutron and electron diffraction. Partial anion order has been observed in both samples up to 750 ^oC. It is consistent with *cis*-ordering of the two nitrides in each MO_4N_2 octahedron. At low temperatures, this order directs the tilting of the octahedron to form a pseudo-tetragonal superstructure. It creates zig-zag MN chains in two or three dimensions within the lattice. This principle can be used to predict the local structures of perovskite-related oxynitrides $AMO_{3-x}N_x$.

Table of contents

Chapter 1. Introduction

1.1 Oxynitride materials

1.1.1 Nitrides and oxides

Nitrogen and oxygen have numerous similarities, such as their electronegativities, polarizabilities, ionic radii and coordinations in the solid state as summarized in Table 1.1.[1-4] Hence, they may substitute for each other, resulting in crystallographically similar structures. Oxide materials with partial oxygen substitution by nitrogen are known as oxynitrides. Many oxynitrides and nitrides have been observed to adopt the same structure as their oxide isomorphs, such as perovskite,[5] scheelite,[6] pyrochlore,[7] spinel,[8] etc. Despite these similarities, nitrogen and oxygen atoms also have distinct crystallochemical and electronic properties. Thus, such substitutions can strongly affect the properties of oxides due to the different charges and the resulting difference in the ionicity of the metal-anion bond. In addition, with combinations of particular cations, the nitrided materials can have useful physical properties.

Table 1.1 Crystallochemical and electronic properties of N and O.

	N	O
Charge (z)	-3	-2
Electronegativity	3.0	3.4
Atomic polarizability ($Å^3$)	1.10	0.80
Electron affinity ($A \rightarrow A^{z-}$, kJ/mol)	1736	601
Bond Energy A-A (kJ/mol)	941	498
Ionic radii (Å) (for CN=IV)	1.46	1.38
Coordination number (CN)	II-VIII	II-VIII

Nitrides are thermodynamically less stable than oxides due to the unfavorable electronic affinity of nitrogen and its strength of the triple bond in molecular nitrogen. Thus, the preparation of nitrides is relatively more difficult than that of oxides.[4, 9] High activation temperatures are often required, but metal to nitrogen bonds are also weakened by high temperatures. In order to use a moderate temperature to complete the synthesis, a long reaction time is often necessary. The approaches to the synthesis of nitrides and oxynitrides are often more complex. Due to development of synthetic methodology within the last two decades, transition metal oxynitrides have been investigated intensively due to their novel and useful physical and chemical properties.

1.1.2 Synthesis of oxynitrides

The conventional method for oxynitride synthesis is thermal ammonolysis, which can use a nitrogen source either from N_2 or NH_3. Due to the high bonding energy of the N to N triple bond, the application of N_2 in synthesis normally requires a very high activation energy.[10] In contrast, decomposition of NH_3 at moderate temperatures (above 300 ^oC) can be considered as an equilibrium of nitriding species (N, NH, NH_2) and molecular hydrogen.[11] In the ammonolysis of oxides, the formation of H_2O provides the thermodynamic driving force in the reaction, while nitrogen is introduced into the compounds through substitution. Hence, ammonia is the most commonly used nitriding reagent. The ammonolysis is normally carried out under ambient pressure in the temperature range 450 – 1200 ^oC.[12-18]

Due to the large difference in the free energies of formation between the binary rare earth oxides and nitrides, the ammonolytic syntheses of rare earth quaternary oxynitrides normally start with ternary oxides or highly reactive amorphous precursors.[12, 19] Other synthesis methods for quaternary oxynitrides are rarely

reported. For instance, $ATaO_2N$ and A_2TaO_3N (A = Sr and Ba) were synthesized by reacting TaON with alkaline earth oxides under nitrogen.[12] $NaTaO_{3-x}N_x$ was prepared by the reaction of $Ta_2O_{5-x}N_x$ and NaOH under hydrothermal conditions.[20] Nd_2AlO_3N was prepared by direct solid state reaction of AlN and Nd_2O_3.[21] $BaNbO_2N$ was prepared by the reaction of BaO_2 and NbN under a pressure of 5 GPa.[22]

1.1.3 Applications of oxynitrides

The most promising application of oxynitrides is probably as a photocatalyst in water splitting. Hydrogen is considered as the best available fuel since the consumption only produces water. However, conventional methods of producing hydrogen mainly rely on steam reforming or convertion from crude oil, making H_2 use less effective and more polluting than traditional energy sources. The activation of TiO_2 powders under UV light as a photocatalyst for splitting H_2O has been studied for many years,[23-25] and more recently other oxides, such as La-doped $NiO/NaTaO_3$ [26] and $RuO_2/CaIn_2O_4$,[27] have been reported. However, these oxide-based photocatalysts are restricted by their limited spectral range (wavelength $\lambda < 400$ nm). Searching for photocatalysts which can be activated by visible light ($400 < \lambda < 800$ nm) is receiving much attention in order to improve solar energy utilization.

The substitution of oxygen by nitrogen leads to more negative valence band levels and hence smaller band gaps than in conventional oxides. The nitrogen-doped TaO_2 system has been reported as a photocatalyst for water splitting under visible light.[28-30] Furthermore, several other series of oxynitrides have demonstrated a wider visible light absorption range than in TaON. For instance, $LaTiO_2N$ has been demonstrated to be a photocatalyst for water splitting up to 600 nm when combined with electron donors (methanol) or electron acceptors (Ag^+).[31] The most recent study shows $ATaO_2N$ (A = Ca, Sr, Ba) are photoactive for H_2 evolution in the presence of

methanol or I^- which act as electron donors.[32]

Conventional inorganic pigments often contain toxic elements and/or heavy metals, such as Cd, Cr, Pb, Sb, etc. Hence, the development of alternative non-toxic inorganic pigments has been an active field. Oxides are often black or colourless, but the substitution of oxygen by nitrogen, with lower electronegativity, alters the optical band gap in many materials. Thus, oxynitrides may show bright colours. In addition, they normally do not contain toxic elements,[33-35] which together with their chemical and thermal stability makes the oxynitrides good candidates for non-toxic inorganic pigments. For instance, the fluorite-type oxynitrides Zr-Ln-O-N (Ln = Eu, Er and Ce) are white, pink, orange or green,[36] respectively depending on the doping level, and $(Ga_{1-x}Zn_x)(N_{1-x}O_x)$ is yellowish in colour.[37] By varying the doping level of nitrogen, the colour of $Ta_{3-x}Zr_xN_{5-x}O_x$ can be shifted from red to yellow.[38] The solid solutions of $CaTaO_2N$ and $LaTaON_2$ with perovskite type structures have been suggested as non-toxic inorganic pigments.[39] Their colour can easily be tuned through the desired range from yellow to deep red, simply by adjusting the proportions of the two end-members. Other perovskite-related oxynitrides of ABO_2N (A = Ca^{2+}, Sr^{2+}, Ba^{2+} and B = Ta^{5+}, Nb^{5+}) show yellow, orange, ochre and black colours.[40]

The substitution of oxide O^{2-} by nitride N^{3-} leads to an increase of the cation oxidation states, hence altering the bonding and structure of oxynitrides. These changes can bring about interesting electronic and magnetic properties. For instance, $LaVO_{3-x}N_x$ shows increased electrical conductivity compared to $LaVO_3$ [41] and the thermoelectric properties of $SrMoO_{3-x}N_x$ can be modified by changing the nitrogen content.[42] $BaTaO_2N$ and $SrTaO_2N$ have been reported to exhibit an extremely high bulk dielectric permittivity. [15] Colossal magnetoresistance (CMR) was recently discovered in $EuNbO_2N$. [17]

1.2 Structure types

1.2.1 Perovskite

Perovskites have a general formula ABX_3.[43] The atomic arrangement in this structure was first observed for the mineral perovskite, $CaTiO_3$. The ideal structure has a primitive cubic unit cell with the A cation in the centre, surrounded by eight smaller B cations at the corners and twelve X anions at the midpoints of the cell edges. Each B cation is coordinated to six X anions, as shown in Figure 1.1. The undistorted cubic perovskite has a space group of $Pm\bar{3}m$. Many different substitutions can made for A, B and X as long as the overall oxidation state balance is maintained and efficient diagonal packing of the A and B cations is accompanied by the BXB packing along the edge of the unit cell.

Figure 1.1 Crystal structure of perovskite [43]

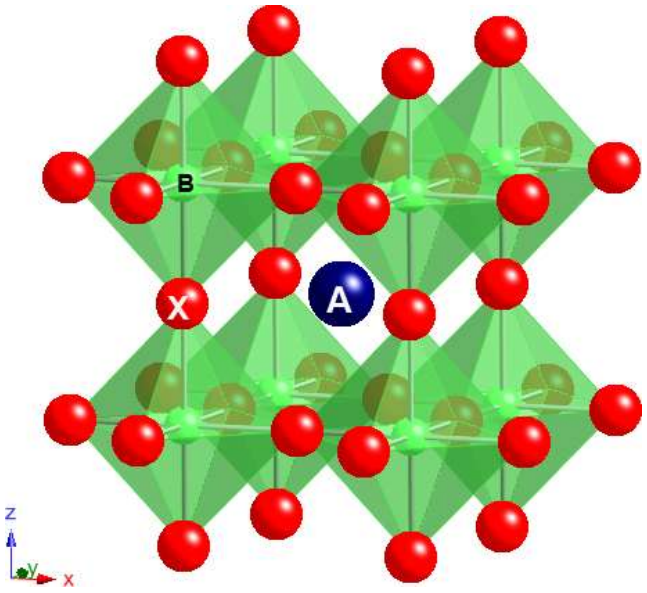

In the perovskite structure, the A cation is normally found to be larger than the B cation. In order to have contact between the cations and the X anions, $R_A + R_X$

should equal $\sqrt{2}(R_B+R_X)$, where R_A, R_B and R_x are the ionic radii. Structure distortions in perovskites were first studied by Goldschmidt in 1926,[44] who defined the tolerance factor, t, by the equation below:

$$t = \frac{R_A + R_x}{\sqrt{2}(R_B + R_x)} \qquad (1.1)$$

In the case of an ideal cubic perovskite, t should be equal to 1. The tolerance factor is a commonly used criterion for the stability of perovskites. At normal conditions, stable perovskites may have t values in the range $0.85 < t < 1.05$.[45] Lower values of t lead to lowering of the symmetry of the perovskite structure.

Most perovskite structures are distorted and do not have the ideal cubic symmetry.[46, 47] The degree of distortion often indicates the stability of the perovskite phase. Superstructures may be obtained by ordered tilts and rotations of the BX_6 octahedra. Jahn–Teller distortions may also be observed due to electronic degeneracies in the perovskite structure. For instance, $LnMnO_3$ (Ln = La, Nd, Sm, Eu and Gd) contain Mn^{3+} ions, which have a high-spin d^4 arrangement.[48] Thus, strong Jahn–Teller effects arise as an elongation of the MnO_6 octahedron.

Perovskites show high flexibility and a wide range of chemical and physical properties, not only owing to structure distortions, but also to defects and combinations of different cations and anions with a variety of oxidation states. Such distorted perovskites have reduced symmetry which may have important implications for their magnetic and electric properties.[49, 50] Notable perovskite properties are superconductivity in $YBa_2Cu_3O_{7-x}$,[51] colossal magnetoresistances in $La_{2/3}Sr_{1/3}MnO_3$,[52] $BaTiO_3$ ferroelectrics,[53] piezoelectric $Pb(ZrTi)O_3$ [54, 55] and multiferroic $BiFeO_3$.[56]

1.2.2 Pyrochlore

The fluorite structure has a general formula AX_2 and crystallises in the space group $Fm\bar{3}m$, where the A cations have 8-fold coordination in the fcc arrangement and X anions have 4-fold coordination and occupy the tetrahedral holes, as shown in Figure 1.2.[57]

Figure 1.2 Fluorite structure [57]

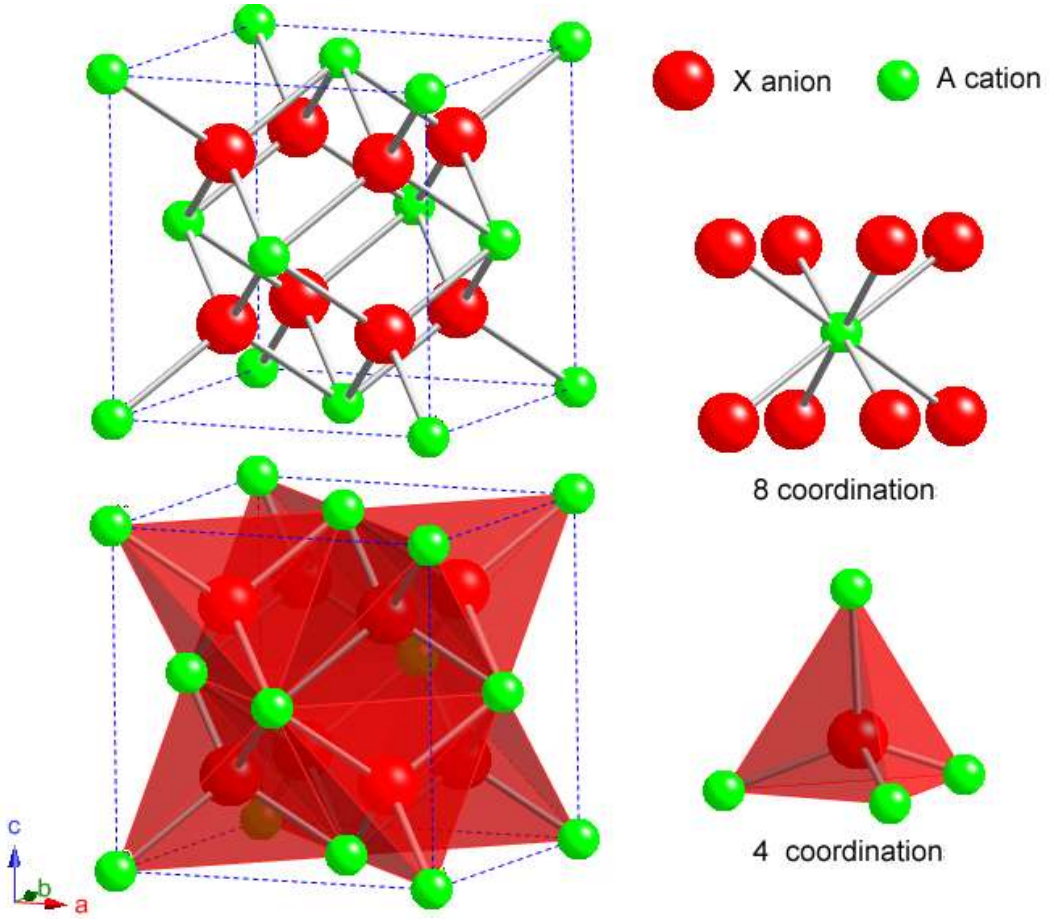

The pyrochlore structure is a fluorite-related crystal structure expressed in $Fd\bar{3}m$ symmetry. The $A_2B_2X_7$ pyrochlore structure is derived by A/B cation ordering and by introducing an anion vacancy into the fluorite structure, as shown in Figure 1.3. [58]

Figure 1.3 Schematic model of the pyrochlore structure showing A/B cation order and anion vacancy formation in a fluorite type sub-cell [58]

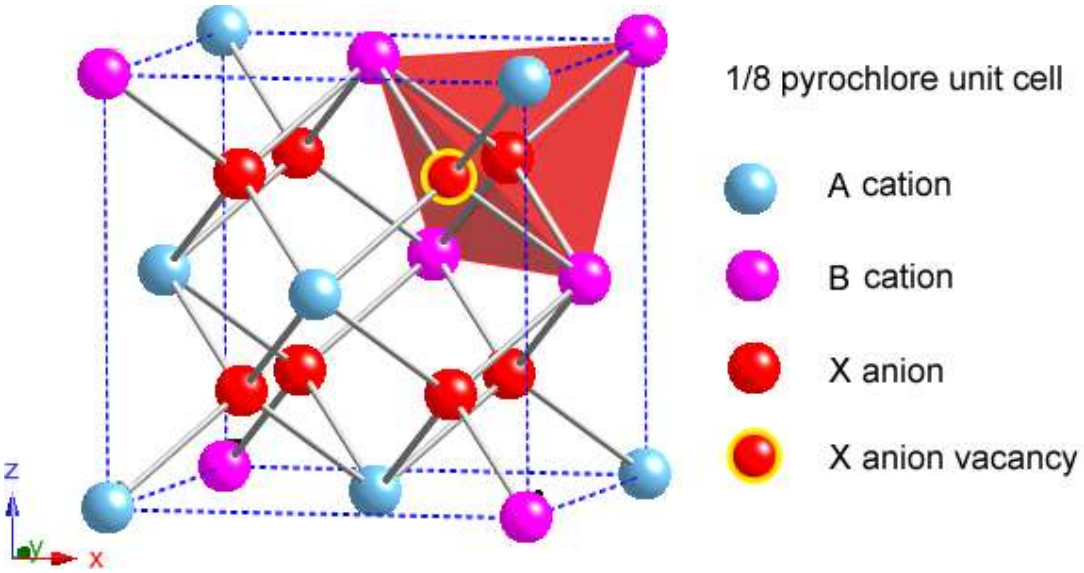

The general formula of pyrochlore is $A_2B_2X_y$, where y can range from 6 to 7, and A, B are two different cations, generally rare-earth or transition metals. Pyrochlores mainly contain two combinations of charges on the A and B sites, which are either (3+, 4+) or (2+, 5+). In the (3+, 4+) combination, A^{3+} can be a rare earth, Sc, Y, Bi, Tl or In, while B^{4+} can be a transition metal or heavy group IV elements.[58-60] In this thesis, $Eu_2Mo_2O_7$ [61] with Eu^{3+} (8-fold coordination) and Mo^{4+} (6-fold coordination) has been used as a parent pyrochlore oxide for ammonolysis. In the (2+, 5+) combination, A^{2+} can be Cd, Hg, Ca, Pb, Sn or Mn, while B^{5+} can be V, Nb, Ru, Rh, Ta, Re, Os, Ir, U or Sb.[58, 62, 63] In addition, a wide range of chemical substitutions and defects can be found at the A, B and X sites. Defect $A_2B_2O_6$ can be formed when A and B ions are highly polarizable but not very electropositive and the A-O or B-O bonds are strongly covalent, for instance $Tl_2B_2O_6$ (B = Nb, Ta and U). Due to their

high compositional diversity, structural flexibility and high anion vacancy concentrations, materials with the pyrochlore structure show a wide variety of chemical and physical properties. For instance, pyrochlores with A and B cations in their maximum oxidation states exhibit dielectric, piezo- and ferro-electric behaviour, e.g. $Cd_2Nb_2O_7$, $Cd_2Nb_2O_6S$ and $Ln_2Ti_2O_7$.[58] Pyrochlores with rare earth A cations and 3d transition metal B cations show interesting magnetic properties. A wide range of electrical properties has been reported,[64-68] e.g. ionic conductivity in $Gd_2Zr_2O_7$,[69,70] superconductivity in $Cd_2Re_2O_7$[71] and colossal magnetoresistances in $Tl_{2-x}Sc_xMn_2O_7$ ($0 \leq x \leq 0.5$). [72]

1.3 Magnetic and Conductivity Properties

1.3.1 Magnetic properties

Magnetic properties arise from the behaviour of electrons. In diamagnetic materials, all of the electrons are paired. Materials containing transition metals and lanthanides with unpaired d and f electrons exhibit paramagnetic behaviours.

The magnetic moment originates from both the spin momentum, S, and orbital angular momentum, L, of the unpaired electrons. The spin is intrinsic to the electrons. In comparison, the orbital angular momentum is strongly influenced by the local environment, and hence can be partially or completely ‘quenched’ by crystal field effects.

The magnetic moment of an atom is given by:

$$\mu = -g\mu_B J \qquad (1.2)$$

where, the ground state value is J = | L – S | when the shell is less than half full and J = L + S for when the shell is more than half full. g is the gyromagnetic ratio, defined by the Landé equation:

$$g = \frac{3J(J+1) + S(S+1) - L(L+1)}{2J(J+1)} \qquad (1.3)$$

μ_B is the Bohr magneton, which is given by:

$$\mu_B = \frac{eh}{4\pi m} \qquad (1.4)$$

where, e is the charge of electron, h is Planck's constant, and m is the mass of the electron.

1.3.2 Paramagnetism

The magnetic moments in paramagnetic materials are disordered. Under an external magnetic field, the disordered magnetic moments will be partly aligned parallel to the field. The magnetization of a material (M) in response to an external magnetic field (H) is defined by the magnetic susceptibility χ, which is given as: [73]

$$\chi = \frac{M}{H} \qquad (1.5)$$

In this thesis, χ is in molar units.

The χ values behave very differently for various materials as observed by their temperature and field dependencies. In general, diamagnetic materials have small and slightly negative χ, due to the realignment of electron orbitals due to the perturbation by the applied field. For many paramagnetic materials, where there is no interaction between adjacent spins, the relationship between χ and temperature is given by the Curie Law.[74]

$$\chi = \frac{C}{T} \qquad (1.6)$$

where C is the Curie constant and is given by:

$$C = \frac{N\mu_B{}^2\mu_{eff}{}^2}{3k_B} \qquad (1.7)$$

where N is the Avagadro number, μ_B is the Bohr magneton, k_B is Boltzmann's constant and μ_{eff} is the effective magnetic moment, given by:

$$\mu_{eff} = g\mu_B\sqrt{J(J+1)} \qquad (1.8)$$

For the first series of transition metal ions, the orbital angular momentum is often quenched (L = 0) and g = 2. Hence, Equation 1.8 can be converted to the spin only effective moment formula as below:

$$\mu_{eff} = 2\mu_B\sqrt{S(S+1)} \qquad (1.9)$$

where S is the spin quantum number.

For ferromagnetic and antiferromagnetic materials, there are interactions between adjacent spins. The high temperature paramagnetic region of ferromagnetic and antiferromagnetic materials is described by the Curie-Weiss Law: [75]

$$\chi = \frac{C}{T - \theta} \qquad (1.10)$$

where θ is the Weiss constant. The θ values depend on the dominant interaction between paramagnetic species, as shown in Figure 1.4.

Figure 1.4 Temperature dependent behaviors of (a) susceptibility and (b) inverse susceptibility for different types of magnetic materials.[75]

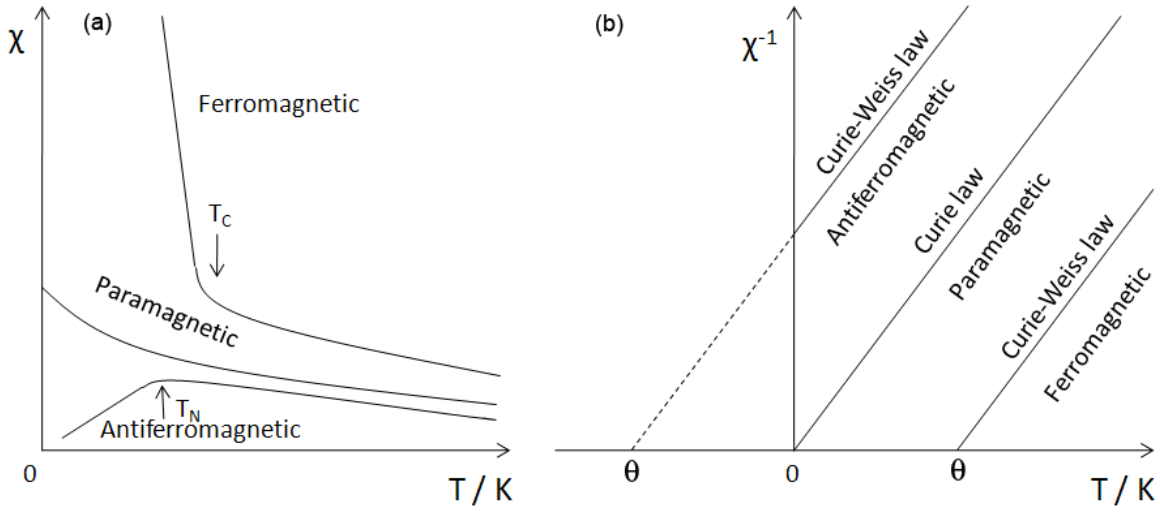

1.3.3 Magnetic ordering

A magnetic ordering may occur if the energy of interaction between magnetic moments is comparable to the thermal energy. For ferromagnetic materials, all the spins are aligned parallel below a transition temperature, also known as the Curie temperature T_C. Hence below T_C, ferromagnetic materials have long range ferromagnetic order, and show a decrease in the susceptibility as temperature

increases. For antiferromagnetic materials, the spins are aligned antiparallel below a transition temperature known as the Néel temperature T_N. Hence below T_N, antiferromagnetic materials have overall zero magnetic moment, and show an increase in the susceptibility as temperature increases. In the case of antiparallel alignment, if the spins are unequal either in number or size, then a net magnetic moment results, which is known as ferrimagnetism. In some disordered and frustrated magnets, spins may freeze in random orientations with short range magnetic order in a spin glass.

1.3.4 Magnetic hysteresis

The hysteresis properties of ferromagnets result from the formation of macroscopic magnetic domains and their reorientation in an applied field. Hysteresis properties are derived from the relationship between magnetization M and applied field H. As shown in Figure 1.5, magnetization reaches the maximum at a high applied field. The saturated magnetization is M_{sat}. As the applied field H is decreased to zero, the magnetization does not go to zero, instead it has a residual value, which is called the remnant magnetization M_r. The M_r needs an opposite field, which is known as the coercive field $-H_c$ to be applied if the magnetization is to be returned to zero. The whole cycle of a process from positive to a negative applied field, forms a hysteresis loop. The area inside the loop is the energy loss per unit per cycle. Hard magnets have a large area and soft magnets have small area in the hysteresis loop.

Figure 1.5 Hysteresis loop in a ferromagnetic material.

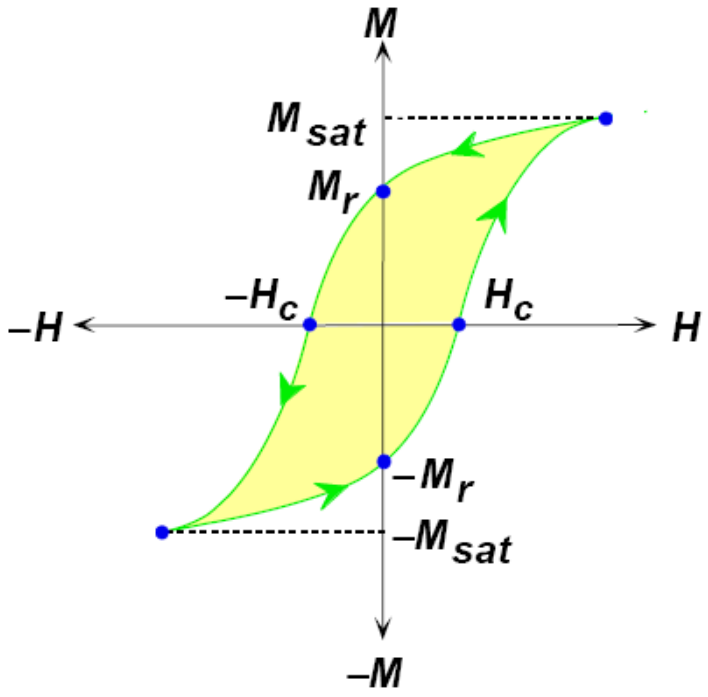

1.3.5 Conductivity

The transport of electrons through a material is defined as electronic conductivity. Conductivity σ is related to the density, charge and mobility of charge carriers according to:

$$\sigma = ne\mu \qquad (1.11)$$

where, n is the number of carriers per unit, e is the electron charge, and μ is the carrier mobility. Thus, highly conductive materials have a high concentration of charge carriers which are highly mobile. The inverse of conductivity is resistivity ρ, defined as:

$$\rho = \frac{1}{\sigma} \qquad (1.12)$$

Crystalline materials exhibit a very wide range of electrical conductivity. Materials are classified according to the electrical conductivity from low to high as insulator, semiconductor or metal. The conductivities of these different types have different temperature dependences, as shown in Figure 1.6. A superconductor behaves like a metal above a certain critical temperature (T_c), but below T_c the material enters a superconducting state in which the resistivity drops to zero.

Figure 1.6 Temperature dependence of conductivity and resistivity

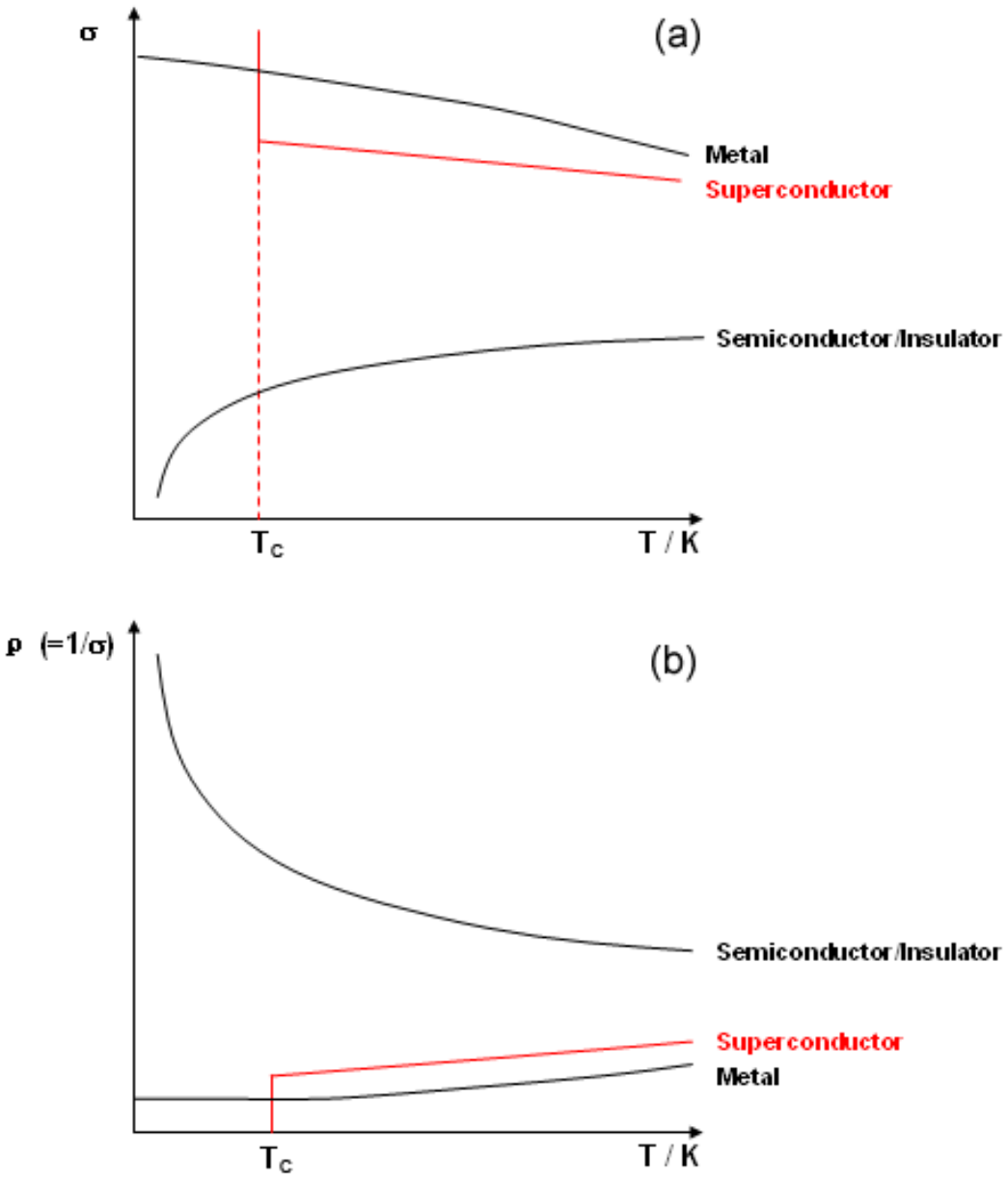

1.3.6 Band theory

The properties of different conductors are explained by Band theory. The outer-shell electrons of atoms in solid materials form energy bands. The completely filled band with lowest energy is the valence band. The band above the valence band is referred to as the conduction band. The energy difference E_g between the valence and conduction bands is the band gap. A current of electrons cannot pass through the valence band as it is filled. However, they can pass through the conduction band due to the empty states. For a metal, the band is partially filled, or commonly the conduction band overlaps with the valence band, thus, metals are good conductors. A semiconductor has an empty conduction band, however the band gap is small. With some additional energy, such as thermal energy, the electrons can be promoted from the valence band to the conduction band. Hence, a current can pass through a semiconductor. The presence of dopants in a semiconductor can also increase its conductivity. By contrast, an insulator has an empty conduction band with a large band gap, and thus has a low conductivity. The Fermi level lies between the bottom of the conduction band and the top of the valence band as shown in Figure 1.7. [76]

Figure 1.7 Schematic energy bands of solid materials [76]

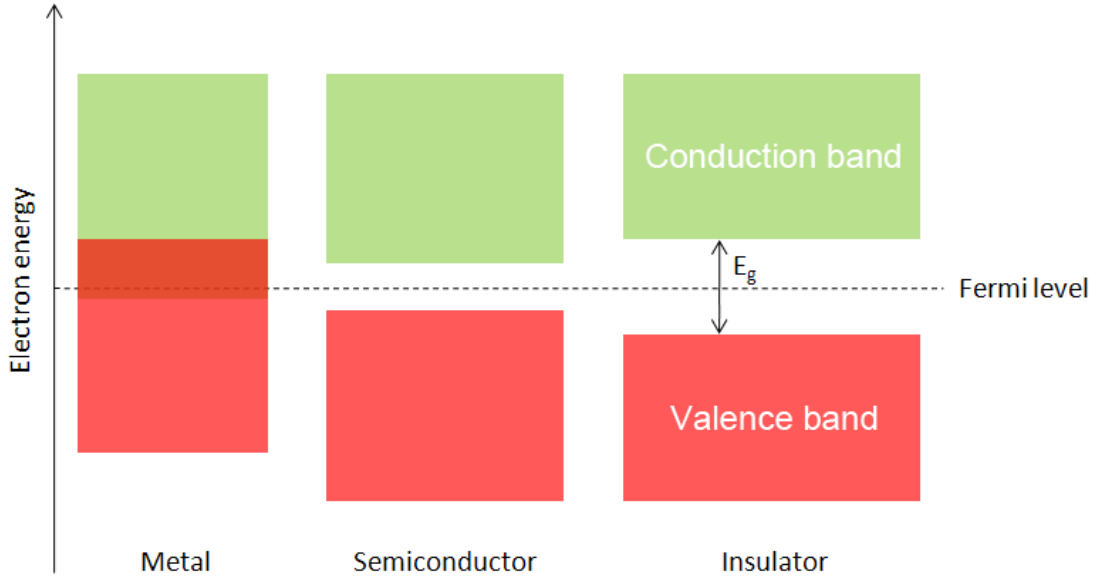

For metals, the number of charge carriers is essentially constant. The resistivity arises from the electron scattering by lattice vibrations and defects. As the temperature increases, the lattice vibrations increase, thus resistivity increases. In contrast, for semiconductors and insulators, the number of mobile carriers is small. As the temperature increases, more electrons can be promoted from the valence band to the conduction band. Thus, the conductivity increases with temperature as the number of carriers increases. The band gap E_g of an intrinsic semiconductor can be determined according to:

$$\sigma = \sigma_0 \cdot \exp(\frac{-E_g}{2k_B T}) \qquad (1.13)$$

where σ is the conductivity at temperature T, σ_0 is a constant for the material and k_B is the Boltzmann constant.

1.3.7 Magnetoresistance

Magnetoresistance (MR) is a phenomenon where electrical resistivity changes in response to an external magnetic field, defined as:

$$MR = \frac{\rho_H - \rho_0}{\rho_0} \qquad (1.14)$$

where ρ_0 is the resistance without a field and ρ_H is the resistance in field.

MR materials have been widely used in memory and sensor technologies. Magnetoresistance in conventional materials is only a few percent. Materials with large magnetoresistance (up to 40%) also known as Giant Magnetoresistance (GMR),

were synthesized with artificial ferromagnetic and nonmagnetic multilayers or heterogeneous materials. For instance, GMR was first observed in Fe-Cr multilayers in 1988, [77] and later in Cu-Co multilayers and heterogeneous alloys.[78] In these GMR materials, a thin layer of nonmagnetic material is 'sandwich' packed between two layers of magnetic materials. When a current passes through the GMR materials with an external magnetic field applied, the spins in ferromagnetic layers are aligned parallel. Hence, the up-spin electrons experience a small resistance and the down-spin electrons experience a large resistance. The net resistance is given by:

$$R_{para} = \frac{2R_{\downarrow} \cdot R_{\uparrow}}{R_{\downarrow} + R_{\uparrow}} \qquad (1.15)$$

When a current passes through GMR materials without an external magnetic field, the spins in ferromagnetic layers are aligned antiparallel due to weak antiferromagnetic coupling between layers. Hence, both up and down spin electrons experience a small resistance in one layer and a large resistance in the other layer. The total resistance is given by:

$$R_{antpara} = \frac{1}{2}(R_{\downarrow} + R_{\uparrow}) \qquad (1.16)$$

The overall difference in resistance, ΔR is equal to:

$$\Delta R = R_{para} - R_{antipara} = -\frac{(R_{\uparrow} - R_{\downarrow})^2}{2(R_{\uparrow} + R_{\downarrow})} \qquad (1.17)$$

In 1990s, Colossal Magnetoresistance (CMR) with changes in resistance >99%, associated with a ferromagnetic-to-paramagnetic phase transition were discovered.[79-80] CMR has potential for applications due to the very large response.

CMR was first observed in perovskite related materials, such as $La_{2/3}Ba_{1/3}MnO_x$ thin films.[79] Subsequently, many $T_{1-x}D_xMnO_3$ (T = trivalent lanthanide cation and D = divalent alkaline-earth cation) systems have been explored.[80] Other CMR systems, for example pyrochlores $Tl_{2-x}Sc_xMn_2O_7$ ($0 \leq x \leq 0.5$) [81] and spinels ACr_2Ch_4 (A = Fe, Cu, Cd and Ch = S, Se, Te) [82] have been reported. These effects are only observed at low temperatures and high magnetic fields. Several theories for CMR have been proposed but a single general model is not yet available.[83-88]

1.4 References

1. G. P. Pearson, *Inorg. Chem.* 1991, 30, 2856.
2. Encyclopedia of Materials; Elsevier: Amsterdam, 2001; Vol. 7, 6161.
3. R. D. Shannon, *Acta Crystallogr. A* 1976, 32, 751.
4. S. G. Ebbinghaus, H. P. Abicht, R. Dronskowski, T. Müller, A. Reller and A. Weidenkaff, *Prog. Solid State Chem.* 2009, 37, 173.
5. R. Marchand, F. Pors, Y. Laurent, *Rev. Int. Hautes Temp. Refract.*1986, 23, 11.
6. P. Antoine, R.Marchand, Y. Laurent, *Rev. Int. Hautes Temp. Refract.* 1987, 24, 43.
7. G. M.Veith, M. Greenblatt, M. Croft, J. B. Goodenough, *Mat. Res. Bull.* 2001, 36, 1521.
8. J. Grins, P. O. Käll, G. Svensson. *J. Solid State Chem.* 1995, 117, 48.
9. A. Hellwig and A. Hendry, *J Mater Sci.* 1994, 29, 4686.
10. R. Marchanda, Y. Laurenta, J. Guyadera, P. L'Haridona and P. Verdiera, *J. Eur. Ceram. Soc.* 1991, 8, 197.
11. A. Hellwig and A. Hendry, *J. Mater. Sci.* 1994, 29, 4686.
12. S. J. Clarke, B. P. Guinot, C. W. Michie, M. J. C. Calmont and M. J. Rosseinsky, *Chem. Mater.* 2002, 14, 288.
13. I. D. Fawcett, K. V. Ramanujachary and M. Greenblatt, *Mater. Res. Bull.* 1997, 32, 1565.
14. J. Grins and G. Svensson, *Mater. Res. Bull.* 1994, 29, 801.
15. Y. Kim, P. M.Woodward, P. M., K. Z. Baba-Kishi, C. W. Tai. *Chem. Mater.* 2004, 16, 1267.
16. G. Tobías, J. Oró-Solé, D. Beltrán-Porter, A. Fuertes, *Inorg. Chem.* 2001, 40, 6867.
17. A. B. Jorge, J. Oró-Solé, A. M. Bea, N. Mufti, T. T. M. Palstra, J. A. Rodgers, J. P. Attfield and A. Fuertes, *J. Am. Chem. Soc.* 2008, 130, 12572.
18. A. B. Jorge, J. Fraxedas, A. Cantarero, A. J. Williams, J. Rodgers, J. P. Attfield and A. Fuertes, *Chem. Mater.* 2008, 20, 1628.

19. S. H. Elder, F. J. Di Salvo, L. Topor, A. Navrotsky. *Chem. Mater*. 1993, 5, 1545.

20. H. Fu, S. Zhang, L. Zhang and Y. Zhu, *Mater. Res. Bull.* 2008, 43, 864.

21. R. Marchand, R. Pastuszak and Y. Laurent, *Rev. Chim. Minér.* 1982, 19, 684.

22. I. O. Troyanchuk, N. V. Kasper, O. S. Mantytskaya and E. F. Shapovalova, *Mater. Res. Bull.* 1995, 30, 421.

23. A, Fujishima and K. Honda, *Nature* 1972, 37, 238.

24. A. J. Bard, *Science* 1980,207, 139.

25. A. M. Linsebigler, L. Gungquan and J. T. Yates, *Chem. Rev.* 1995, 95, 735.

26. A. Kudo and H. Kato, *Chem. Phys. Lett.* 2000, 331, 373.

27. Y. Inoue, *Energy Environ. Sci.* 2009, 2, 364.

28. R. Nakamura, T. Tanaka, Y. Nakato, *J. Phys. Chem. B* 2004, 108, 10617.

29. G. Hitoki, T. Takata, J. N. Kondo, M. Hara, H. Kobayashi, K. Domen, *Chem. Commun.* 2002, 1698.

30. W.-J. Chun, A. Ishikawa, H. Fujisawa, T. Takata, J. N. Kondo, M. Hara, M. Kawai, Y. Matsumoto, K. Domen, *J. Phys. Chem. B* 2003, 107, 1798.

31. A. Kasahara, K. Nukumizu, G. Hitoki, T. Takata, J. N. Kondo, M. Hara, H. Kobayashi, K. Domen, *J. Phys. Chem. A* 2002, 106, 6750.

32. M. Higashi, R. Abe, T. Takata and K. Domen, *Chem. Mater.* 2009, 21, 1543.

33. J. Grins and G. Svensson, *Mater. Res. Bull.* 1994, 29, 801.

34. R. Marchand, F. Pors and Y. Laurent, *Ann. Chim. Fr.* 1991, 16, 553.

35. F. Tessier and R. Marchand, *J .Solid. State. Chem.* 2003, 171, 143.

36. M. Pérez-Estébanez, R. Pastrana-Fábregas, J. Isasi-Marín and R. Sáez-Puche, *J. Mater. Res.* 2006, 21, 1427.

37. K. Maeda, T. Takata, M. Hara, N. Saito, Y. Inoue and H. Kobayashi, *J. Am. Chem. Soc.* 2005, 127, 8286.

38. E. Guenther and M. Jansen, *Mater. Res. Bull.* 2001, 36, 1399.

39. M. Jansen and H. P. Letschert, *Nature* 2000, 404, 980.

40. A. Rachel, S. G. Ebbinghaus, M. Güngerich, P. J. Klar, J. Hanss and A.

Weindenkaff, *Thermochim. Acta.* 2005, 438, 134.

41. P. Antoine, R. Assabaa, P. L'Haridon, R. Marchand, Y. Laurent and C. Michel, *Mater. Sci. Eng.* 1989, B 5, 43.
42. I. C. Lekshmi, A. Gayen and M. S. Hegde, *Mater. Res. Bull.* 2005, 40, 93.
43. R. H. Mitchell, *Perovskites: Modern and Ancient*, Almaz Press Inc., Ontario 2002.
44. V. M. Goldschmidt, Skrifer Norske Videnskaps-Akad. Oslo, I. Mat.-Nat. Kl. 8 (1926).
45. C. Li, K. K. S. Chi and Ping Wu, *J. Alloy. Compd.* 2004, 372, 1, 40.
46. K. Terakura, *Prog. Mater. Sci.* 2007, 52, 2, 388.
47. M. A. Peña and J. L. G. Fierro, *Chem. Rev.* 2001, 101, 1981.
48. T. Mori, N. Kamegashira, K. Aoki, T. Shishido and T. Fukuda, *Mater. Lett.* 2002, 54, 238.
49. S. Hayashi, R. Aoki and T. Nakamur, *Mater. Res. Bull.* 1979, 14, 409.
50. H. Taguchi, *J. Solid State Chem.* 1995, 118, 367.
51. J. G. Bednorz and K. A. Mueller, *Z. Phys.* 1986, B64, 189.
52. S. Jin, *Science* 1994, 264, 414.
53. A. Benziada-Taibi, J. Ravez and P. Hagenmuller, *J. Fluorine Chem.* 1984, 26, 395.
54. M. Yamamoto, Y. Sasaki, A. Ochi, T. Inoue and S. Hamamura, *Jpn. J. Appl. Phys.* 2001, 40, 3637.
55. G. Ivensky, I. Zafrany and S. Ben-Yaakov, *IEEE Trans. Power Electron.* 2002, 17, 1049.
56. Y. Tokunaga, N. Furukawa, H. Sakai, Y. Taguchi, T-H Arima and Yoshinori Tokura, *Nature Mater.* 2009, 8, 558.
57. L. E. Smart and E. A. Moore, *Solid State Chemistry: An Introduction, 3rd* edition, Taylor & Francis Group, London, 2005.
58. M. A. Subramanian, G. Aravamudan and G. V. Subba Rao, *Prog. in Solid State*

Chem. 1983, 15, 55.

59. R. D. Shannon and A. W. Sleight, *Inorg. Chem.* 1972, 7, 1649.
60. R. A. McCauley, *J. Appl. Phys.* 1980, 51, 290.
61. G. J. McCarthy, *Mater. Res. Bull.* 1971, 6, 31.
62. G. V. Bazuev, O. V. Makarova and G. V. Shveikin, *Russ. J. Inorg. Chem.* 1978, 23, 345.
63. J. E. Greedan, *Mater. Res. Bull.* 1979, 14, 13.
64. O. Porat, C. Heremans, and H. L. Tuller, *Solid State Ionics* 1997, 94, 75.
65. E. V. Tsipis, V. V. Kharton, and J. R. Frade, *J. Eur. Ceram. Soc.* 2005, 25, 2623.
66. S. A. Kramer and H. L. Tuller, *Solid State Ionics* 1995, 82, 15.
67. B. J. Wuensch, K. W. Eberman, C. Heremans, E. M. Ku, P. Onnerud, E. M. E. Yeo, S. M. Haile, J. K. Stalick, J. D. Jorgensen, *Solid State Ionics* 2000, 129, 111.
68. A. V. Shlyakhtina, I. V. Kolbanev, A. V. Knotko, M. V. Boguslavskii, S. Yu. Stefanovich, O. K. Karyagina, L. G. Shcherbakova, *Inorg. Mater.* 2005, 41, 854.
69. J. A. Díaz-Guillén, M. R. Díaz-Guillén, J. M. Almanza, A. F. Fuentes, J. Santamaría, C. León, *J. Phys. -Condes. Matter* 2007, 19, 356212.
70. J. A. Díaz-Guillén, M. R. Díaz-Guillén, K. P. Padmasree, J. M. Almanza, A. F. Fuentes, J. Santamaría, C. León, *Bol. Soc. Esp. Ceram.* 2008, 47, 159.
71. K. Yoshimura, H. Sakaia, H. Ohnoa, S. Kambeb,R. E. Walstedtb, *Physica B: Condensed Matter* 2003, 329, 1319.
72. S. K. Kwon, J. H. Park and B. I. Min, *Physica B: Condensed Matter* 2000, 281, 1, 528.
73. John Crangle, *Solid State Magnetism*, Edward Arnold, 1991.
74. P. Curie, *Ann. Chem. Phys.* 1895, 5, 289.
75. A. R. West, *Basic Solid State Chemistry*, John Wiley and Sons, Chichester, 1999.
76. http://en.wikipedia.org/wiki/Electronic_band_structure
77. M. N. Baibich, J. M. Broto, A. Fert, F. Nguyen, Van Dau, F. Petroff, P. Eitenne, G. Creuzet, A. Friederich and J. Chazelas, *Phys. Rev. Lett*. 1988, 61, 2472.

78. A. E. Berkowitz, J. R. Mitchell, M. J. Carey, A. P. Young, S. Zhang, F. E. Spada, F. T. Parker, A. Hutten and G. Thomas, *Phys. Rev. Lett*. 1992, 68, 3745.

79. R. von Helmolt, J. Wecker, B. Holzapfel, L. Schultz, and K. Samwer, *Phys. Rev. Lett.* 1993, 71, 2331.

80. A. P. Ramirez, *J.Phys: Condens. Matter* 1997, 9, 8171.

81. Y. Shimakawa Y. kubo and T. Manako, *Nature* 1996, 268, 387.

82. A. P. Ramirez, R. J. Cava and J. Krajewski, *Nature* 1997, 268, 387.

83. C. Zener, *Phys. Rev.* 1951, 81, 440.

84. P. W. Anderson and H. Hasegawa, *Phys. Rev.* 1955, 100, 675.

85. D. Gennes *Phys. Rev.* 1960, 118, 141.

86. A .J. Millis, B. I. Shraiman and R. Mueller *Phys. Rev. Lett.* 1996, 77, 175.

87. J. R. Fletcher and K. W. H. Stephens *J. Phys. C: Solid State Phys.* 1969, 2, 444.

88. A. J. Millis, P. B. Littlewood and B. I. Shraiman, *Phys. Rev. Lett.* 1955, 74, 5144.

Chapter 2. Methodology and Techniques

2.1 Synthesis methods

Samples were prepared by using ceramic, ammonolysis and high pressure solid state synthesis. These methodologies and techniques are introducted below. The detailed synthesis conditions for different samples will be given in the following chapters.

2.1.1 Ceramic synthesis

Metal oxides were pre-heated at 800 ℃ overnight to remove any moisture or carbonates. High purity metal and metal oxide mixtures in stoichiometric ratios were finely ground using an agate pestle and mortar. In order to improve particle contact during the reaction, a powder mixture with high homogeneity was pelletized with a cylindrical pelletizer under loads up to 10 tonnes. High temperatures were employed to facilitate interparticle diffusion. To improve the sample homogeneity, the synthesis process was normally repeated several times.

High temperatures were achieved by using box or tube furnaces, which allow temperatures up to 1600 ℃. Reactions which are air sensitive, were done by using tube furnaces under flowing argon. The sintered pellets were finely powdered and checked by powder x-ray diffraction at each stage.

2.1.2 Ammonolysis

Powdered oxide precursors were placed in an alumina boat in a tube furnace for ammonolysis. Nitrogen gas (Oxygen-free, BOC) was passed over the sample for 15 min to expel air before the flow of ammonia gas (99.999%, BOC) was started. The sample was heated to the reaction temperature at a rate of 150 to 300 ℃/hr and furnace cooled after treatment. Sintered pellets were prepared for resistivity measurements by heating compressed powders of ammonolysis phase at specific conditions (details in Chapters) under ammonia gas. The outcoming ammonia was neutralized by ~50mol% acetic acid solution.

Figure 2.1 Ammonolysis setup

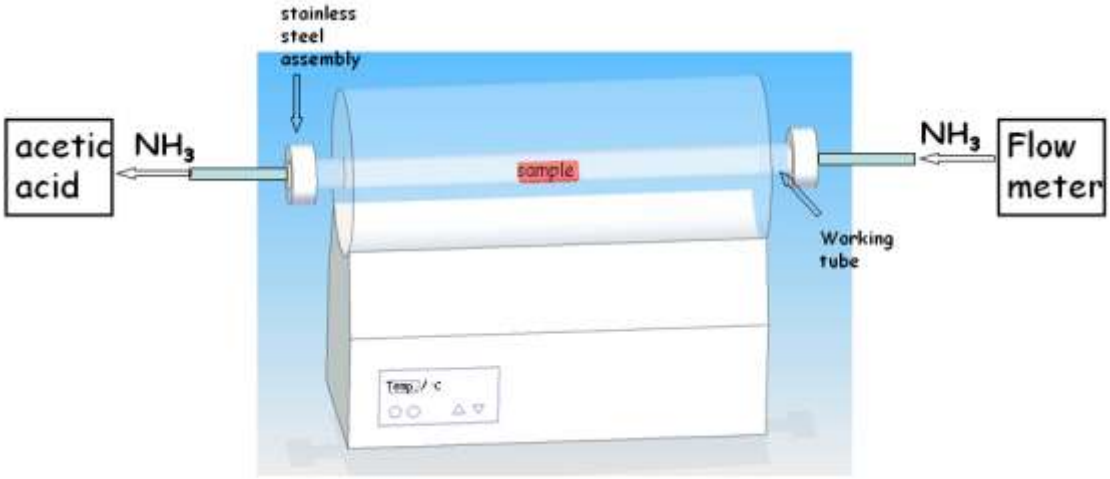

2.1.3 High pressure synthesis

High pressure high temperature (HPHT) solid state synthesis is extensively used to make materials which cannot be synthesized at ambient pressures. The preparation of superhard materials, including diamonds, is one of the important applications of HPHT synthesis. For instance, materials in the B-C-N system[1-3] and α and β-Si_3N_4[4] have been synthesized using HPHT.

Tolerance factor (t) is an important estimate of the stability of perovskites (Chapter 1.1.2.1 Perovskite). Perovskites are usually stable with $0.85 < t < 1.05$. Perovskites with lower tolerance factors can be stabilized by high pressure. Many new perovskite related materials with interesting physical properties have been synthesized using HPHT since 1970.[5] For example, the multiferroic $BiScO_3$[6, 7] and the room temperature magnetoresistance material $LnCu_3Mn_4O_{12}$ [8] have been synthesized using HPHT.

In HPHT synthesis, there are two distinct approaches used to generate high pressure, dynamic and static. Dynamic techniques can create very high pressures above 500 GPa, but only in the microsecond range, typically achieved by explosive devices.[9] Hence, it is difficult to reproduce the conditions. By contrast, static techniques can generate more controllable pressures for relatively long periods of time, by using pressure cell assemblies.

In this thesis, HPHT reactions have been achieved by using a Walker module multi-anvil press shown in Figure 2.2.[10, 11] For these experiments with a 6-8 type (anvils and cubes respectively) Walker module and graphite heating components, the press can achieve conditions up to 15 GPa, and 1500 ℃. A total mass of about 25 mg was finely ground, transferred to a boron nitride capsule, and then loaded into the press. The pressure was generated within 2 hr, and then reactants were heated to specific conditions (details in Chapters), after which the samples were quenched to room temperature, and the pressure was released over 8 hr. After decompression, the product in the octahedral assembly was carefully separated from the surrounding boron nitride.

Figure 2.2 Schematic drawing of the assemblage of the Walker-type module [10, 11]

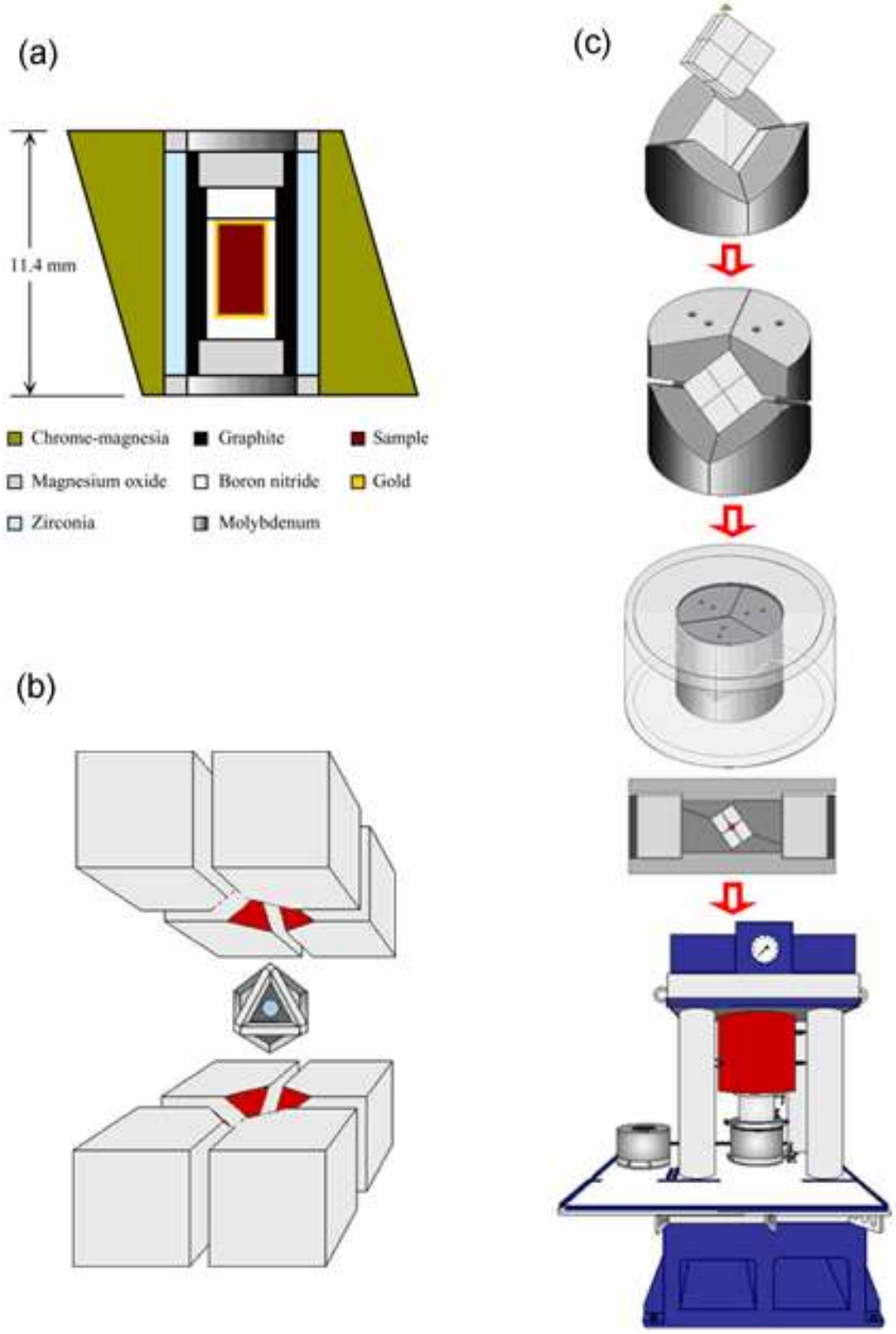

2.2 Structure characterization

2.2.1 Diffraction techniques

Crystalline materials are formed by a periodic arrangement of atoms in a three-dimensional space. Diffraction is a scattering phenomenon. For crystal structure studies, diffraction occurs when the waves have wavelengths comparable to or smaller than the size of diffracting objects at the atomic level, such as the distances between atoms. The short wavelengths of X-ray, neutrons and electrons makes them ideally suited to the characterization of crystalline materials. They cannot only be used to study the crystallographic structure, but also to obtain detailed information about the chemical composition due to each crystalline substance having its own characteristic diffraction pattern.

2.2.1.1 Bragg's Law

Bragg's Law is a simple expression of constructive diffraction that describes interference between reflected waves from different lattice planes rather than from different atoms (Figure 2.3).

$$2d_{hkl}\sin\theta = n\lambda \qquad (2.1)$$

where, n is an integer given by the order of the diffracted beam, λ is the wavelength of the beam, d is the spacing between crystal planes, and θ is the angle of the diffracted beam.

Based on Bragg's law, a crystal can be described as a series of parallel planes separated from one another by a distance d, which varies according to the nature of

the material. For a specified crystal, planes exist in every possible orientation with characteristic d-spacings. As a monochromatic beam strikes the crystal at an angle theta θ, diffraction occurs only when the difference in distance travelled equals a whole number of wavelengths nλ, also known as constructive interference. By changing θ, the Bragg's Law conditions are satisfied by different d-spacings. Plotting the angular positions and intensities of the resultant diffracted peaks of radiation produces a pattern which is characteristic of the sample. Bragg diffraction can be carried out using any beam that has a wavelength of the same order as the atomic spacing.

Figure 2.3 Bragg's Law diffraction.

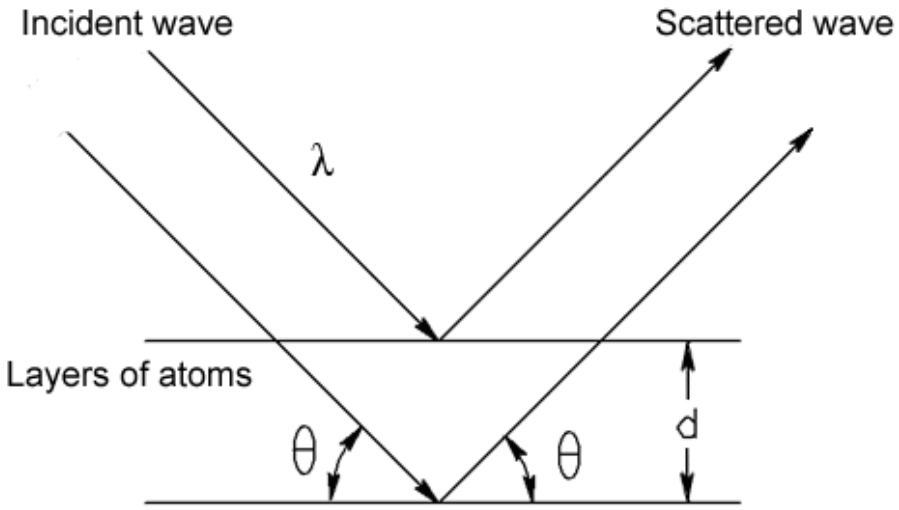

2.2.1.2 Miller indices

Diffraction peaks are dependent on the size and shape of the unit cell of a given crystalline material. All the peaks are related to sets of parallel atomic planes which can be characterized by Miller indices (hkl). h, k and l are the reciprocals of the points where the plane intersects the crystallographic axes. The d-spacing for each (hkl) plane can be calculated from the lattice parameters.

The diffracted intensities (I_{hkl}) are proportional to the square of the structure factor (F_{hkl}), where F_{hkl} is a summation over all the atoms within the unit cell, which is defined as:

$$F_{hkl} = \sum_{j=1}^{N} f_j \exp\left[2\pi i\left(hx_j + ky_j + lz_j\right)\right] \exp\left[-B_j\left(\sin^2\theta\right)/\lambda^2\right] \qquad (2.2)$$

where f_j is the scattering factor or form factor for X-rays (scattering length b_j for neutrons) of atom j, and x_j, y_j, and z_j are the fractional coordinates of atom j in the unit cell. The thermal motion of atoms is taken into account by the Debye-Waller factor where B_j is the atomic temperature factor which is related to the mean square thermal displacement factor U_j by $B = 8\pi^2 U$. Thus, an observed diffraction pattern does not only provide the information about the symmetry and lattice parameters in the crystalline material, but also about the atomic contents and atomic positions within its unit cell.

2.2.1.3 X-ray diffraction

X-ray beams can be described as electromagnetic waves (photons), which will interact with the electron cloud of an atom. Additionally, the wavelength of X-rays is of the same order as the interplanar spacings (d_{hkl}) in crystalline materials. Therefore it is ideal for diffraction studies.

As X-rays interact with the atomic electron density, the diffracted intensity increases with the atomic number. Thus it is difficult to locate light elements (such as hydrogen), particularly in the presence of heavy elements. For the same reason, it is also difficult to distinguish between elements with similar atomic electron density (such as oxygen and nitrogen) in crystalline materials. The X-rays are scattered from different electrons around the atom, thus the scattered intensity of X-rays is reduced rapidly with increasing scattering angle.

2.2.1.4 Neutron diffraction

Neutrons can also be used in diffraction for crystallographic structure studies in a similar way to X-rays. Neutron beams interact with nuclei rather than electrons in the atoms, therefore neutron diffraction provide structural information in a different way to X-ray diffraction.

According to the de Broglie equation, $\lambda = h / mv$, where h is Planck's constant, λ is the wavelength corresponding to a free particle with a mass m and a velocity v. Therefore by varying the velocity of neutrons, a neutron beam can be generated with a specific wavelength λ, which is suitable for diffraction study. As the size of atomic nuclei is much smaller than the wavelength of neutron beams, the scattered intensity of neutrons is constant at different scattering angles, unlike scattered X-rays from an

electron cloud. Additionally, there is no strong correlation between the scattering lengths and the atomic number of atoms, as shown in Figure 2.4, unlike in X-ray diffraction where the scattering factors are proportional to the atomic number. Therefore, light elements, isotopes and elements with similar electron density can be observed or distinguished by neutron diffraction.

Figure 2.4 Variation of neutron scattering length with atomic number. Full marks represent the different scattering lengths of Ni isotopes. [12]

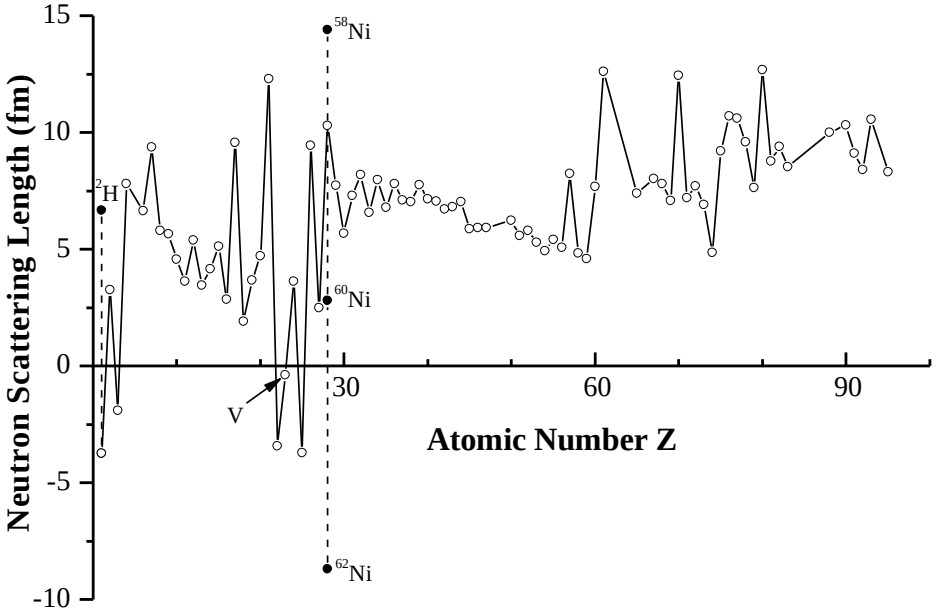

Magnetic structure determination is another important application of neutron diffraction. Neutrons, with a spin quantum number ½, show a net magnetic moment. Thus, neutrons can interact with unpaired electron spins. As this magnetic interaction is with the electron cloud, as with X-rays, the scattered intensity of neutrons is reduced rapidly with increasing scattering angle for the same reason as explained in X-ray diffraction (2.2.1.3). For paramagnetic materials, the magnetic scattering is incoherent, and therefore only shows as a contribution to the background intensity. However, for magnetically ordered materials, the magnetic scattering shows a substantial contribution. For ferromagnetic materials with magnetically ordered

states, the magnetic unit cell has the same periodicity as the nuclear unit cell, thus the two sets of reflections will be superimposed. For commensurate antiferromagnetic ordering where the periodicity of the magnetic unit cell in one or more directions is greater than for the nuclear unit cell, then extra reflections are observed. If the antiferromagnetic ordering is incommensurate, the magnetic reflections are observed as satellite peaks surrounding the nuclear reflections.

Furthermore, due to the weak interactions of a neutron beam with atomic nuclei, a wide range of experimental configurations can be used in neutron diffraction, such as cryostats, furnaces, pressure assemblies, etc. However, for the same reason, a relatively large amount of sample is required for neutron diffraction, in comparison with X-ray diffraction.

There are two types of neutron diffraction experiments, which are constant wavelength and time-of-flight. According to Bragg's law, if the wavelength of scattering beam λ is a constant, then d_{hkl} can be determined by varying the diffraction angle 2θ. On the other hand, if the diffraction angle 2θ is constant, then d_{hkl} can be determined by varying the wavelength λ of the scattering beam.

Constant wavelength neutron diffraction uses a nuclear reactor, where fast neutrons are continuously expelled by nuclear fission. In order to maintain a suitable range of wavelengths, a moderator which contains numerous low mass nuclei, is used to slow down the initial fast neutrons. Then the moderated thermal neutrons go through a monochromator to select a single wavelength for diffraction experiment.

A spallation source, also for time-of-flight (TOF), provides a neutron beam with a series of wavelengths. A high-energy proton beam is accelerated through a synchrotron ring to very high speeds (close to the speed of light), and then hits a

heavy metal target such as tantalum. This bombardment expels a number of spallation particles including neutrons with very high momentum, which can be used in diffraction experiments.

By combining Bragg's law ($2d_{hkl}\sin\theta = \lambda$) and the de Broglie equation ($\lambda = h / mv$), it gives:

$$2d_{hkl}\sin\theta = \frac{h}{mv} \quad (v=\frac{L}{t}) \tag{2.3}$$

where v is the neutron velocity. L is the length of total flight path from neutron source to sample to detector, and t is the total flight time. Therefore, v can be substituted by L and t to give:

$$\frac{2mL\sin\theta}{h} \cdot d_{hkl} = t \tag{2.4}$$

In this case, the diffraction angle 2θ is fixed. Hence d_{hkl} can be determined by t. Thus, the resolution of TOF can be improved by using a long flight path L and a high angle detector (2θ close to 180^o). However, normally for the TOF technique a few detector banks at different angles are used simultaneously to observe different t ranges.

2.2.1.5 Powder diffraction

Most solid state materials are synthesised as powders, and single crystal growth is often difficult. For many materials it is impossible to form single crystals suitable for crystallographic structure studies. Therefore, powder diffraction is the most frequently used technique to identify and characterize new materials in solid state chemistry.

In the ideal case, a polycrystalline material contains a large quantity of crystallites in all possible orientations. In this case, all hkls of the appropriate d-spacing can be observed simultaneously. These crystallites will take up every possible angular position with respect to the incident beam and therefore the diffracted beams will be emitted as cones of radiation. Thus the three-dimensional (hkl) data of single crystal diffraction is effectively reduced to one-dimensional (θ) data in powder diffraction patterns.

The interpretation of powder diffraction data is more challenging than for single crystal diffraction data. The size and symmetry of the unit cell has to be obtained directly from the peak positions of the powder patterns. Other detailed atomic information about the unit cell has to be calculated from the peak intensities. Furthermore, the overlap of peaks with similar d-spacings is usually a problem in powder diffraction patterns. Hence, structural refinement is the main crystallographic use of powder diffraction.

2.2.1.6 Transmission Electron Microscopy

For the same reason as for neutrons and X-rays, electrons can also be used for diffraction. Transmission Electron Microscopy (TEM) uses electrons generated by an electron gun for diffraction studies of materials. Based on the de Broglie equation, $\lambda = h / mv$ and the kinetic energy $E = mv^2/2$, the electron wavelength is:

$$\lambda = \frac{h}{\sqrt{2mE}} \qquad (2.5)$$

Thus, wavelength λ is related to the energy of electrons E in the unit of accelerating voltage, eV. If an electron beam has high enough energy then a diffraction pattern of

the crystal structure can be obtained. For 120 kV, the usual operation voltage for the microscopes in the thesis, λ is 0.0335 Å.

Furthermore, TEM can also be used as a microscopy that can achieve a much higher resolution than possible with a normal optical microscope due to the shorter wavelength of accelerated electrons when compared to that of visible light. Figure 2.5 shows the two different operation modes of a TEM.

Figure 2.5 Operation modes of TEM: (a) diffraction, (b) imaging. [13]

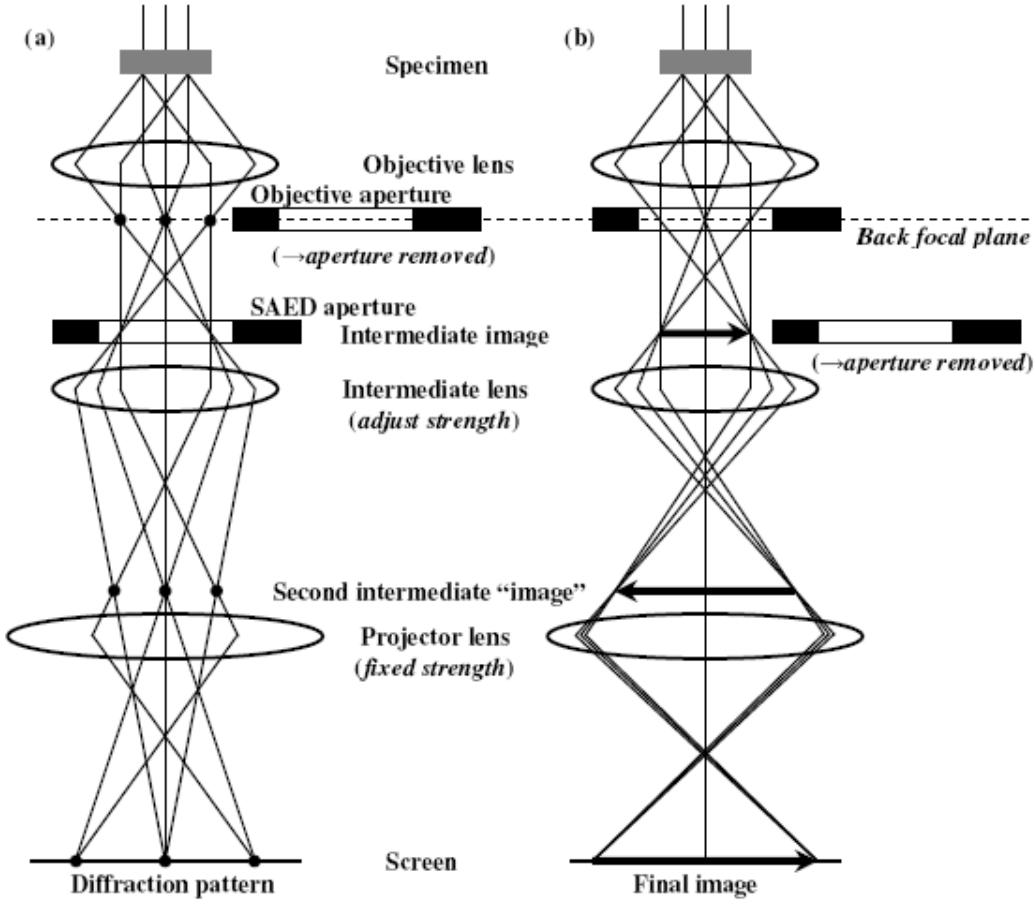

2.2.2 Experimental techniques

2.2.2.1 Laboratory Powder X-ray Diffractometer

The most commonly used source of X-rays in a laboratory diffractometer is an X-ray tube where electrons are accelerated and bombard a metal target such as copper or molybdenum to generate X-rays. The wavelength of the X-rays is characteristic to the metal target.

In this thesis, powder X-ray diffraction patterns were collected on a Bruker D8 Advance powder X-ray diffraction using a θ-2θ diffractometer with monochromatic $CuK_{\alpha 1}$ radiation (λ = 1.540562 Å) in flat plate mode. Scans were taken in the range of 2θ, 10-140^{o} at 0.007^{o} step size, and with 1-3 s count times. The initial diffraction patterns were compared with models from ICSD (Inorganic Crystal Structure Database) using Eva software before performing any structure refinement.

2.2.2.2 Time-of-Flight (TOF) Neutron Diffraction

In this thesis, the TOF neutron diffraction experiments were carried out at ISIS at Rutherford Appleton Laboratory, UK. Neutrons at the ISIS are generated by a spallation process where high speed protons hit a tantalum target. Different hydrogenous moderators, ambient temperature water (315 K), liquid methane (100 K) and liquid hydrogen (20 K) are used to slow down the initial expelled neutrons. Then, the moderated neutrons can be used for particular experiments at different experimental stations.

Figure 2.6 Layout of the synchrotron and instruments at ISIS. [14]

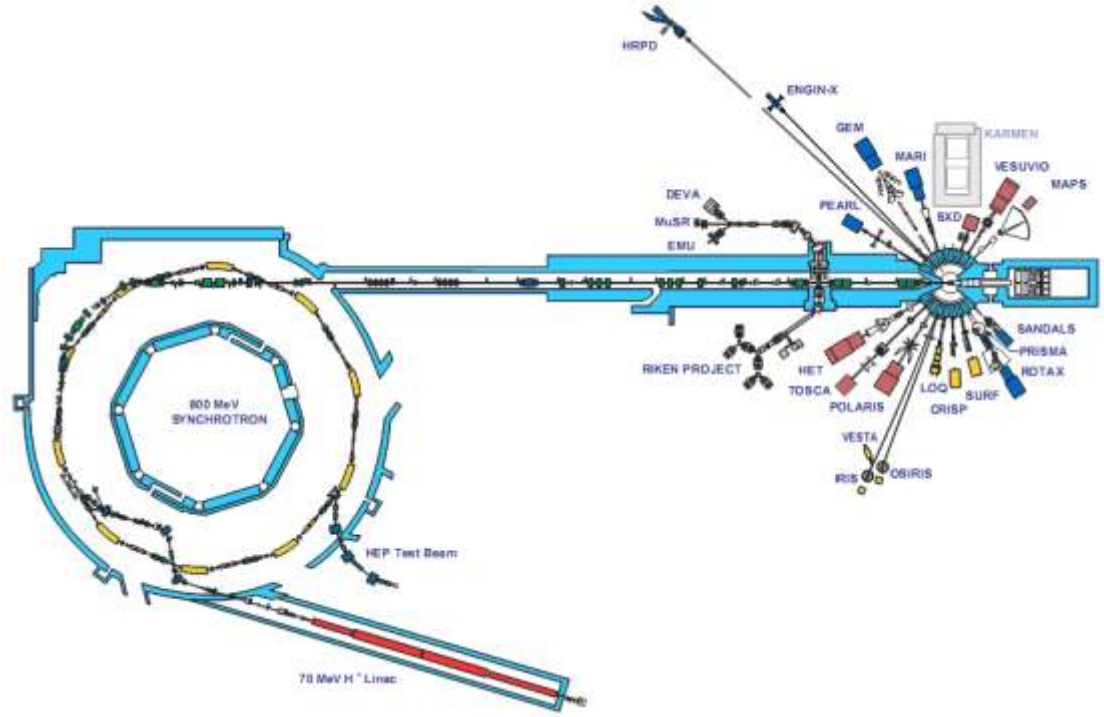

The GEneral Materials Diffractometer (GEM) at ISIS is designed for structural studies of crystalline powders. The high flux incident neutron beams pass through a liquid methane moderator, then through a flight path of 17 m to the sample. This leads to high resolution diffraction patterns. The key feature of GEM is the highly stable detector array, which has a large area of 7.27 m^2, covering a wide range of scattering angles from 1.21 to 171.41^o. The distribution of detector banks is shown in Figure 2.7. Studies at low temperatures can be achieved by using a top-loading Closed-Cycle Refrigerator (CCR).

In this thesis, TOF neutron diffraction patterns were collected from samples loaded in a vanadium can with 3 mm diameter at different temperatures using a CCR on GEM. The diffraction patterns at each temperature were collected by six detector banks for approximately 7 hr.

Figure 2.7 The distribution of detector banks at GEM. [14]

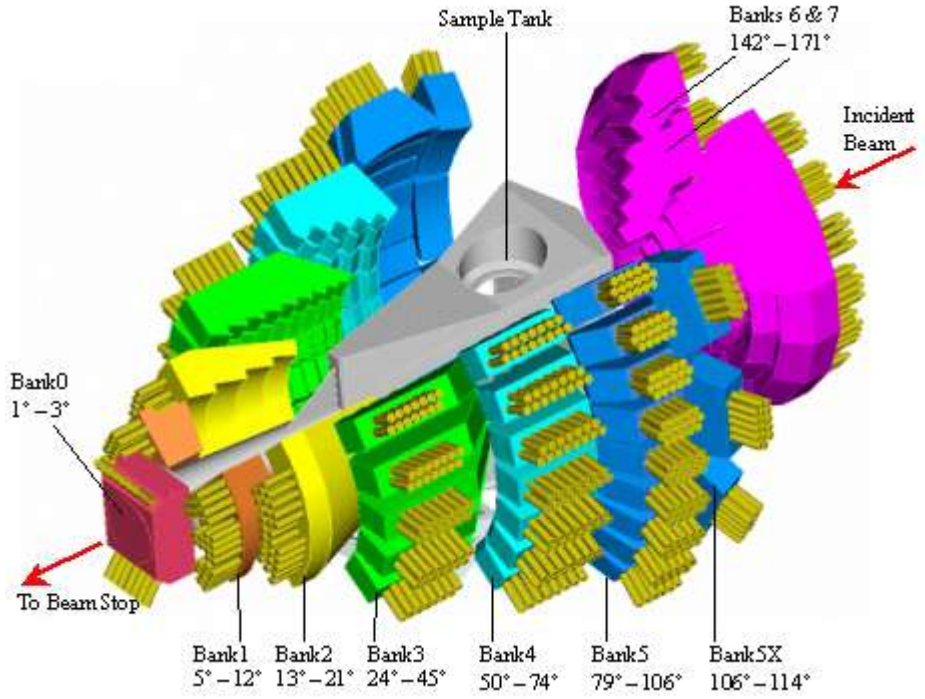

2.2.2.3 Constant Wavelength Neutron Diffraction

Constant wavelength neutron diffraction experiments were carried out at Institut Laue-Langevin (ILL) in Grenoble, France. The high flux nuclear reactor delivers a flux of 1.5×10^{15} thermal neutrons per second per cm^2 with a thermal power of 53.8 MW. A wide range of wavelengths is provided by using three moderators at different temperatures. There are a variety of stations available for different experimental purposes as shown in Figure 2.8. The instrument used in this thesis is D2B with thermal neutrons.

Figure 2.8 Experimental instruments in Institut Laue-Langevin. [15]

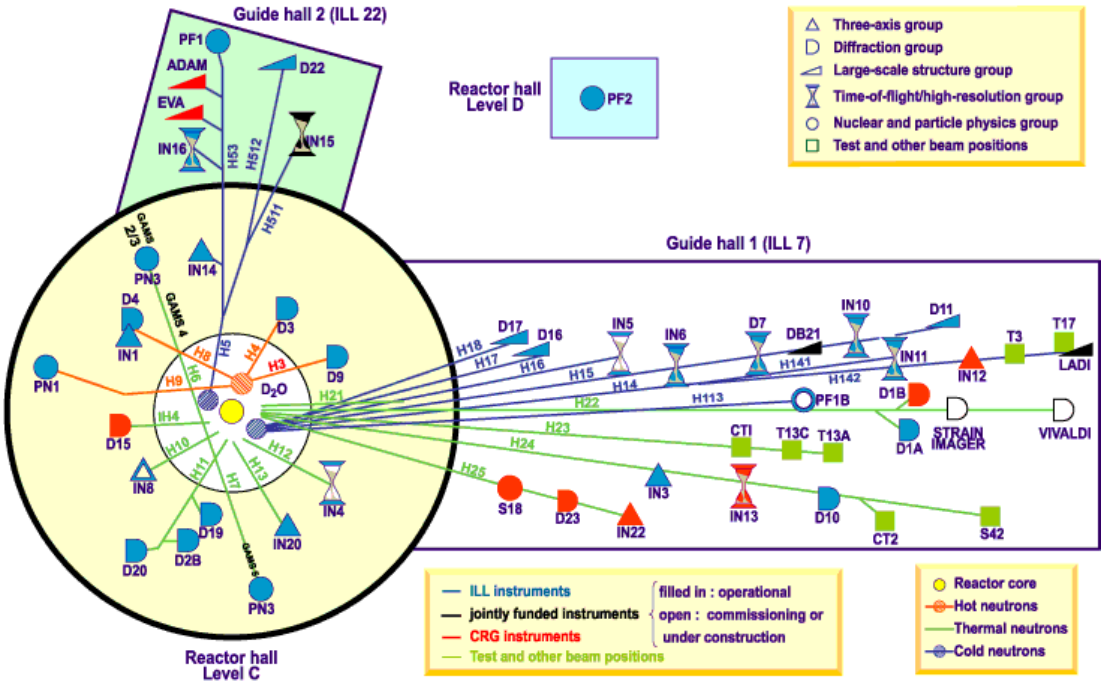

D2B is a high resolution powder diffractometer. The layout of the insturment is shown in Figure 2.9. The optimum neutron flux on the sample is enabled by both vertical and horizontal focussing of the monochromator and the high monochromator take-off angle (135^{o}). A range of neutron wavelengths from 1.051 to 3.152 Å can be achieved by altering the hkl of a Ge crystal monochromator. The optimum flux is achieved with a neutron wavelength of 1.594 Å. There are 128 detectors, 300 mm in height, fixed regularly at 1.25^{o} intervals. Thus a complete pattern with the 2θ range of 5^{o} to 165^{o} can be obtained with 25 steps of 0.05^{o}. In order to improve the statistics, scans are normally repeated several times. A wide temperature range between 1.5 to 1000 K can be controlled in situ with a cryostat or furnace.

The neutron powder diffraction data from D2B in this thesis were collected with 8 mm diameter vanadium can at temperatures between 25 and 750 ℃. Data were collected in the 2θ range of 5 °to 155 °for approximately 3 hr per scan with a neutron

wavelength of 1.5943 Å.

Figure 2.9 The layout of D2B. [15]

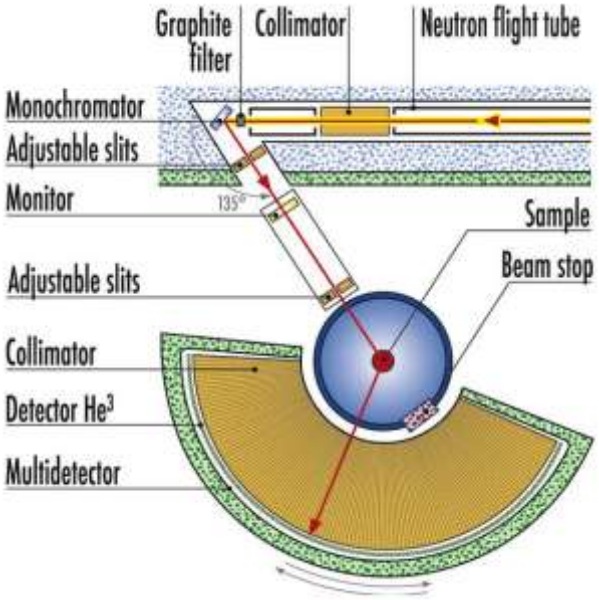

2.2.2.4 TEM

The TEM data collection in this thesis was performed by Dr. Judith Oró-Solé and Prof. Amparo Fuertes at Institut de Ciència de Materials de Barcelona (C.S.I.C.), Campus U.A.B., 08193 Bellaterra, Spain. A copper grid with a holey carbon film was used to mount a small amount of the sample powder. Electron diffraction micrographs were obtained by using a JEOL 1210 transmission electron microscope operating at 120 kV, equipped with a side-entry 60/30 ° double tilt GATHAN 646 specimen holder.

2.2.3 Rietveld analysis

For structure characterization in powder diffraction, refinement is essential due to the problem of reflection overlapping, as discussed in 2.2.1.4 Powder diffraction. A least squares approach is used in the Rietveld method, [16, 17] to get the best fit between a theoretical profile and an observed profile from diffraction. The Rietveld method is a full pattern analysis technique. It does not consider the reflections or overlapping peaks individually, but performs a curve fitting by calculating all the observed intensity in equal step sizes over the whole diffraction range, which can be described as:

$$y_{i(obs)} = y_{i(back)} + \sum_i y_{i(Bragg)}^{(i)} \qquad (2.6)$$

where $y_{i(obs)}$ is the observed intensity, $y_{i(back)}$ is the background intensity and $\sum_i y_{i(Bragg)}^{(i)}$ is the sum of the contributions of reflections close to the powder pattern step i, which contains information about the crystal structure.

The refinement by the Rietveld method is achieved by minimising the residual S_y between the observed intensity $y_{i(obs)}$ and the calculated intensity $y_{i(calc)}$ by the best least-square fits to all the steps:

$$S_y = \sum_i w_i (y_{i(obs)} - y_{i(calc)})^2 \qquad (2.7)$$

where w_i is statistical weight, usually equal to $1/y_{i(obs)}$, and $y_{i(calc)}$ is the calculated intensity of each step. $y_{i(calc)}$ is a sum of the contribution of all nearby reflections, k, which can be described as:

$$y_{i(calc)} = s\sum_{k} L\,|F_k|^2\,\phi_k(2\theta_i - 2\theta_k)\,P_k\,A + y_{i(back)} \qquad (2.8)$$

where s is the scale factor, L contains the Lorentz, polarisation and multiplicity factors, F_k is the structure factor, $\phi(2\theta_i - 2\theta_k)$ is the peak shape function, P_k is the preferred orientation function, A is the absorption factor and $y_{i(back)}$ is the background intensity at the step i of the diffraction pattern. All the terms in Equation 2.8, may be adjusted to minimise the residual S_y in the refinement process.

The peak shape function, $\phi(2\theta_i - 2\theta_k)$, contains the contribution of the instrument and the sample on the reflection profile. For constant wavelength data, including X-rays and low resolution neutrons, the instrumental and partical size broadening are almost entirely Gaussian and the angular dependence of the Full Width at Half Maximum (FWHM) is empirically modelled by: [18]

$$FWHM^2 = U\tan^2\theta + V\tan\theta + W \qquad (2.9)$$

where U, V and W are the refinable parameters. For high resolution data, the peak is sharp, thus particle size or strain broadening may affect the refinement, and are modelled by a Lorentzian function with: [19]

$$FWHM = X\tan\theta + \frac{Y}{\cos\theta} \qquad (2.10)$$

where X and Y are refinable parameters.

The quality of refinement can be estimated by the following residual values,

$$R_p = \frac{\sum \left| (y_{i(obs)}) - (y_{i(calc)}) \right|}{\sum (y_{i(obs)})} \qquad (2.11)$$

$$R_{wp} = \left[\frac{\sum w_i (y_{i(obs)} - y_{i(calc)})^2}{\sum w_i (y_{i(obs)})^2} \right]^{1/2} \qquad (2.12)$$

$$\chi^2 = \sum \frac{w_i (y_{i(obs)} - y_{i(calc)})^2}{n - p + c} \qquad (2.13)$$

where $y_{i(obs)}$, $y_{i(calc)}$ and w_i are the observed intensity, calculated intensity and statistical weight at the i^{th} step, respectively. n is the number of observations, p is the number of parameters and c is the number of constraints. A lower residual value represents better fitting. χ^2 is also known as goodness of fit, as it is proportional to S_y. The R_{wp} is another commonly considered value as it contains S_y. However, none of these values can be counted as an absolute criteria of refinement, because these values may be affected by high background intensities and long counting times. Hence, it is important to examine the quality of refinements by multiple factors, as well as the chemical and physical sense of the results.

A number of programs can be used for structure determination such as GSAS, TOPAS, Fox, EXPO2004, and others. All refinements in this thesis were carried out with the Rietveld method using the General Structure Analysis System (GSAS) developed by A. C. Larson and R. B. von Dreele. [20]

2.3 Bond valence theory

The bond lengths and bond angles of a crystal structure are some of the most important output data from a structural refinement. The bond valence can be calculated from bond lengths by using the Bond Valence Sum (BVS). [21, 22] Furthermost, the valence of cations in the materials can be calculated from the bond valences. In Bond Valence theory, the bond valence is given as:

$$s_{ij} = \exp(\frac{r_0 - r_i}{B}) \qquad (2.14)$$

where s_{ij} is the bond valence between cation i and anion j, r_i is observed bond length from structure refinement, r_0 is an empirically determined value from reference structures, and B is a constant value of 0.37 Å. The valence of cation, V_i can be calculated according to:

$$V_i = \sum s_{ij} \qquad (2.15)$$

2.4 Physical property measurements

2.4.1 Magnetisation measurements

In this thesis, magnetisations of the samples at different temperatures and fields were studied by using a Quantum Design Magnetic Property Measurement System (MPMS). The MPMS contains a Superconducting Quantum Interference Device (SQUID) which is a sensitive device for measuring magnetic fields. Superconductors play two important roles in this device. They generate a large uniform magnetic field and they detect any tiny changes in the magnetic field from the samples during the

measurement. The configuration of the MPMS is shown in Figure 2.10. The sensitivity of this SQUID is 10^{-7} emu.

Figure 2.10 Configuration of the MPMS. [23]

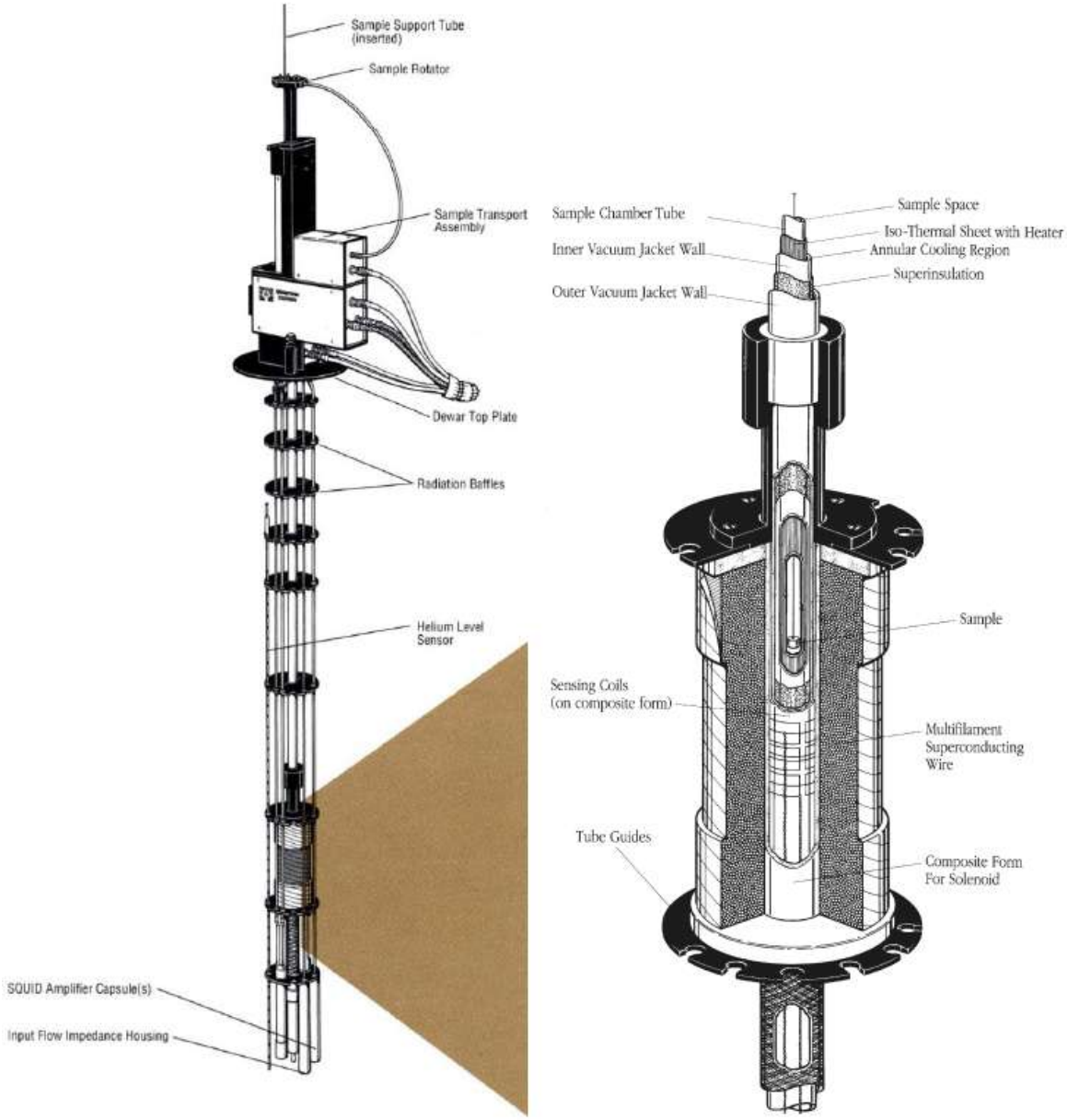

Approximately 30 mg of pelleted sample were placed in a gelatine capsule with an inverse capsule configuration to avoid any movement during the measurement. The temperature and magnetic field ranges were 2 – 300 K and 0 – 7 Tesla, respectively.

2.4.2 Conductivity measurements

In this thesis, the electrical resistivity of the samples were studied using a Quantum Design Physical Properties Measurement System (PPMS). The sensitivity of the PPMS is 10^{-3} ohms. A typical four probe configuration, which contains four electrical contacts to the rectangular sample bar, was used for these resistivity measurements, as shown in Figure 2.11. The measurements in each case were performed by introducing an electrical current I, along the sample with a cross sectional area A, whilst the voltage was measured across the contacts with a length L between V^+ and V^-. The resistivity ρ can be calculated from the measured resistance R according to the formula below:

$$\rho = \frac{R \cdot A}{L} \qquad (2.16)$$

Figure 2.11 Four probe configuration of the resistivity measurement

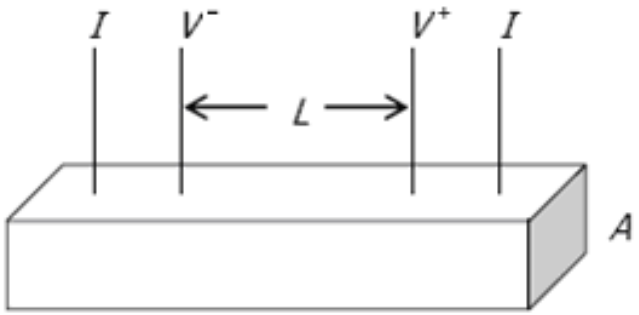

Copper wires were attached with silver epoxy resin to reduce contact resistance. The measurements were carried out on three samples simultaneously. The electronic resistivity measurements were taken at a temperature range of 2-300 K under 0 and 7 Tesla, respectively. The magnetoresistivity measurements were made at 2, 8, 15, 30 and 50 K by varying the magnetic field between -7 and +7 T.

2.5 References

1. V. L. Solozhenko, D. Andrault, G. Fiquet, M. Mezouar and D. C. Rubie, *Appl. Phys. Lett.* 2001, 78, 1385.
2. Y. Zhao, D. W. He, L. L. Daemen, T. D. Shen, R. B. Schwarz, Y. Zhu, D. L. Bish, J. Huang, J. Zhang, G. Shen, J. Qian, T. W. Zerda, *J. Mater. Res.* 2002, 17, 3139.
3. V. L. Solozhenko, S. N. Dub and N. V. Novikov, *Diam. Relat. Mater.* 2001, 10, 2228.
4. T. Sekine, *J. Am. Ceram. So.* 2002, 85, 113.
5. J. A. Rodgers, A. J. Williams, and J. P. Attfield, *Z. Naturforsch.* 2006, 61b, 1515.
6. A. A. Belik, S. Iikubo, K. Kodama, N. Igawa, S. Shamoto, M. Maie, T. Nagai, Y. Matsui, S.Y. Stefanovich, B. I. Lazoryak, E. Takayama-Muromachi, *J. Am. Chem. Soc.* 2006, 128, 706.
7. Y. Inaguma, A. Miyaguchi, M. Yoshida, T. Katsumata, Y. Shimojo, R. P. Wang, T. Sekiya, *J. Appl. Phys*. 2004, 95, 231.
8. B. Bochu, J. C. Joubert, A. Collomb, B. Ferrand and. D. Samaras, *Journal of Magnetism and Magnetic Materials* 1980, 15, 1319.
9. H. Huppertz, *Z. Kristallogr.* 2004, 219, 330.
10. D. Walker, M. A. Carpenter and C. M. Hitch, *Am. Mineral.* 1990, 75, 1020.
11. D. Walker, *Am. Mineral.* 1991, 76, 1092.
12. NIST Center for Neutron Research, http://www.ncnr.nist.gov/
13. D. B. Williams and C. B. Cater, *"Transmission Electron Microscopy I: Basics"*, Plenum Publishing Corporation, 1996.
14. ISIS at Rutherford Appleton Laboratory, http://www.isis.rl.ac.uk/
15. The Institut Laue-Langevin, http://www.ill.eu/
16. H. M. Rietveld, *J. Appl. Cryst.* 1969, 2, 65.
17. R. A. Young, *The Rietveld Method*, Oxford University Press, 1993.
18. G. Caglioti, A. Paoletti, F. P. Ricci, Nuclear Instruments & Methods 1958, 3, 223.
19. P. Thompson, D. E. Cox, J. B. Hastings, *J. Appl. Cryst.* 1987, 20, 79.

20. A. C. Larson and R. B. von Dreele, "General Structure Analysis System (GSAS)", Los Alamos National Laboratory Report LAUR 86-748 (1994)

21. I. D. Brown, *J. Appl. Crystallogr.* 1996, 29, 479.

22. J. P. Attfield, *Solid State Sci.* 2006, 8, 861.

23. Quantum Design, http://www.qdusa.com/

Chapter 3. Synthesis, structure and physical properties study of $EuWO_{1+x}N_{2-x}$

3.1 Introduction

Transition metal oxynitrides are an important class of emerging materials that in optimal cases may combine the advantages of transition metal oxides and nitrides. They generally have greater air and moisture stability than pure nitrides, but with smaller bandgaps than comparable oxides leading to useful electronic or optical properties, [1-6] see detailed discussion and examples in Chapter 1.

The discovery of CMR in $EuNbO_2N$ resulted from a slight nitrogen-deficiency leading to electron doping of the Nb d-band (reduction of Nb^{5+} to Nb^{4+}), as the coupling of the carrier spins to those of the localized, ferromagnetically ordered Eu^{2+} S = 7/2 states gives rise to colossal magnetoresistances at low temperatures (>99% reduction of resistance at 2 K).[3] Materials showing CMR are of interest for memory and sensor applications, and large magnetoresistances had not previously been reported in oxynitrides. Thus, further europium-based analogues have been investigated. W is a transition metal with W^{5+}/W^{6+} oxidation state flexibility. One impure composition of Eu-W-O-N with the perovskite structure has been reported but without any conductivity study. [7]

In this work, $EuWO_{1+x}N_{2-x}$ with a wide range of nitrogen contents has been synthesized using thermal ammonolysis at various conditions. Detailed magnetic and conducting properties of these samples have been studied and are discussed.

3.2 Experimental

3.2.1 Synthesis

An $Eu_2W_2O_9$ precursor was prepared by a solid state reaction between Eu_2O_3 (99.99%, Aldrich) and WO_3 (99.99%, Aldrich) which were heated for three 24 hr periods at temperatures of 950 to 1150 °C with intermediate regrindings. 0.2 – 0.3 g samples of $Eu_2W_2O_9$ were placed in an alumina boat in a tube furnace for ammonolysis. Nitrogen gas (Oxygen-free, BOC) was passed over the sample for 15 min to expel air before the flow of ammonia gas (99.999%, BOC) was started. The sample was heated to the reaction temperature at 150 °C/hr and furnace cooled after treatment. Sintered pellets were prepared for resistivity measurements by heating compressed $EuWO_{1+x}N_{2-x}$ powders at 550 °C for 3 hr under ammonia gas flowing at 250 cm^3/min.

3.2.2 Sample analysis

The nitrogen contents of the products were determined as N_2 by a combustion method using a Carlo Erba CHNS analyzer. Approximately 3 mg of finely ground powder was used for each analysis and results of three analyses were averaged for each sample. Finely ground powders were examined with a powder X-ray diffractometer using monochromatic $CuK_{\alpha 1}$ radiation (λ = 1.540562 Å). Scans were taken in the 2θ range 10-120° with a 0.007° step size and a 3 s count time. Crystal structures were fitted to the X-ray diffraction profiles using the GSAS package.[8] The TOF neutron powder diffraction patterns were collected using a 3 mm diameter vanadium can at 2, 6, 10, 14 and 18 K at GEM in ISIS. The diffraction patterns at each temperature were collected from 1 – 6 detector banks for ~7 hr. Multi-histogram structure refinements from banks 2 – 4 were performed using GSAS. Electron

diffraction micrographs were obtained in a JEOL 1210 transmission electron microscope operating at 120 kV, equipped with a side-entry 60/30° double tilt GATHAN 646 specimen holder. The samples were prepared by dispersing the powders in ethanol and depositing of a droplet of this suspension on a carbon coated holey film supported on a copper grid.

3.2.3 Physical properties study

Electrical resistivities were measured from 2 to 300 K in zero and 7 T magnetic fields using a four-probe method with a Quantum Design Physical Properties Measurement System (PPMS). Resistivity-field measurements were made at 2, 8, 15, 30 and 50 K by varying the magnetic field between -7 and +7 T. Magnetic susceptibilities were recorded using a Quantum Design Magnetic Properties Measurement System (MPMS) SQUID magnetometer under an external field of 100 Gauss from 2 to 300 K after cooling the sample in the field (FC) or in zero field (ZFC). Magnetization-field loops were measured between -7 and +7 T at 2, 8, 15, 30 and 50 K.

3.3 Results and discussion

3.3.1 Synthesis of precursor

$Eu_2W_2O_9$ is a convenient precursor for the ammonolytic synthesis of $EuWO_{1+x}N_{2-x}$ as it provides a 1:1 atomic scale mixture of Eu and W. Impure samples of this precursor were found to give impure perovskite products. Thus in this work, the X-ray diffraction profile was fitted carefully to check for the presence of secondary phases. $Eu_2W_2O_9$ was white in colour and crystallized in the $P2_1/c$ with cell parameters a = 7.5535(1), b = 9.6769(2), c = 9.1226(2) Å, β = 107.76(2)°, in agreement with

published data.[9]

3.3.2 Ammonolysis of $Eu_2W_2O_9$

Ammonolysis reactions of $Eu_2W_2O_9$ were carried out for a range of temperatures (450 – 850 °C), ammonia flow rates (22 to 250 cm^3/min) and times (10 min to 12 hr) to explore the reaction pathway and compositional variations in the products. The reaction was found to proceed via a crystalline, scheelite ($CaWO_4$) type intermediate phase, of ideal composition $EuWO_4$, as shown by the representative powder X-ray diffraction patterns in Figure 3.1. Ammonia can act as a simultaneous reducing and nitriding agent, or can bring about just one of these changes. In this case, the reaction proceeds through two distinct steps, which in the simplest description are a reduction and a nitride substitution according to the ideal formulae:

$$Eu_2^{3+}W_2^{6+}O_9 \rightarrow Eu^{2+}W^{6+}O_4 \rightarrow Eu^{2+}W^{6+}ON_2 \qquad (3.1)$$

However, a range of Eu and W redox states are found in the final perovskite product, as discussed later. No additional amorphous X-ray scattering is observed during the conversions of $Eu_2W_2O_9$ to $EuWO_4$ and of $EuWO_4$ to the perovskite phase (see the two two-phase patterns in Figure 3.1). This demonstrates that the reduction of $Eu_2W_2O_9$ and nitridation of $EuWO_4$ reactions are each followed by rapid recrystallization, as there are no simple topotactic relations between the $Eu_2W_2O_9$, $EuWO_4$ and perovskite structures.

Figure 3.1 Powder X-ray diffraction patterns illustrating the conversion of $Eu_2W_2O_9$ to the perovskite $EuWO_{1+x}N_{2-x}$ via an intermediate scheelite phase $EuWO_{4-y}N_y$, with the crystal structures also shown. The ammonolysis was performed at 600 °C with a flow rate of 250 cm^3/min.

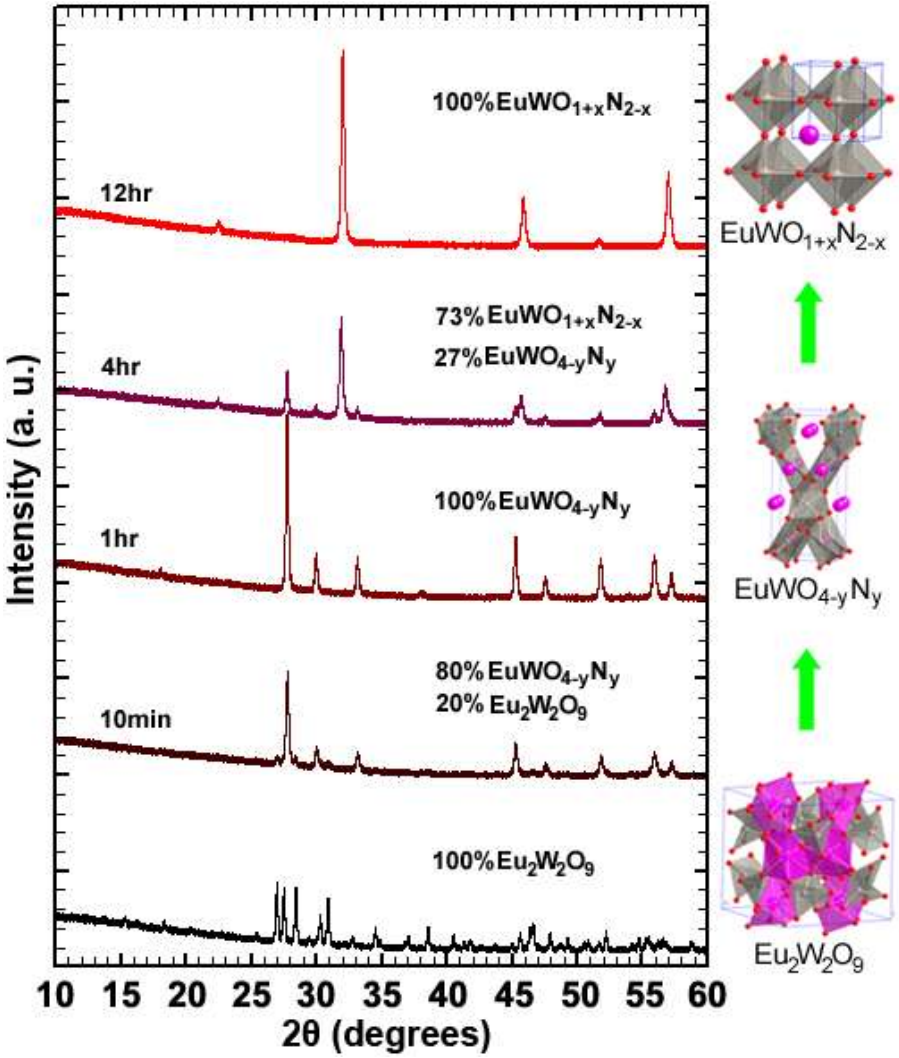

3.3.2.1 Synthesis of $EuWO_{4-y}N_y$ scheelites

Ammonolyses at temperatures between 450 and 550 °C produced single phase samples of the tetragonal scheelite intermediate with ideal composition $EuWO_4$. This structure contains 8-coordinate Eu^{2+} and isolated tetrahedral tungstate groups. Reaction conditions and lattice parameters for the resulting samples and those

reported for $EuWO_4$ [9] are shown in Table 3.1, and a profile fit is displayed in Figure 3.2 with structural results in Table 3.2. Small variations in the unit cell parameters between samples indicate that these scheelites are slightly non-stoichiometric.

Table 3.1 Reaction conditions (ammonia flow rate = 250 cm^3/min) and lattice parameters for the scheelite phases $EuWO_{4-y}N_y$ formed by the ammonolysis of $Eu_2W_2O_9$, with the reported lattice parameters [9] for $EuWO_4$ shown for comparison in the final row.

Temperature / °C	Time / hr	a / Å	c / Å	V / $Å^3$
*600	4	5.4140(1)	11.9547(6)	350.42(2)
550	12	5.4143(1)	11.9564(2)	350.50(1)
500	12	5.4130(1)	11.9503(3)	350.15(2)
450	12	5.4078(1)	11.9362(2)	349.07(1)
-	-	5.411(1)	11.936(1)	349.4(1)

* sample contains both scheelite and perovskite phases, as shown on Figure 3.1

Figure 3.2 Fit of the scheelite type $EuWO_{4-y}N_y$ structural model in Table 3.1 to powder X-ray diffraction data, showing the difference between the experimental and calculated points and the Bragg reflection markers.

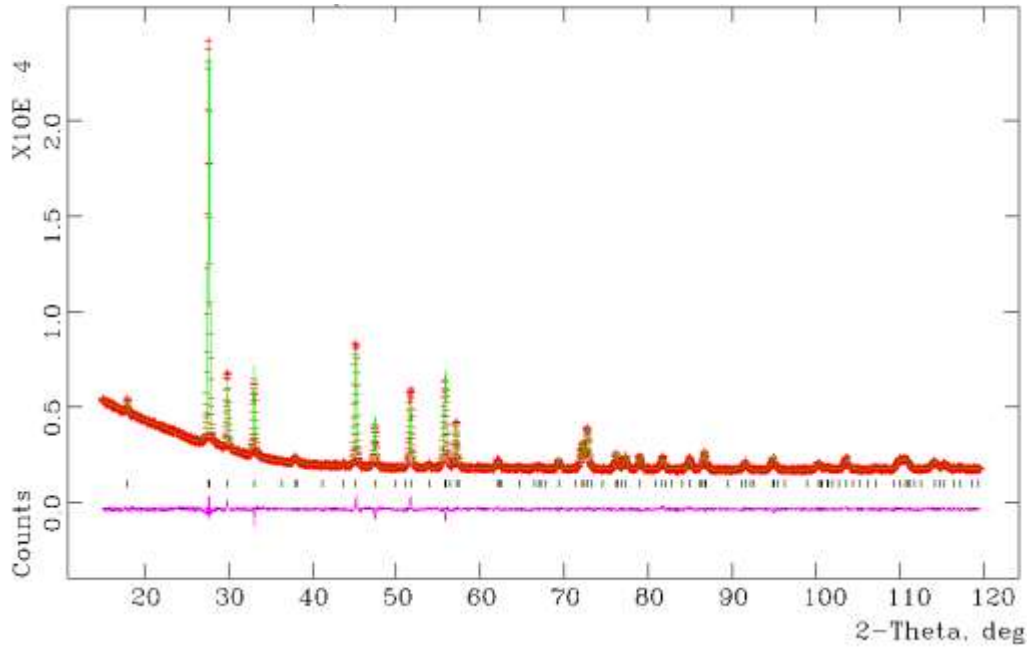

Table 3.2 Atomic coordinates and bond distances in Å for $EuWO_{3.96}N_{0.04}$ synthesized at 550 °C, in space group $I4_1/a$, from refinement against powder X-ray diffraction data. Cell parameters; a = 5.4144(1), c = 11.9511(1) Å, V = 350.36(1) $Å^3$; residuals R_{wp} = 2.88, R_p = 2.14%, χ^2 = 1.949; overall isotropic temperature factor = 0.0111(5) $Å^2$.

Atom	x	y	z
Eu	0	0.25	0.625
W	0	0.25	0.125
O/N	0.2264(14)	0.0912(10)	0.0504(3)

Eu-O/N (x 4)	2.530(5)	<Eu-O/N>	2.619(6)
Eu-O/N (x 4)	2.708(7)	W-O/N (x 4)	1.742(6)

In this work, the scheelite samples obtained from ammonolyses at 500-600 °C show expansion of the unit cell relative to that of $EuWO_4$, indicating the oxidation of Eu^{2+} is compensated by nitride substitution, i.e. $Eu^{2+}_{1-y}Eu^{3+}_{y}WO_{4-y}N_{y}$, and chemical analysis of the 550 °C sample in Table 3.1 showed that 0.13(1)wt% N is present corresponding to a value of y = 0.04. This small N-content is consistent with the average Eu-O(/N) bond distance of 2.62 Å (Table 2) which is in good agreement with the ideal Eu^{2+}-O distance of 2.61 Å predicted from ionic radii. The samples show a range of colours from yellow to orange at various temperatures, hence further proving the presence of mixed valence Eu^{3+}/ Eu^{2+}.

Stoichiometric, scheelite-type oxynitrides $LnWO_3N$ have previously been obtained by ammonolysis of $Ln_2W_2O_9$ for the trivalent lanthanides Ln = La, Sm, Nd, Dy,[10] but the Eu analogue, corresponding to the y = 1 limit of $Eu^{2+}_{1-y}Eu^{3+}_{y}WO_{4-y}N_{y}$, was not obtained. $EuWO_3N$ would be a plausible intermediate if a nitridation reaction occurred before reduction, i.e.

$$Eu_2^{3+}W_2^{6+}O_9 \rightarrow Eu^{3+}W^{6+}O_3N \quad Eu^{2+}W^{6+}O_3N \qquad (3.2)$$

but these results show that almost complete reduction of Eu^{3+} to Eu^{2+} occurs before nitridation. Hence, the $Eu^{2+}_{1-y}Eu^{3+}_{y}WO_{4-y}N_{y}$ phase is only formed with small values of y $\approx$ 0.04.

3.3.2.2 Synthesis of $EuWO_{1+x}N_{2-x}$ perovskites

The ammonolysis of $Eu_2W_2O_9$ at temperatures between 600 and 850 °C at various flow rates and reaction times (Table 3.3) produced pure phases of the perovskite $EuWO_{1+x}N_{2-x}$. Systematic investigations of the effects of temperature or ammonia

flow rate on the nitrogen content are shown in Figure 3.3. These demonstrate that either variable can be used to access a wide range of compositions ($\Delta x \sim 0.3$-0.4) within the domain of conditions used here. High temperatures and flow rates and long reaction times increase the nitrogen content.

Table 3.3 Ammonolysis conditions for the formation of $EuWO_{1+x}N_{2-x}$ perovskites with cubic lattice parameters and analyzed compositions x shown.

T / °C	Flow rate / $cm^3 \cdot min^{-1}$	Duration / hour	Lattice a / Å	x
850	250	12	3.9472(2)	-0.16
850	120	10	3.9536(1)	-0.12
800	250	10	3.9556(2)	-0.04
800	120	10	3.9591(1)	0.09
800	250	8	3.9621(1)	0.17
750	250	8	3.9674(1)	0.25
600	120	8	3.9756(2)	0.41
600	120	6	3.9779(3)	0.46

Figure 3.3 Plots of the compositional variable x and the N content for $EuWO_{1+x}N_{2-x}$ perovskites (a) heated under ammonia at a flow rate of 250 cm^3/min^{-1} for 12 hr at various temperatures, and (b) heated at 600 °C for 12 hr at variable flow rates.

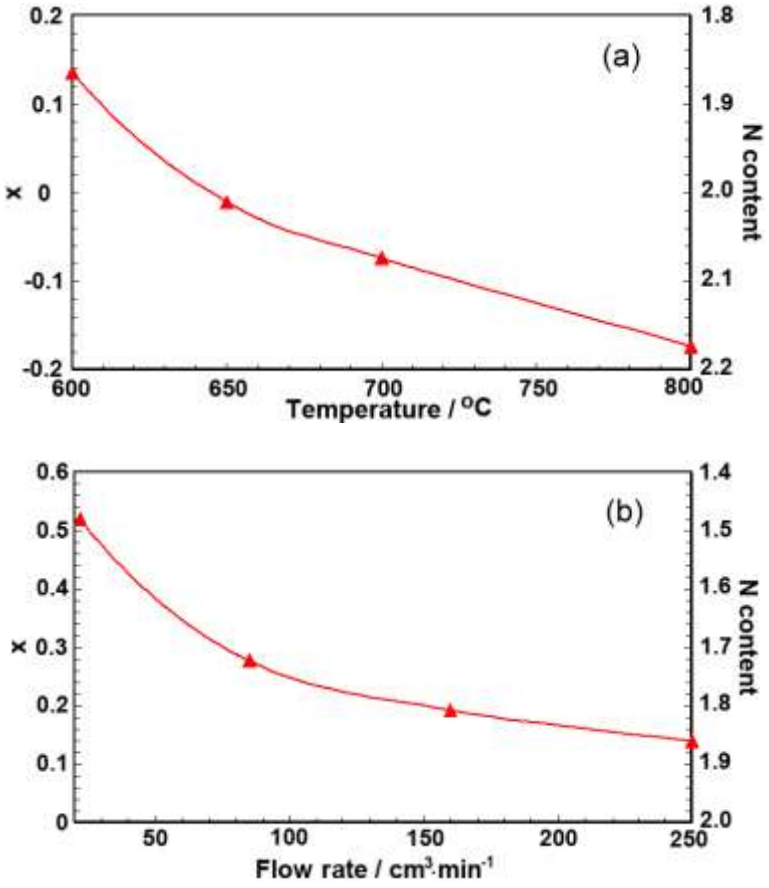

Chemical analyses showed that a wide range of nitrogen contents ($-0.16 \leq x \leq 0.46$) were obtained. A notable discovery is that ammonolysis at relatively high temperatures of 800-850 °C gave nitrogen-rich materials with negative values of x in the $EuWO_{1+x}N_{2-x}$ formulation. Previous studies[7] reported only nitrogen-deficient materials with positive x values, corresponding to chemical reduction of W (electron-doping of the W:5d (t_{2g}) band), formally $Eu^{2+}W^{6+}_{1-x}W^{5+}_{x}O_{1+x}N_{2-x}$. These demonstrates that materials in which Eu is oxidized (hole-doping of the Eu:4f band) can also be accessed with formal compositions $Eu^{2+}_{1+x}Eu^{3+}_{-x}W^{6+}O_{1+x}N_{2-x}$ for negative x values up to x = -0.16. Hence, both the W and Eu oxidation states can be tuned in the

$EuWO_{1+x}N_{2-x}$ system by varying the O/N ratio. The ideal x = 0 stoichiometry $EuWON_2$ does not appear to have any special chemical stability, an attempt to prepare this composition resulted in a slightly N-rich (x = -0.04) sample.

All of the $EuWO_{1+x}N_{2-x}$ samples appear cubic by powder X-ray diffraction and the patterns are fitted well by the simple cubic $Pm\bar{3}m$ perovskite structure model (Figure 3.4) with no superstructure peaks evident. The cubic lattice parameters (Table 3.3) show a linear variation with the analysed nitrogen content for all samples (Figure 3.5) and no change in slope is evident at the x = 0 crossover between electron and hole doped regimes. The decrease in lattice parameter with increasing N content shows that the lattice contraction from the oxidations of the cations outweighs the expanding effect of replacing oxide by the larger nitride anion.[11]

Figure 3.4 Fit of the cubic perovskite model for $EuWO_{1+x}N_{2-x}$ (x = -0.04) to powder X-ray diffraction data.

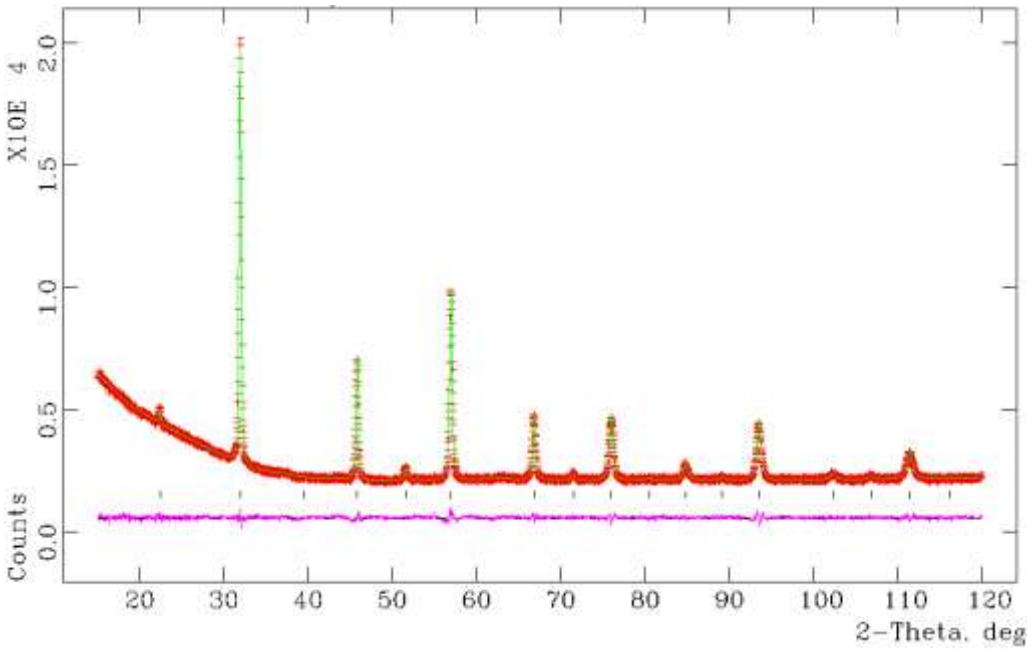

Figure 3.5 Plot of the cubic lattice parameter a against the analysed N content and the equivalent variable x for $EuWO_{1+x}N_{2-x}$ samples.

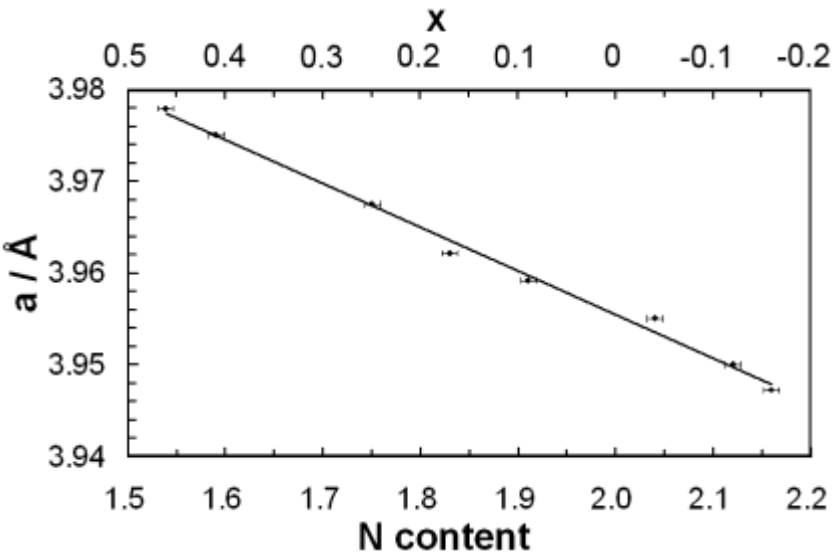

3.3.3 Magnetic properties

The magnetic, conductivity and magnetoresistance properties of three $EuWO_{1+x}N_{2-x}$ samples with x = 0.41, -0.04 and -0.12 were measured, which covers nitrogen deficient, nitrogen-rich, and the close-to-stoichiometry samples.

The magnetic susceptibilities of the samples have very similar temperature variations. All show a ferromagnetic transition at a Curie temperature of $T_C = 12 \pm 1$ K, below which field and zero-field cooled susceptibilities diverge (Figure 3.6). The high temperature susceptibilities follow a Curie-Weiss variation and the derived Curie constants, paramagnetic moments and Weiss temperatures are shown in Table 3.4. The positive Weiss temperatures confirm the dominant ferromagnetic exchange interactions and the maximum value is obtained for the x = -0.04 sample which may signify higher structural order or loss of competing antiferromagnetic interactions at x = 0. Magnetization-field loops show typical behaviour for soft ferromagnets at low temperatures (Figure 3.7) and the saturated magnetizations (taken from the 2 K data)

are also shown in Table 3.4.

Figure 3.6 Zero field cooled (ZFC) and field cooled (FC) ac magnetic susceptibilities of $EuWO_{0.96}N_{2.04}$ at low temperatures and the inverse FC susceptibility (inset), using a 0.01 T magnetic field.

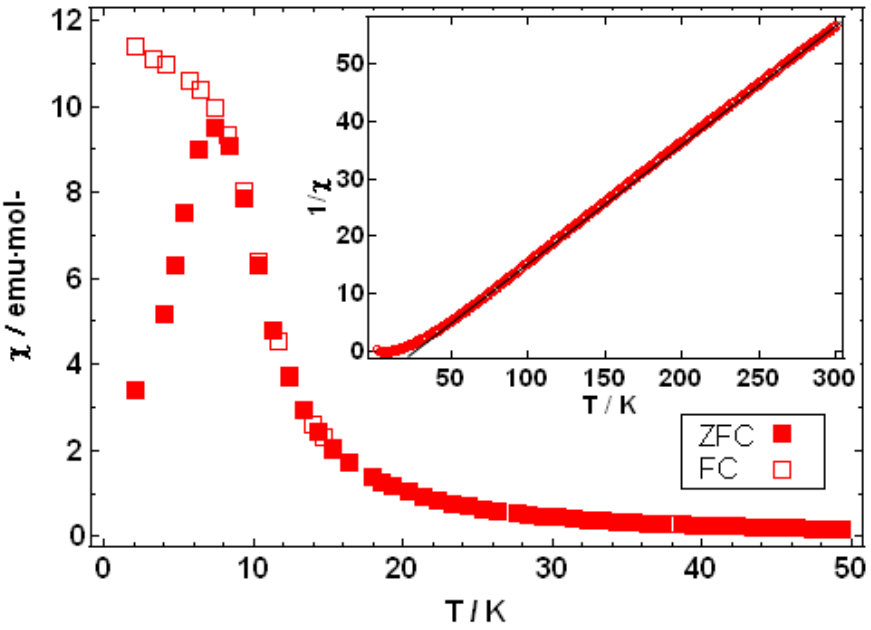

Table 3.4 Results of susceptibility measurements of $EuWO_{1+x}N_{2-x}$ (x = 0.41, -0.04 and -0.12).

x	0.41	-0.04	-0.12
C / emu·K·mol^{-1}	6.04	4.90	5.00
μ_{eff} / μ_B	6.96	6.27	6.34
θ / K	12.9	22.1	12.8
μ_{sat} / μ_B	5.48	3.50	3.38
T_C / K	12.3	11.3	11.5

Figure 3.7 Magnetization-field loops for $EuWO_{1+x}N_{2-x}$; x = 0.41, -0.04 and -0.12 at low temperatures

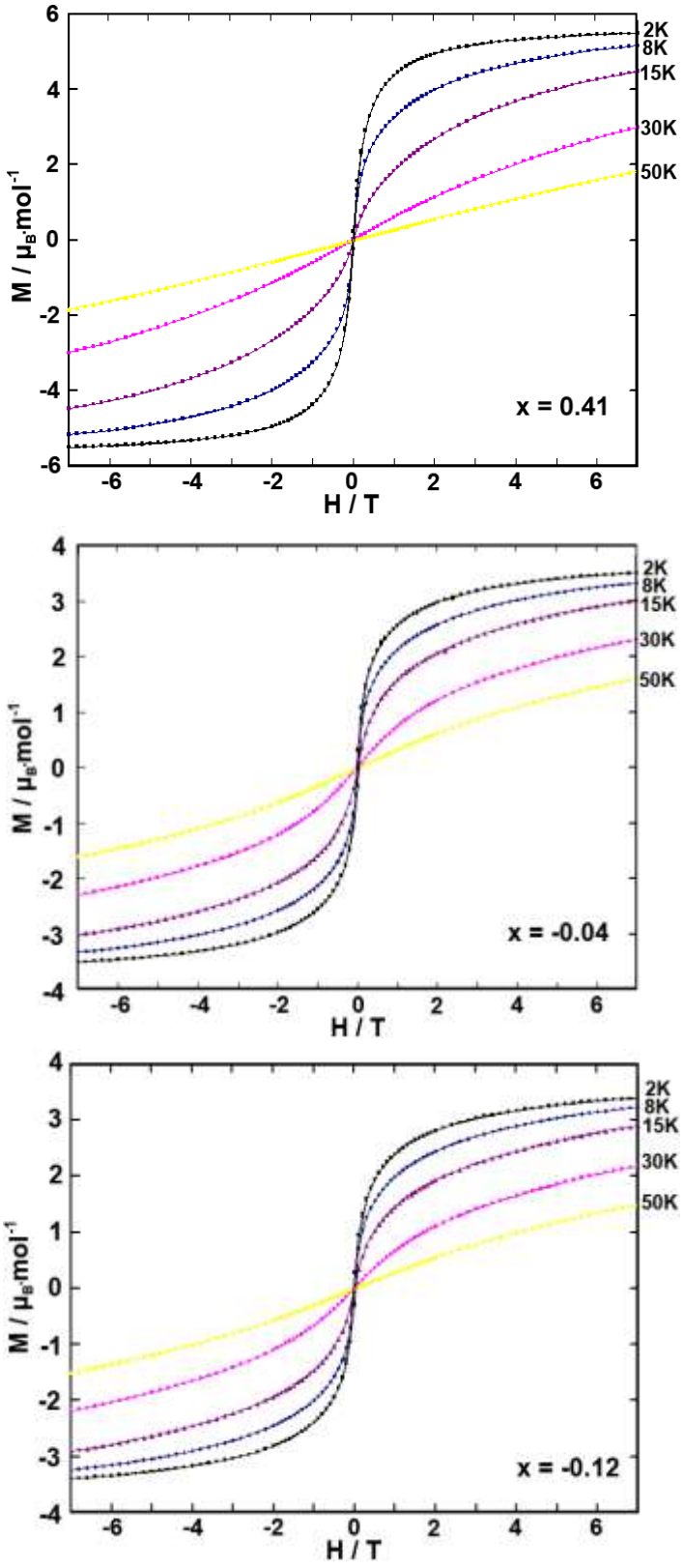

In the electron doped (x > 0) regime, the formal valence distribution is $Eu^{2+}W^{6+}_{1-x}W^{5+}_{x}O_{1+x}N_{2-x}$ so the magnetic moments are predicted to be close to the spin-only values of μ_{eff} = 7.9 μ_B and μ_{sat} = 7.0 μ_B for S = 7/2 Eu^{2+}. However, the hole doped (x < 0) materials have the nominal distribution $Eu^{2+}_{1+x}Eu^{3+}_{-x}W^{6+}O_{1+x}N_{2-x}$. Eu^{3+} has a non-magnetic (J = 0) ground state and although higher J states are thermally accessible, the moments become very small at low temperatures. Hence, the average Eu magnetic moments are expected to decrease in the hole doped region. This trend is borne out by the data in Table 3.4 as the hole-doped materials have smaller paramagnetic and saturated moments than those for the electron doped x = 0.41 sample and the previously reported x = 0.17 sample which has μ_{sat} = 4.1 μ_B, although there is little difference between the values for the x = -0.04 and -0.12 materials. All of the moments are below the predicted values, showing that more Eu^{3+} is present than expected from the chemical compositions. This evidences a significant influence of anion disorder on the electronic configurations. An ideal, anion ordered, x = 0 composition $EuWON_2$ would be expected to contain only Eu^{2+} and W^{6+} states, but anion disorder can create nitride-rich regions that stabilize oxidation of Eu^{2+} to Eu^{3+}, balanced by oxide-rich regions where W^{6+} is reduced to W^{5+}. Hence, inhomogeneity in the anion distribution controls the internal redox equilibrium:

$$Eu^{2+} + W^{6+} \Leftrightarrow Eu^{3+} + W^{5+}$$

3.3.4 Conducting properties

The three measured samples all show semiconducting behavior (Figure 3.8) although the heavily doped x = 0.41 sample has relatively little temperature dependence and is approaching metallic conductivity.

Figure 3.8 Temperature dependence of the electronic resistivities of $EuWO_{1+x}N_{2-x}$ (x = 0.41, -0.04 and -0.12) in zero field and in a magnetic field of 7 T. Resistivity values of $>10^9$ mΩcm for the x = -0.04 sample at low temperatures were unreliable and are not shown.

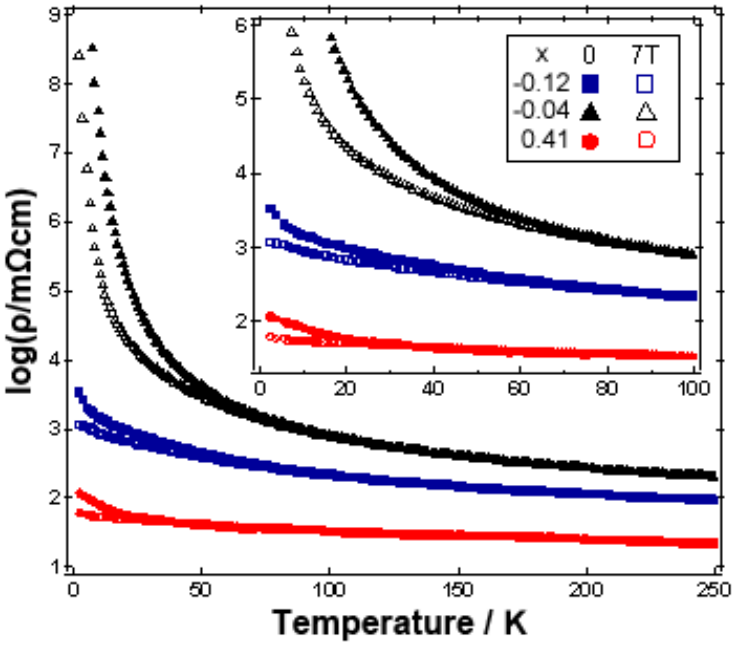

The zero field and 7 T resistivities diverge at low temperatures signifying the onset of significant negative magnetoresistance effects. Field-dependent measurements of the negative magnetoresistance $-MR = (\rho_0 - \rho_H) / \rho_0$, where ρ_0 and ρ_H are the resistivities in zero and applied field H respectively, are shown in Figure 3.9. The electron and hole-doped samples both show large magnetoresistances, approaching -50 and -70% at 2 K in a 7 T field. However, the x = -0.04 sample shows much larger, CMR effects with –MR > 99% at low temperatures. The maximum measurable value of –MR was 99.7% at 7 K in a 7 T field the zero field resistance was too high to be measured accurately at lower temperatures. Hence, $EuWO_{1+x}N_{2-x}$ is found to be a new CMR material at low temperatures, for dopings x close to zero (here x = -0.04).

Figure 3.9 Magnetic field variations of negative magnetoresistances ($-MR = (\rho_0 - \rho_H) / \rho_0$) for $EuWO_{1+x}N_{2-x}$ (x = 0.41, -0.04 and -0.12).

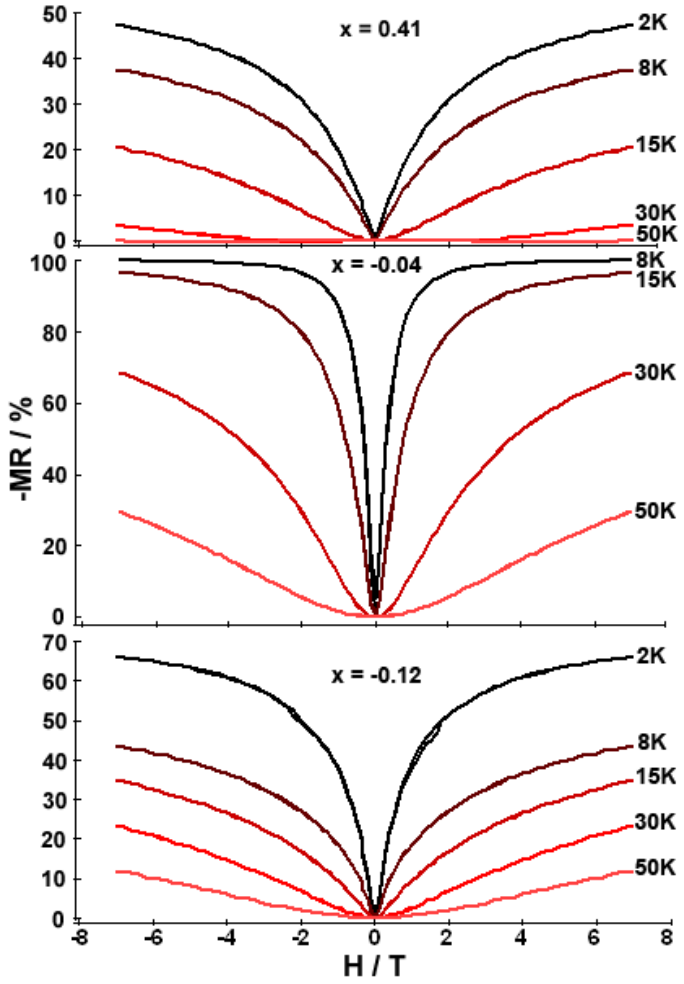

Resistivity data for the three $EuWO_{1+x}N_{2-x}$ samples measured in this work (x = 0.41, -0.04 and -0.12) and those for the previous published three electron-doped samples (x = 0.25, 0.18, and 0.09) are combined to show overall trends in Figures 3.10. The non-linear variations of log(resistivity) against inverse temperature show that these materials do not follow a simple activated semiconductor behaviour. The highest resistivities and the strongest temperature dependence are observed for the x = -0.04 sample which confirms that minimum doping occurs close to the ideal x = 0 composition. The bandgap for the x = -0.04 sample estimated from the slope of log(resistivity) at room temperature is 60 meV, showing that the $EuWO_{1+x}N_{2-x}$

materials have narrow bandgaps. The hole doped x = -0.12 material has a higher resistivity than samples with comparable magnitudes of electron doping (x = 0.09 and 0.17). This is in keeping with the expected carrier mobilities, as f-band holes are expected to be less mobile than the 5d-band electrons, i.e. Eu^{2+}-Eu^{3+} electron transfer is less rapid than W^{5+}-W^{6+} transfer. Resistivity decreases as hole or electron doping increases, although the x = 0.41 material has an anomalously high resistivity that may reflect some electrical inhomogeneity close to the upper limit of nitrogen deficiency.

Figure 3.10 Variations of zero field resistivity for hole and electron doped $EuWO_{1+x}N_{2-x}$ perovskites, plotted as $\log_{10}$(resistivity) against inverse temperature.

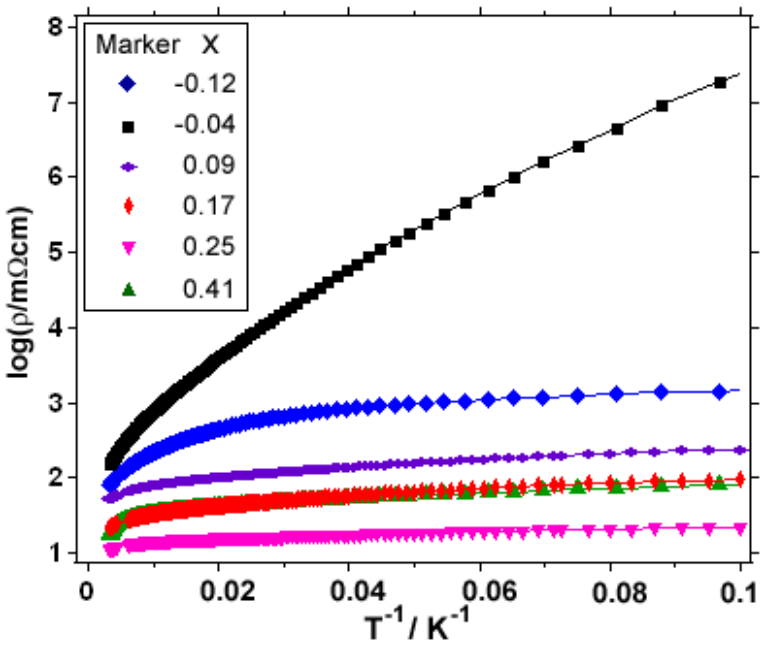

The compositional trends in low temperature magnetoresistance follow the resistivity variations, as illustrated by Figure 3.11. The most resistive x = -0.04 sample is the only one to show a CMR effect in high fields. This material also shows a very rapid rise in –MR at low fields. The low field (0.1 T) value of -MR is 13% for the latter sample at 8 K but <3% for all other samples. Low field magnetoresistances of

ceramic materials are often dominated by the magnetotransport of carriers across the boundaries between different grains or magnetic domains. These effects are more dependent on sample microstructure than composition and so do not follow simple chemical trends. Hence the observed variation strongly indicates that the low field magnetoresistance is intrinsic to the $EuWO_{1+x}N_{2-x}$ materials rather than of microstructural origin. This also demonstrates that the intrinsic electronic properties of the 'undoped' x = 0 material are apparent despite any additional carriers introduced by anion disorder.

Figure 3.11 Compositional variations for $EuWO_{1+x}N_{2-x}$ of 250 K resistivity, high field (7 T) magnetoresistances at 2 and 8 K, and low field (0.1 T) magnetoresistance at 8 K.

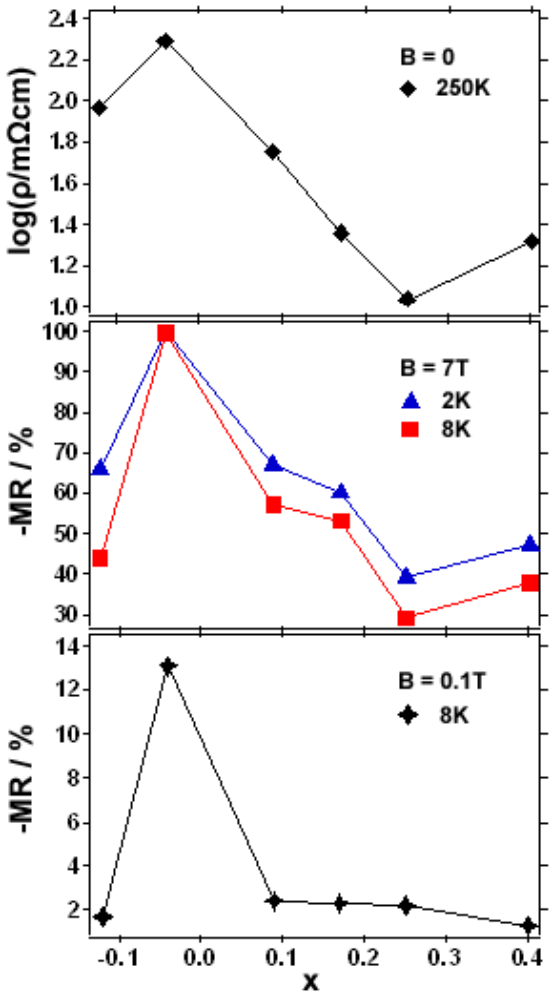

3.3.5 Diffraction study

3.3.5.1 TEM

Superstructures are evident in the electron diffraction patterns of individual $EuWO_{1+x}N_{2-x}$ crystallites, as shown in Figure 3.12. These contain additional reflections characteristic of a tetragonal √2 x √2 x 2 body-centred perovskite superstructure for the N-rich x = -0.04 and -0.12 samples. This superstructure was also observed in the previously reported x = 0.09 and 0.25 samples, and in the $EuNbO_2N$ and $EuTaO_2N$ analogues,[3] but it is notably absent for the most non-stoichiometric, x = 0.41 sample. Powder neutron diffraction studies of $SrNbO_2N$[12] and $SrTaO_2N$[13, 14] have shown that a tetragonal √2 x √2 x 2 body-centred (I4/mcm symmetry) superstructure results from octahedral tilting with partial anion order in most refinements. It is likely that such superstructures are also formed in $EuWO_{1+x}N_{2-x}$ although the high degree of disorder present for the x = 0.41 sample suppresses the octahedral tilting transition to below room temperature.

Figure 3.12 Electron diffraction patterns of representative crystallites of $EuWO_{1+x}N_{2-x}$ samples with x = -0.12, -0.04 and 0.41.

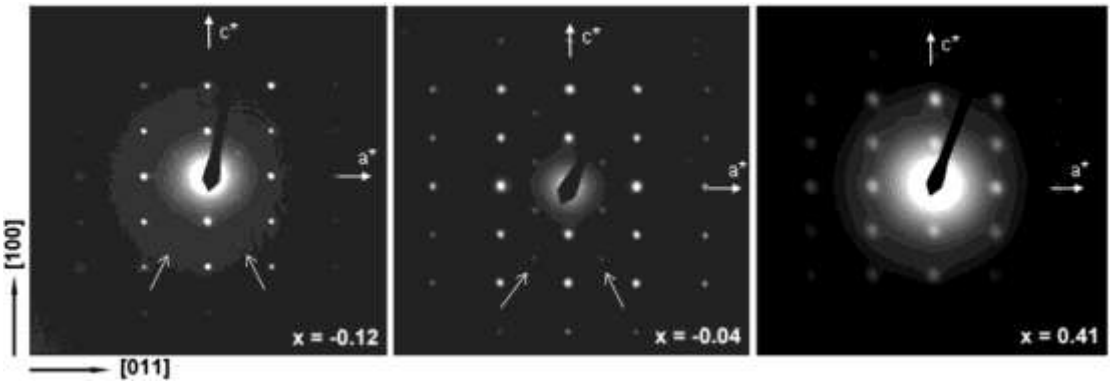

3.3.5.2 TOF neutron powder diffraction

These diffraction patterns were collected from 2 to 18 K and fitted in the tetragonal space group (I4/mcm) in order to resolve any superstructure, such as may arise from anion ordering. Table 3.5 shows the summary of neutron refinement results. It was not possible to achieve any reliable chemical composition refinement because of the high sample absorption. The occupancies of O/N were thus given as disordered at each site according to the chemical analysis results.

According to the magnetization measurements, a ferromagnetic transition is expected below $T_C = 12 \pm 1$ K. However, 2 and 18 K neutron patterns (Figure 3.13) are virtually identical and no additional magnetic diffraction is evident at 2 K. Attempts to fit a ferromagnetic model give moments less than 1 μ_B and no improvement to the fit. This suggests that the magnetic moment observed in magnetization measurements was induced by the external field, but without an external field in the neutron experiment, there is no magnetic diffraction observed.

Table 3.5 Refinement results of neutron powder diffraction of $EuWO_{1.17}N_{1.83}$ at 2, 6 10, 14 and 18 K in space group I4/mcm. The atomic positions are Eu: (0, 0.5, 0.25); W: (0.5, 0.5, 0); O/N(1): (x, y, 0); O/N(2): (0, 0, 0.25).

T / K	2	6	10	14	18
a / Å	5.5918(1)	5.5923(5)	5.5922(2)	5.5900(1)	5.5928(3)
c / Å	7.9240(3)	7.9238(10)	7.9244(5)	7.9225(3)	7.9261(7)
V / $Å^3$	247.77(1)	247.80(7)	247.82(2)	247.57(1)	247.92(3)
x: O/N(1)	0.7751(1)	0.7750(1)	0.7750(1)	0.7750(1)	0.7747(1)
y: O/N(1)	0.2751(1)	0.2750(1)	0.2750(1)	0.2750(1)	0.2747(1)
Eu: Uiso / $Å^2$	0.00305(15)	0.00329(25)	0.00288(18)	0.00326(13)	0.00338(37)
W: Uiso / $Å^2$	0.00677(22)	0.00633(31)	0.00586(24)	0.00661(20)	0.00655(38)
O/N: Uiso/$Å^2$	0.01762(11)	0.01726(21)	0.01639(12)	0.01740(9)	0.01758(35)
Eu-O/N1(×4) / Å	2.6622(6)	2.6627(7)	2.6628(6)	2.6616(6)	2.6649(7)
Eu-O/N1(×4) / Å	2.9424(7)	2.9420(8)	2.9421(7)	2.9415(6)	2.9407(7)
Eu-O/N2(×4) / Å	2.79593(8)	2.79615(29)	2.79611(10)	2.79504(6)	2.79640(19)
<Eu-O/N> / Å	2.8001(5)	2.8003(6)	2.8003(5)	2.7994(4)	2.8007(5)
W-O/N1(×4) / Å	1.98696(10)	1.98706(23)	1.98702(12)	1.98631(9)	1.98699(16)
W-O/N2(×2) / Å	1.98102(10)	1.98095(27)	1.98112(13)	1.98064(8)	1.98154(19)
<W-O/N>/ Å	1.9850(1)	1.9850(3)	1.9851(1)	1.9844(1)	1.9852(2)
R_p	0.0127	0.0128	0.0126	0.0124	0.0112
R_{wp}	0.0226	0.0230	0.0232	0.0218	0.0197
χ^2	4.997	5.166	5.288	4.661	3.833

Figure 3.13 Fit of tetragonal (I4/mcm) model for $EuWO_{1.17}N_{1.83}$ to neutron powder diffraction at 2 and 18 K. Regions containing scattering from the cryostat have been excluded.

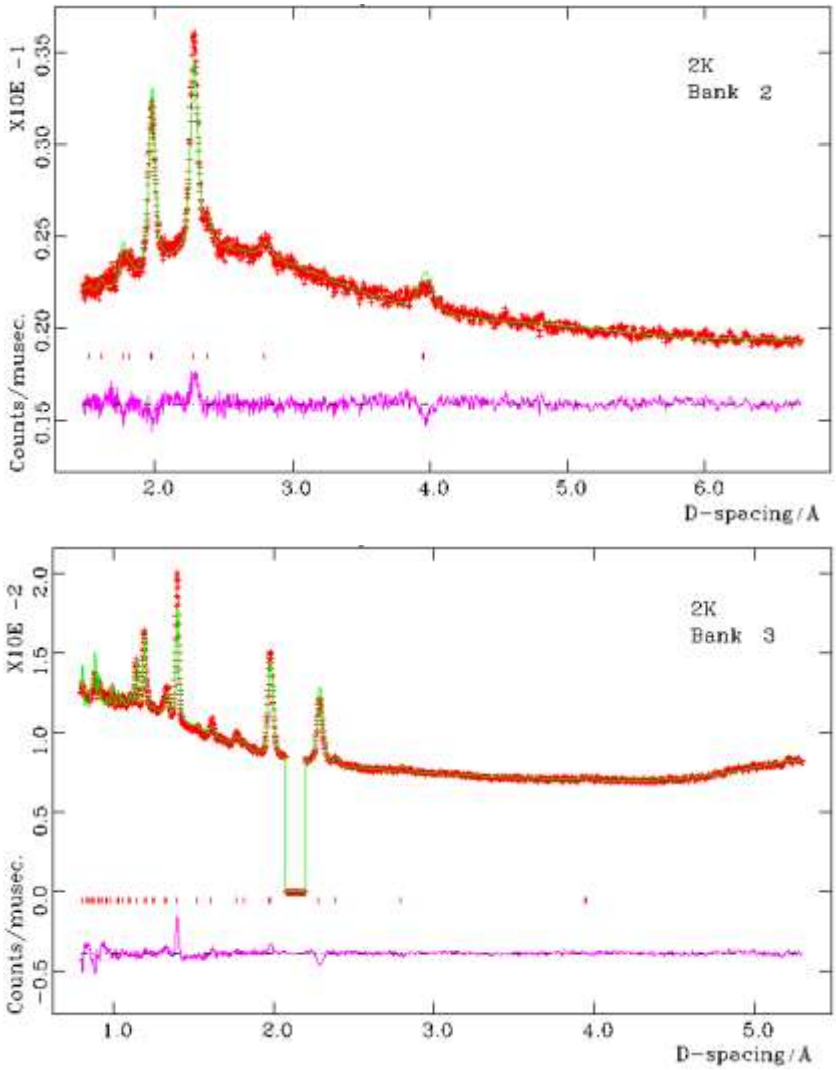

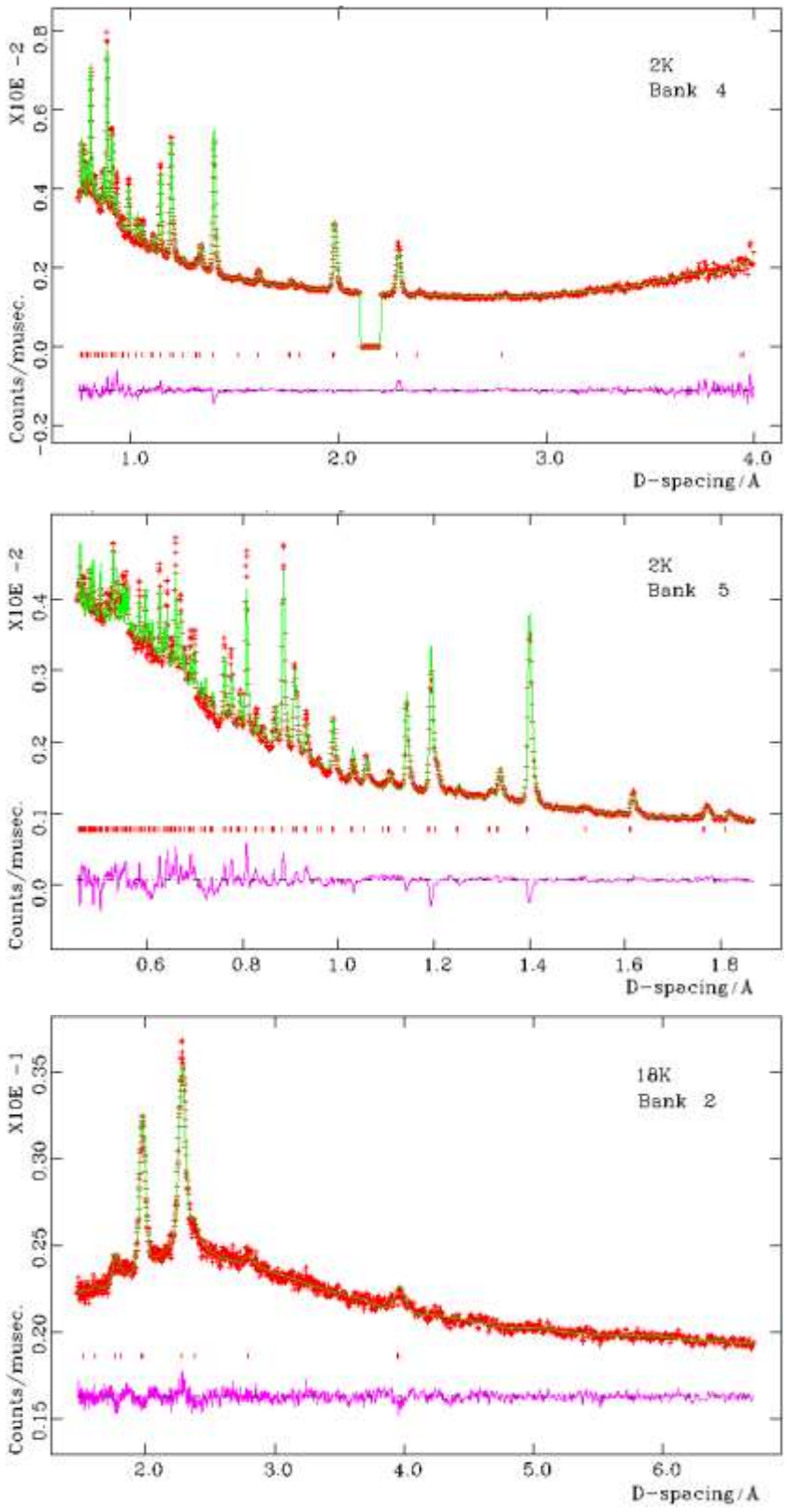
2K
Bank 4
X10E -2
Counts/musec.
D-spacing/A
2K
Bank 5
X10E -2
Counts/musec.
D-spacing/A
18K
Bank 2
X10E -1
Counts/musec.
D-spacing/A

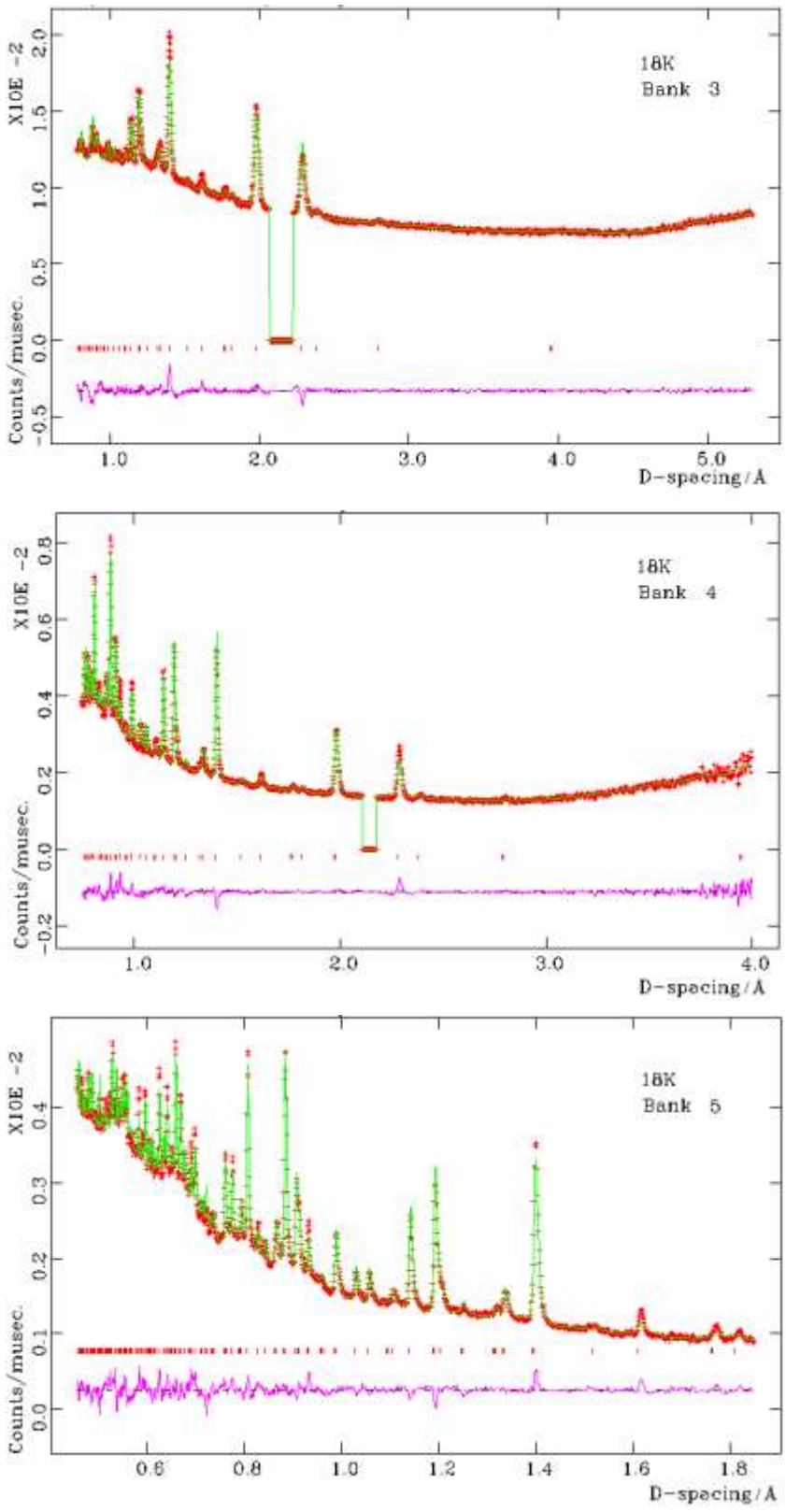
18K
Bank 3
X10E -2
Counts/musec.
D-spacing/Å
18K
Bank 4
X10E -2
Counts/musec.
D-spacing/Å
18K
Bank 5
X10E -2
Counts/musec.
D-spacing/Å

3.4 Conclusions

A wide range of $EuWO_{1+x}N_{2-x}$ materials ($-0.16 \leq x \leq 0.46$) have been synthesized by thermal ammonolysis of a $Eu_2W_2O_9$ precursor. A scheelite intermediate phase $EuWO_{4-y}N_y$, containing mixed valence Eu^{2+}/Eu^{3+}, has been discovered. A linear relationship between the lattice parameter and nitrogen content of $EuWO_{1+x}N_{2-x}$ was observed. Apparent ferromagnetic ordering below a Curie temperature $T_C = 12 \pm 1$ K and large negative magnetoresistances have been discovered in these samples. In particular, for the least doped sample, $EuWO_{0.96}N_{2.04}$, CMR $\geq$ 99.7% was observed at 7 K. The possibility of tuning the physical properties by altering the chemical composition has been demonstrated. The structure of $EuWO_{1.17}N_{1.83}$ was studied by neutron diffraction between 2 to 18 K and an I4/mcm superstructure was confirmed. However, no additional magnetic diffraction is evident at 2 K suggesting that the apparent ferromagnetism may be induced by small external fields.

This research has led to the following publications:

[1] Minghui Yang, J. Oró-Solé, A. Kusmartsva, A. Fuertes and J. Paul Attfield, Electronic Tuning of Two Metals and Colossal Magnetoresistances in $EuWO_{1+x}N_{2-x}$ Perovskites, *J. Am. Chem. Soc.* 2010, 132, 4822.

[2] A. Kusmartsva, Minghui Yang, J. Oró-Solé, A. B. Jorge, A. Fuertes and J. Paul Attfield, *Appl. Phys. Lett.* 2009, 95, 022110.

3.5 References

1. R. Asahi, T. Morikawa, T. Ohwaki, K. Aoki, Y. Taga, *Science* 2001, 293, 269.
2. Y. Kim, P.M.Woodward, P.M., K.Z. Baba-Kishi, C.W. Tai. *Chem. Mater.* 2004, 16, 1267.
3. A. B. Jorge, J. Oró-Solé, A. M. Bea, N. Mufti, T. T. M. Palstra, J. A. Rodgers, J. P. Attfield and A. Fuertes, *J. Am. Chem. Soc.* 2008, 130, 12572.
4. M. Jansen and H. P. Letschert. *Nature* 2000, 404, 980.
5. M. Highashi, R. Abe, T. Takata, K. Domen. *Chem. Mater.* 2009, 21, 1543.
6. K. Maeda, K. Teramura, D. Lu, T. Takata, N. Saito, Y. Inoue and K. Domen, *Nature* 2006, 440, 295.
7. R. Pastrana-Fabregas, J. Isasi-Marin, C. Cascales, R. Saez-Puche, *J. Solid State Chem.* 2007, 180, 92.
8. A. C. Larson and R. B. von Dreele, "General Structure Analysis System (GSAS)", Los Alamos National Laboratory Report LAUR 86-748 (1994).
9. G. J. McCarthy, R. D. Fischer, J. Sanzgiri, *J. Solid State Chem.* 1971, 5, 200.
10. P. Antoine, R. Marchand, Y. Laurent, *Rev. Int. Hautes Temp. Refract. Fr.* 1987, 24, 43.
11. R. D. Shannon, *Acta Cryst. A* 1976, 32, 751.
12. S. G. Ebbinghaus, A. Weidenkaff, A. Rachel, A. Reller, *Acta Cryst. C* 2004, 60, i91.
13. S. J. Clarke, K. A. Hardstone, C. W. Michie, M. J. Rosseinsky, *Chem. Mater.* 2002, 14, 2664.
14. E. Gunther, R. Hagenmayer, M. Jansen, *Z. Anorg. Allg. Chem.* 2000, 626, 1519.

Chapter 4. High pressure synthesis of $RZrO_2N$ (R = Pr, Nd and Sm) perovskites

4.1 Introduction

Quaternary oxynitrides containing rare earth cations and transition metals may show interesting electronic,[1, 2] optical[3] and catalytical[4, 5] properties (see Chapter 1). Zirconium rare earth oxynitride perovskites - $RZrO_2N$ (R = trivalent rare earth) are potential multiferroic materials as they contain both magnetic R^{3+} and d^0 Zr^{4+}. A previous investigation showed that $LaZrO_2N$ could be synthesized by repeated ammonolysis of a highly reactive amorphous $La_2Zr_2O_7$ precursor at 1000 °C, but the other R analogues were not accessible.[6]

High pressure synthesis is a well established method in perovskite synthesis. The use of high pressure is expected to be a general and very convenient approach in oxynitride synthesis since it suppresses the decomposition to oxides and nitrogen gas and it should be useful for the stabilization of new phases at moderate temperatures. High pressure is also expected to stabilize oxynitride structures with high coordination numbers for cations and anions as for instance perovskites. Few examples of oxynitrides perovskites have been reported by using high pressure synthesis. For instance, the spinel Ga_3O_3N has been synthesized by direct solid state reaction of Ga_2O_3 and GaN at 1500 – 1700 °C under an applied pressure of 5 GPa.[7] La_2VO_3N and $BaNbO_2N$ are the only reported examples of quaternary oxynitrides synthesized by high pressure.[8]

In this work, three new oxynitride perovskites, $RZrO_2N$ (R = Pr, Nd and Sm) have

been synthesized using high pressure high temperature (HPHT) methods, starting from 1:1 mixtures of rare earth oxides and zirconium oxynitride, Zr_2ON_2, which was used as the nitrogen source:

$$R_2O_3 + Zr_2ON_2 \rightarrow 2RZrO_2N \qquad (4.1)$$

4.2 Experimental

4.2.1 Precursors

Pr_2O_3 was prepared by reducing Pr_6O_{11} (Aldrich Chemical Co., 99.999 %) under 5% H_2/N_2 at 1100-1200 °C for 24 hr. The purity of Pr_2O_3 was checked by powder X-ray diffraction and structure refinement. Both Nd_2O_3 and Sm_2O_3 were commercially available (Aldrich Chemical Co., 99.99%), and were dried overnight at 800 °C before use.

Zr_2ON_2 was prepared by treatment of ZrO_2 (Aldrich Chemical Co., 99.99%) under NH_3 (99.98%, BOC) at a flow rate of 670 cm^3/min. Samples were treated at 1000 °C for 24 hr and then rapidly cooled at room temperature in ammonia.[9] Their purity was checked by powder X-ray diffraction and their nitrogen contents were determined by elemental analysis (Carlo Erba instrument) and thermogravimetric analysis (Perkin Elmer) in an oxygen atmosphere. The samples selected for the high pressure experiments showed nitrogen contents between 2.01 and 1.97 moles per formula.

4.2.2 HPHT synthesis

High pressure high temperature (HPHT) reactions have been achieved by using a

Walker module multi-anvil press.[10, 11] For these experiments with a 6-8 type (anvils and cubes respectively) Walker module and graphite heating components, the press can achieve conditions up to 15 GPa, and 1500 °C. According to Reaction 4.1, a 1:1 mixture of R_2O_3 and Zr_2ON_2 with a total mass of about 25 mg was finely ground and transferred to a boron nitride capsule, and then loaded into the press using the experimental setup shown in Figure 4.1. The pressure was generated over 2 hr, and reactants were heated to the temperature (see specific reactions conditions in Table 1) in the following 10 min. The samples were quenched to room temperature, and the pressure was released over about 8 hr. After decompression, the product in the octahedral assembly was carefully separated from the surrounding boron nitride. All the products were light blue in colour and stable in air.

Figure 4.1 Experimental setup for HPHT synthesis

4.2.3 Structure characterizations

The products were finely ground and then examined by powder X-ray diffraction using a θ-2θ diffractometer with monochromatic $CuK_{\alpha 1}$ radiation (λ = 1.540562) in reflection geometry. Scans were taken in the range of 2θ, 15-115° at 0.007° step size, and with 3 s count times. The structures were refined using least square refinement in GSAS.[12]

4.3 Results and discussion

4.3.1 Synthesis results

Table 4.1 shows a summary of the HPHT synthesis of $RZrO_2N$. As the starting point of this study, a wide range of the reaction conditions have been applied to Nd_2O_3 and Zr_2ON_2. At pressures above 6 GPa, mixtures of ZrN and various metal oxides were formed. At pressure of 1 – 2.5 GPa and temperature above 1200 °C, mixtures of ZrN, the new perovskite $NdZrO_2N$, and pyrochlore phase were observed. There is no sign of perovskite phase formation at low temperatures such as 800 °C. At higher temperatures, the yield of the perovskite phase was lower, suggesting that the perovskite phase is decomposed. Similar conditions were applied to the synthesis of $SmZrO_2N$ which was only obtained at pressures of 2.5 – 3 GPa and temperature around 1500 °C. Similar conditions to the $NdZrO_2N$ synthesis were used to obtain a $PrZrO_2N$ sample.

Comparing the reaction products for these syntheses clearly indicates that the temperature is important. The temperature must be high enough to promote the diffusion of R^{3+} and Zr^{4+} cations during the reaction, but reactions at too high a temperature give a relatively large degree of decomposition of the perovskite phase,

for instance 25% of the $NdZrO_2N$ decomposed at 1500 °C relative to reaction at 1200 °C, as shown in Table 4.1.

The tolerance factors (see Chapter 1) of $RZrO_2N$ (R = Pr, Nd, and Sm) are 0.88 to 0.89. These values are low but within the typical range $0.85 < t < 1.05$ for ambient pressure perovskites. Hence, the role of the applied pressure is mainly to prevent nitrogen loss during the course of the reaction. Reaction time has a very small effect on the observed products. However, for too long a reaction time, the perovskite phases are observed to decompose slightly.

The cubic lattice parameter of the pyrochlore phase was found in R = Nd and Sm synthesis, to vary in the ranges 10.62 – 10.70 Å and 10.58 – 10.61 Å, around the values of 10.68 Å and 10.59 Å for $Nd_2Zr_2O_7$ and $Sm_2Zr_2O_7$, respectively. This indicates that the pyrochlore has a variable composition and so may also be a quaternary oxynitride, $R_2Zr_2O_{7-x}N_{2x/3}$, as rare earth transition metal oxide pyrochlores are known to accommodate substantial nitride contents e.g. $Sm_2Mo_2O_{3.83}N_{3.17}$,[13] see also Chapter 5. Reflections for ZrN were weak due to the relatively low phase fractions in the samples (less than 10%). They can be indexed by a cubic unit cell with experimental parameter a = 4.5684(2) Å. The sums of metals in the crystalline products were not balanced, indicating the existence of other unidentified impurities or amorphous phases.

Table 4.1 Conditions and results of $RZrO_2N$ (R = Pr, Nd, and Sm) syntheses

	Conditions			Results
	T / °C	P / GPa	Heating / hr	
Nd	1200	6	0.25	Unknown phases
	1200	6	0.25	Unknown phases
	1200	10	0.25	Unknown phases
	1200	10	1	Unknown phases
	1200	2	0.25	50% $NdZrO_2N$, 40.1%$Nd_2Zr_2O_7$, 9.9%ZrN
	1200	2.5	0.25	50.6% $NdZrO_2N$, 42.1%$Nd_2Zr_2O_7$, 7.3%ZrN
	1200	1	0.25	49.7% $NdZrO_2N$, 42.8%$Nd_2Zr_2O_7$, 7.5%ZrN
	**1200	2	1	68.9% $NdZrO_2N$, 27.8%$Nd_2Zr_2O_7$, 3.3%ZrN
	1200	2	2	70.7% $NdZrO_2N$, 29.3%$Nd_2Zr_2O_7$, unknown
	1500	2	1	45.3% $NdZrO_2N$, 47%$Nd_2Zr_2O_7$, 7.6%ZrN
	*1200	2	1	71.8% $NdZrO_2N$, 28.2%$Nd_2Zr_2O_7$, unknown
	800	2	1	Unknown phases
Sm	1200	2	1	Unknown phases
	1200	5	1	Unknown phases
	1200	3.5	1	Unknown phases
	1200	7	1	Unknown phases
	1200	10	3	Unknown phases
	1350	2.5	3	Unknown phases
	1500	2.5	0.25	44% $SmZrO_2N$, 45%$Sm_2Zr_2O_7$, 11%ZrN
	**1500	3	0.5	43.3% $SmZrO_2N$, 50.2%$Sm_2Zr_2O_7$, 6.5%ZrN
Pr	**1150	2	1	42.9% $PrZrO_2N$, 48.9%$Pr_2Zr_2O_7$, 8.2%ZrN

Note: the samples are quenched after heating, except the * sample was slow cooled in 1 hr. ** samples were selected for the structure refinements.

4.3.2 Structure characterization of $RZrO_2N$

Selected Rietveld refinement of the powder X-ray patterns of the best samples are shown in Figure 4.2. All the patterns were fitted well with a mixture of perovskite, pyrochlore and ZrN phases. All three new $RZrO_2N$ perovskites crystallize in the orthorhombic Pnma superstructure as shown in Figure 4.3. The summary of refined lattice parameters and atomic positions are shown in Tables 4.2 and 4.3. No evidence of O/N order over the two available anion sites was found.

Figure 4.2 Refinement of the structure of $RZrO_2N$ against powder X-ray diffraction data. The different phases are represented by the vertical bars, from top to bottom these correspond to ZrN, $R_2Zr_2O_7$ and $RZrO_2N$.

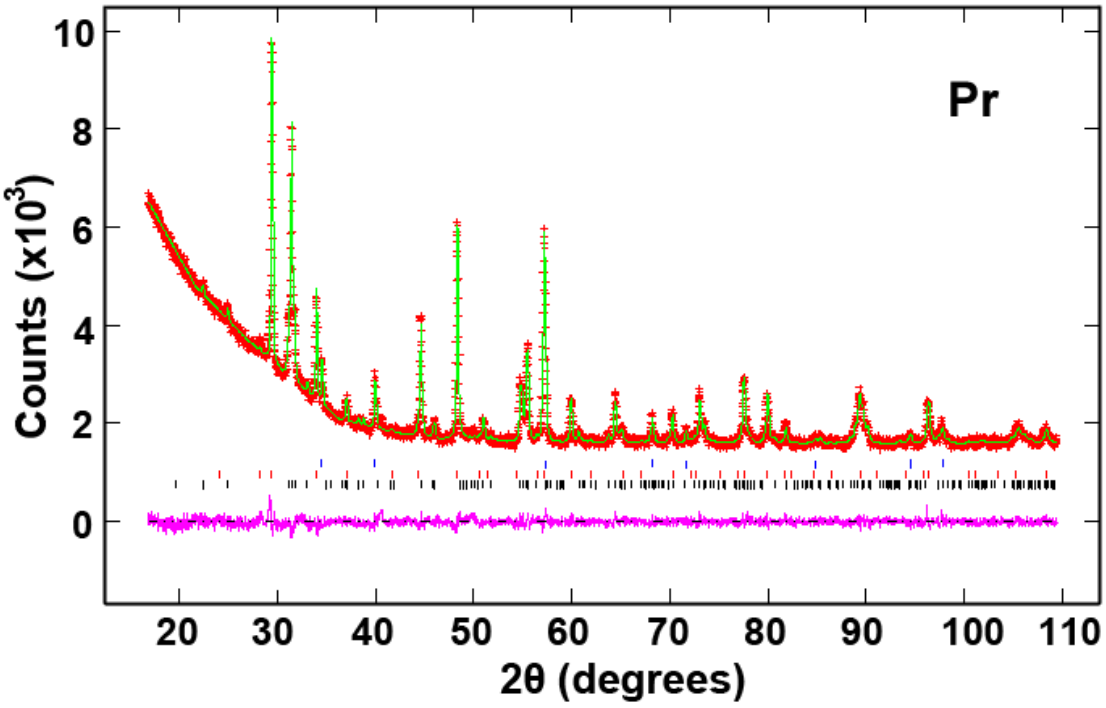

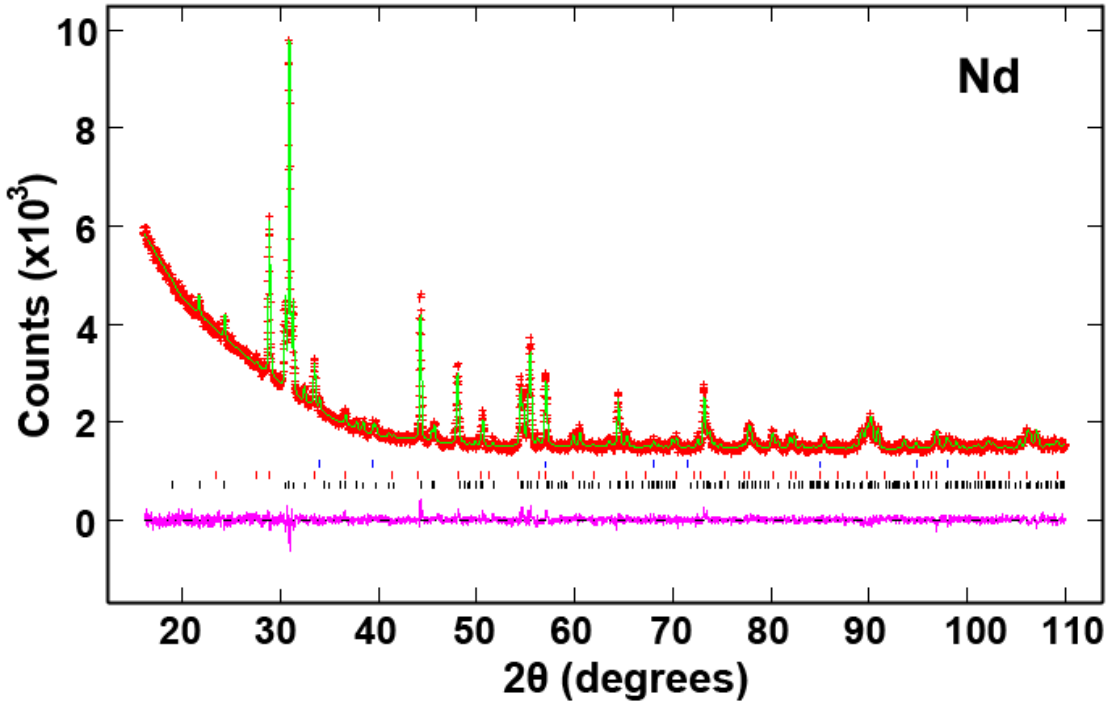
Nd
Counts (x10^3)
2θ (degrees)
0
2
4
6
8
10
20
30
40
50
60
70
80
90
100
110

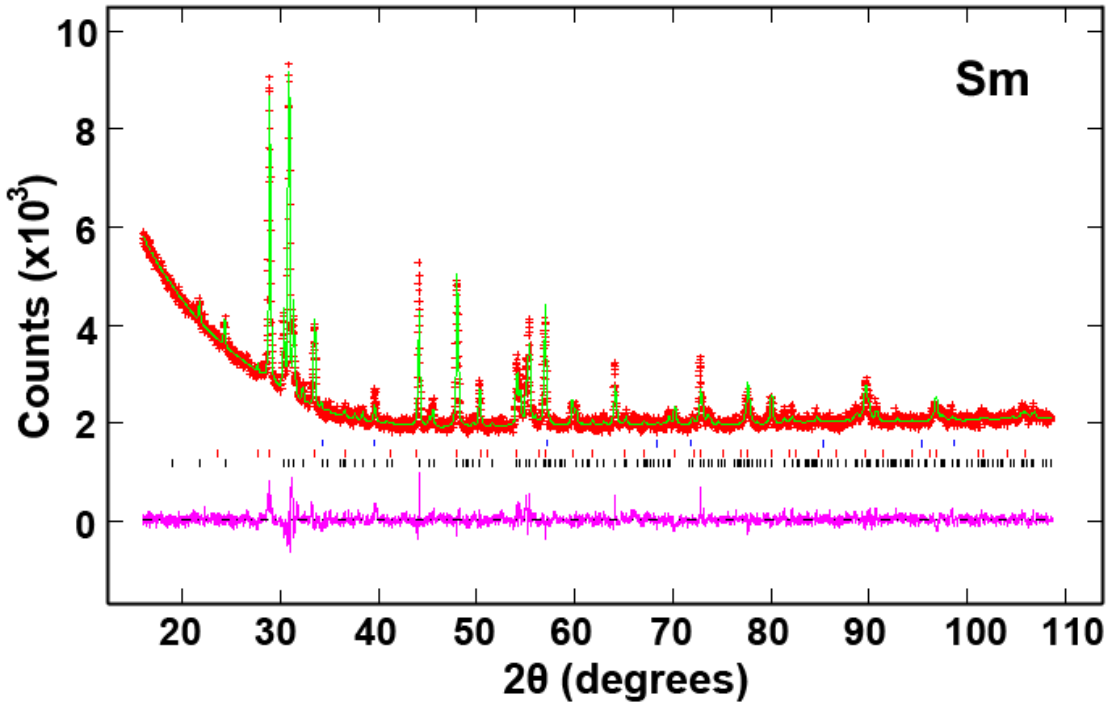
Sm
Counts (x10^3)
2θ (degrees)
0
2
4
6
8
10
20
30
40
50
60
70
80
90
100
110

Figure 4.3 Structure of $RZrO_2N$

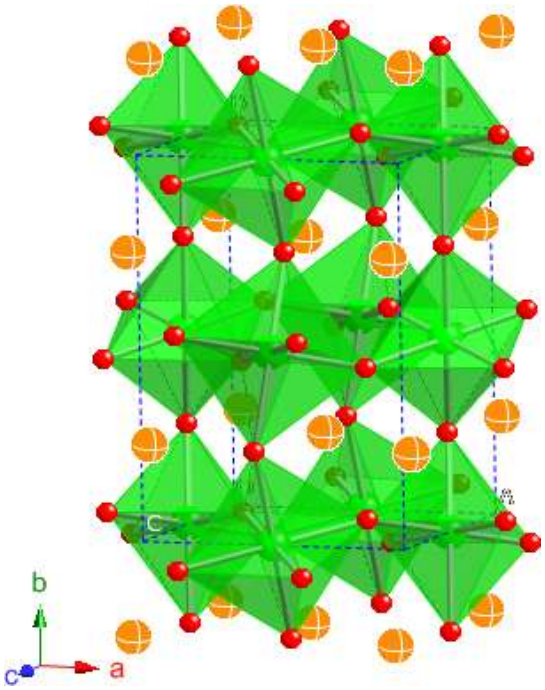

Table 4.2 Refined lattice parameters and residuals for $RZrO_2N$ (R = Pr, Nd, and Sm)

	$PrZrO_2N$	$NdZrO_2N$	$SmZrO_2N$
a / Å	5.8440(2)	5.8537(1)	5.8423(2)
b / Å	8.1808(2)	8.1707(1)	8.1281(3)
c / Å	5.7335(1)	5.7093(1)	5.6621(1)
V / $Å^3$	274.12(1)	273.07(1)	268.88(1)
R_p	0.0181	0.0197	0.0190
R_{wp}	0.0238	0.0253	0.0246
$\chi 2$	1.428	1.340	1.532

Table 4.3 Atomic positions for $RZrO_2N$* (R = Pr, Nd, and Sm)

Variables	Pr	Nd	Sm
R: x	0.0442(4)	0.0469(2)	0.0549(5)
R: z	0.9799(7)	0.9857(4)	0.998(2)
R: Uiso / $Å^2$	0.027(1)	0.020(1)	0.023(8)
Zr: Uiso / $Å^2$	0.009(1)	0.015(1)	0.025(1)
O/N(1): x	0.466(4)	0.465(2)	0.469(6)
O/N(1): z	0.103(3)	0.112(2)	0.126(4)
O/N(2): x	0.301(3)	0.314(2)	0.331(4)
O/N(2):y	0.061(2)	0.049(1)	0.044(3)
O/N(2): z	0.689(2)	0.690(2)	0.650(4)
O/N(1/2): Uiso / $Å^2$	0.005(3)	0.012(3)	0.011(3)

* Atomic positions are R: (x, 0.25, z); Zr: (0.5, 0, 0); O/N(1): (x, 0.25, z); O/N(2): (x, y, z).

The plot of cell parameters against R^{3+} radius in Figure 4.4 demonstrates that the orthorhombic structural distortion increases as R^{3+} becomes smaller. The eight-fold coordination environment of R^{3+} becomes more distorted as the average <R-O/N> distance decreases from R = Pr to Sm. This results in increasing deformations and tilting of the $Zr(O/N)_6$ octahedra, as shown by the bond distances and angles in Table 4.4 and Figure 4.4. The Zr-O/N-Zr angles are reduced from 180 ° in the ideal perovskite structure to 136 °in $SmZrO_2N$.

Figure 4.4 Plots of cell parameters and volume against ionic radius R^{3+}: Sm, Nd and Pr (from experimental), La (from literature[6])

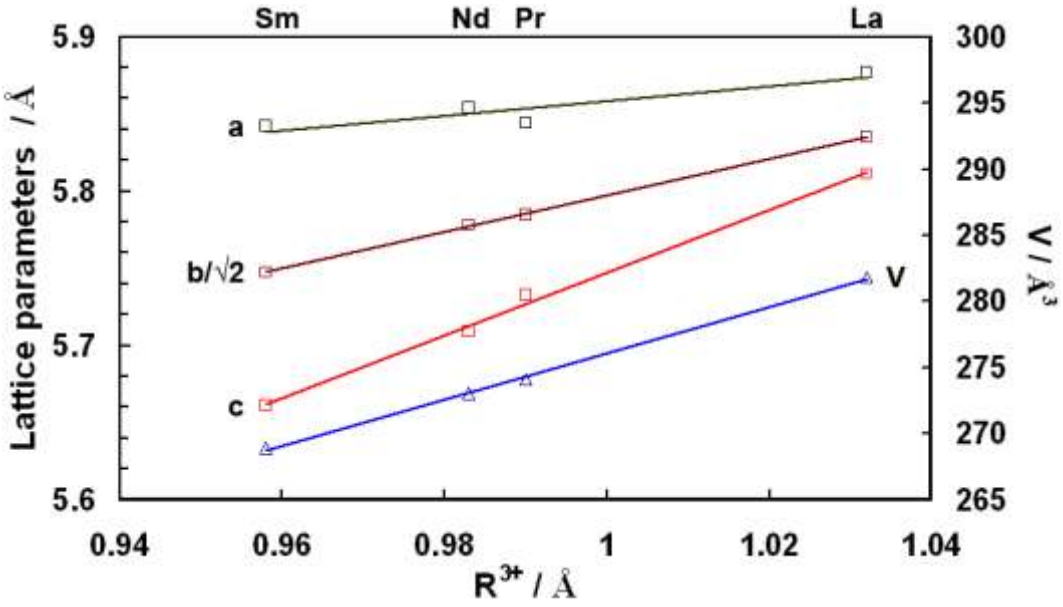

Table 4.4 Selected Interatomic Distances and Angles for $RZrO_2N$ (R = Pr, Nd, and Sm)

Dis. (Å) / Ang. (deg)	Pr	Nd	Sm
Zr_O/N1 (×2)	2.13(1)	2.15(1)	2.16(1)
Zr_O/N2 (×2)	2.13(1)	2.11(1)	2.14(2)
Zr_O/N2 (×2)	2.18(1)	2.17(1)	2.24(2)
<Zr-O/N>	2.15(1)	2.14(1)	2.18(2)
R_O/N1 (×1)	2.43(2)	2.34(1)	2.18(3)
R_O/N1 (×1)	2.56(2)	2.55(1)	2.53(4)
R_O/N2 (×2)	2.31(1)	2.35(1)	2.27(2)
R_O/N2 (×2)	2.71(1)	2.82(1)	2.63(2)
R_O/N2 (×2)	2.96(2)	2.83(1)	3.04(2)
<R-O/N>	2.62(1)	2.61(1)	2.55(2)
Zr_O/N1_Zr	146.0(1)	143.4(7)	140.1(1)
Zr_O/N2_Zr	143.2(8)	144.9(5)	136.0(1)

4.4 Conclusions

New oxynitrides of $RZrO_2N$ (R = Pr, Nd and Sm) have been synthesised via a solid state reaction of rare earth oxide with Zr_2ON_2 at 1200-1500 °C under 2-3 GPa pressure. A comparative structural study of this new series of oxynitrides has been performed by Rietveld refinement using powder X-ray diffraction data, which indicates that $RZrO_2N$ has a distorted perovskite structure in orthorhombic space group Pnma. An increased structural distortion with decreasing R^{3+} ionic radius has been discovered.

This study shows that new mixed metal oxynitrides are accessible by direct solid state reaction between metal oxides and oxynitrides at high pressures. The high temperatures needed to promote diffusion of R^{3+} and Zr^{4+} cations would lead to nitrogen loss at ambient pressure, but the application of pressures of 1 – 3 GPa has enabled the $RZrO_2N$ phases to be obtained as the majority products. This method may lead to the discovery of many new mixed metal oxynitrides. Unfortunately, the very stable secondary pyrochlore phases also appear to accommodate nitrogen, and so are also formed in competition with the perovskite under the investigated high pressure reaction conditions. The physical properties of these new oxynitrides were not studied due to the presence of secondary phases.

This research has led to the following publication:

Minghui Yang, J. Rodgers, L. C. Middler, J. Oró-Soléb, A. B. Jorge, A. Fuertes and J. Paul. Attfield, Direct solid state synthesis at high pressures of new mixed metal oxynitrides; $RZrO_2N$ (R = Pr, Nd, and Sm), *Inorg. Chem.* 2009, 48, 11498.

4.5 References

1. Y. Kim, P. M.Woodward, P. M., K. Z. Baba-Kishi, C. W. Tai. *Chem. Mater.* 2004, 16, 1267.
2. A. B. Jorge, J. Oró-Solé, A. M. Bea, N. Mufti, T. T. M. Palstra, J. A. Rodgers, J. P. Attfield and A. Fuertes, *J. Am. Chem. Soc.* 2008, 130, 12572.
3. M. Jansen and H. P. Letschert. *Nature* 2000, 404, 980.
4. M. Highashi, R. Abe, T. Takata, K. Domen. *Chem. Mater.* 2009, 21, 1543.
5. K. Maeda, K. Teramura, D. Lu, T. Takata, N. Saito, Y. Inoue and K. Domen, *Nature* 2006, 440, 295.
6. S. J. Clarke, B. P. Guinot, C. W. Michie, M. J. C. Calmont, and M. J. Rosseinsky, *Chem. Mater.* 2002, 14, 288.
7. E. Soignard, D. Machon, P. F. McMillan, J. Dong, B. Xu, K. Leinenweber. *Chem. Mat.* 2005, 17, 5465.
8. J. O. Troyanchuk, N. V. Kasper, O. S. Mantytskaya, E. F. Sbapovalova. *Mater. Res. Bull.* 1995, 30, 421.
9. J. C. Gilles. *Bull. Soc. Chim. Fr.* 1962, 22, 2118.
10. D. Walker, M. A. Carpenter and C. M. Hitch, *Am. Mineral.* 1990, 75, 1020.
11. D. Walker, *Am. Mineral.* 1991, 76, 1092.
12. A. C. Larson and R. B. von Dreele, "General Structure Analysis System (GSAS)", Los Alamos National Laboratory Report LAUR 86-748 (1994)
13. G. M. Veitha, M. Greenblatt, M. Croft, J. B. Goodenough, *Mater. Res. Bull.* 2001, 36, 1521.

Chapter 5. Synthesis, structure and physical properties study of europium molybdenum oxynitrides

5.1 Introduction

Negative colossal magnetoresistances (CMR) have been reported in oxynitride perovskites $EuNbO_2N$ [1] and $EuWO_{1+x}N_{2-x}$ ($-0.16 \leq x \leq 0.46$).[2, 3] These interesting CMR properties are related to the ferromagnetically ordered Eu^{2+} S = 7/2 spins and the mixed oxidation states of the transition metals. As reported in Chapter 3, the physical properties of $EuWO_{1+x}N_{2-x}$ can be tuned by careful synthetic control of the O/N ratios. Molybdenum is another transition metal in the same group as W, which has stable oxidation states of 4+ to 6+. Moreover, oxide precursors with a 1:1 ratio of Eu:Mo have been reported [4] and are good candidates for exploration of new Eu-Mo oxynitride phases and their properties. Numerous oxynitrides with various physical properties have been synthesized and studied, as reviewed in Chapter 1. However, only a few examples of oxynitride pyrochlores have been reported such as $R_2Ta_2O_5N_2$ for R = Nd – Gd,[5] $Sm_2Mo_2O_{3.83}N_{3.17}$ [6] and $Y_2Mo_2O_{4.5}N_{2.5}$.[7]

In this work, $EuMoO_4$ and $Eu_2Mo_2O_7$ have been used as the precursors for thermal ammonolysis at varying conditions. $EuMoO_4$ and $Eu_2Mo_2O_7$ were first synthesized by McCarthy in 1970.[4] $Eu_2Mo_2O_7$ is metallic and shows ferromagnetic interactions below a transition at T_C = 56K.[8, 9] The detailed synthesis, structural characterization and physical properties of the resulting phases are presented here.

5.2 Experimental

5.2.1 Investigation of Eu – Mo oxide precursors

Eu_2O_3 (99.99%, Aldrich) and MoO_3 (99.99%, Aldrich) were pre-heated at 800 ^oC and 350 ^oC for 10 hr, respectively. Mixture of dried Eu_2O_3, MoO_3 and Mo (99.99%, Aldrich) was finely ground and pelletized in the stoichiometric ratio as reaction 5.1.[4]

$$3Eu_2O_3 + Mo + 5MoO_3 \rightarrow 6EuMoO_4 \quad (5.1)$$

The pellet was sealed into a quartz tube under a vacuum of 10^{-2} mbar, and slowly heated to 600 ^oC at 3 ^oC/min for 24 hr, then heat to 1050 ^oC at 3 ^oC/min for 36 hr. After the heating, the sample was cooled to room temperature at 3 ^oC/min. The resulting product was black in colour and stable in air. The purity of $EuMoO_4$ was checked by powder X-ray diffraction and structure refinement.

Eu_2O_3 (99.99%, Aldrich) was pre-heated at 800 ^oC for 10 hr. Mixture of dried Eu_2O_3 and MoO_2 (99.99%, Aldrich) was finely ground and pelletized in the stoichiometric ratio as reaction 5.2.[4]

$$Eu_2O_3 + 2MoO_2 \rightarrow Eu_2Mo_2O_7 \quad (5.2)$$

The pellet was ‘sandwich’ packed between two pieces of Mo foil, and fully covered by Mo powder, then heated in an aluminum boat to 1450 ^oC at 6 ^oC/min. After 24 hr heating under argon, the sample was cooled to room at 6 ^oC/min. The resulting product was black in colour and stable in air. The purity of $Eu_2Mo_2O_7$ was checked by the powder X-ray diffraction and structure refinement.

5.2.2 Thermal ammonolysis

0.2 – 0.3 g of europium molybdenum oxide precursor were placed in an alumina boat, and then sealed into a tube furnace. Nitrogen gas (Oxygen free, BOC) was introduced into the working tube to expel air for 15 min before turning on the ammonia gas (99.999%, BOC) for the reaction. The temperature was raised at the rate of 150 ^{o}C/hr. For $EuMoO_4$, the ammonolysis conditions were explored at the temperature range from 550 – 1000 ^{o}C under an ammonia gas flow rate of 10 – 250 cm^3/min, for 3 – 48 hr. For ammonolysis of $Eu_2Mo_2O_7$, the temperatures were varied as shown in Table 5.1, all for 12 hr under ammonia gas at 250 cm^3/min. After heating, the samples were cooled to room temperature under the same rate of flowing NH_3. The phase purities were checked by powder X-ray diffraction and structure refinement. For physical property measurements, the europium molybdenum oxynitride powders were pelletized and heated at 500 ^{o}C for 3 hr under ammonia gas at 250 cm^3/min.

5.2.3 Sample analysis

The finely ground products were examined by powder X-ray diffraction using a θ-2θ diffractometer with monochromatic $CuK_{\alpha 1}$ radiation (λ = 1.540562 Å). Scans were taken in the 2θ range of 10-120^{o} at a 0.007^{o} step size, and with 3 s count times. The structures were fitted using least square refinement in GSAS.[10]

The proportions of nitrogen and metals in the products were determined for one sample. Nitrogen was measured as N_2 by combustion method using a Carlo Erba CHNS analyzer for all samples. Approximately 3 mg of finely ground samples were used each time. An average result from three analyses was taken for each sample.

5.2.4 Physical property measurements

The electrical resistivity at temperatures from 2 to 300 K was measured using a standard four-probe setup with a Quantum Design Physical Properties Measurement System (PPMS).

The temperature dependence of the magnetic susceptibility was evaluated by using a Quantum Design Magnetic Properties Measurement System (MPMS) under an external field of 100 Gauss from 2 to 300 K after cooling of the sample in the field (FC) and without a field (ZFC). Hystereses were measured under magnetic fields between -7 and +7 T at 5 K.

5.3 Results and discussion

5.3.1 Structure of $Eu_2Mo_2O_7$ and $EuMoO_4$

Figure 5.1 shows the powder X-ray diffraction patterns and Rietveld fits of $Eu_2Mo_2O_7$ and $EuMoO_4$. The $Eu_2Mo_2O_7$ precursor has a pyrochlore structure and crystallized in space group $Fd\bar{3}m$, with cell parameter a = 10.3831(1) Å. The $EuMoO_4$ precursor has a scheelite structure and crystallized in space group $I4_1/a$, with cell parameters a = 5.3875(1) and c = 11.9876(1) Å. These are in good agreement with reported observations.[4]

Figure 5.1 Rietveld refinements against powder X-ray diffractions of (a) $Eu_2Mo_2O_7$ and (b) $EuMoO_4$: χ^2 = 1.183, R_{wp} = 0.0338 and χ^2 = 1.635, R_{wp} = 0.0187 for $Eu_2Mo_2O_7$ and $EuMoO_4$, respectively.

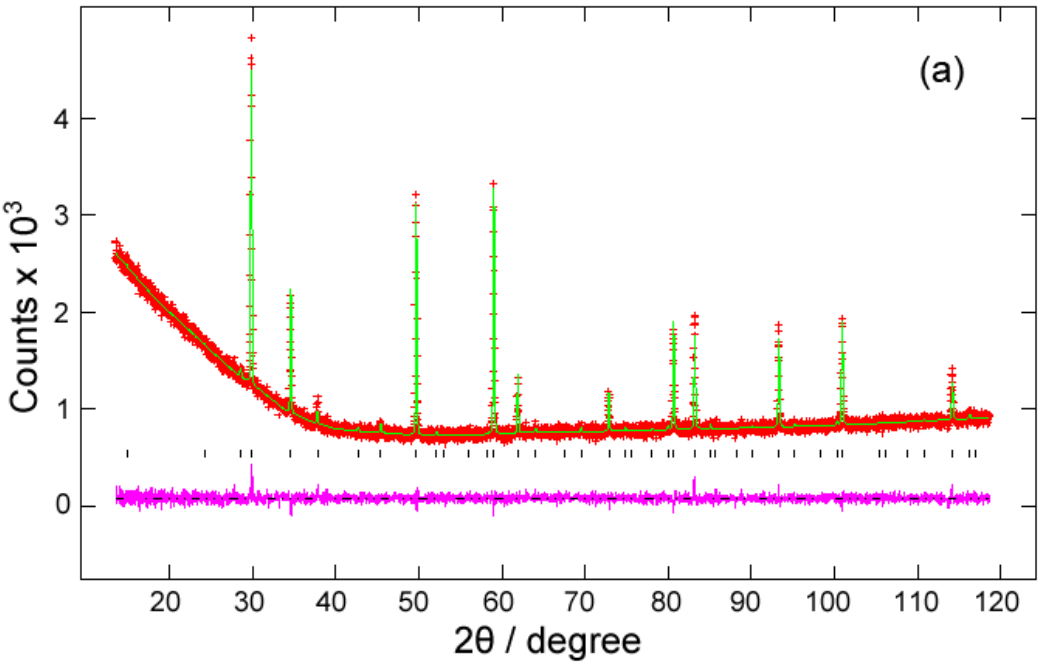

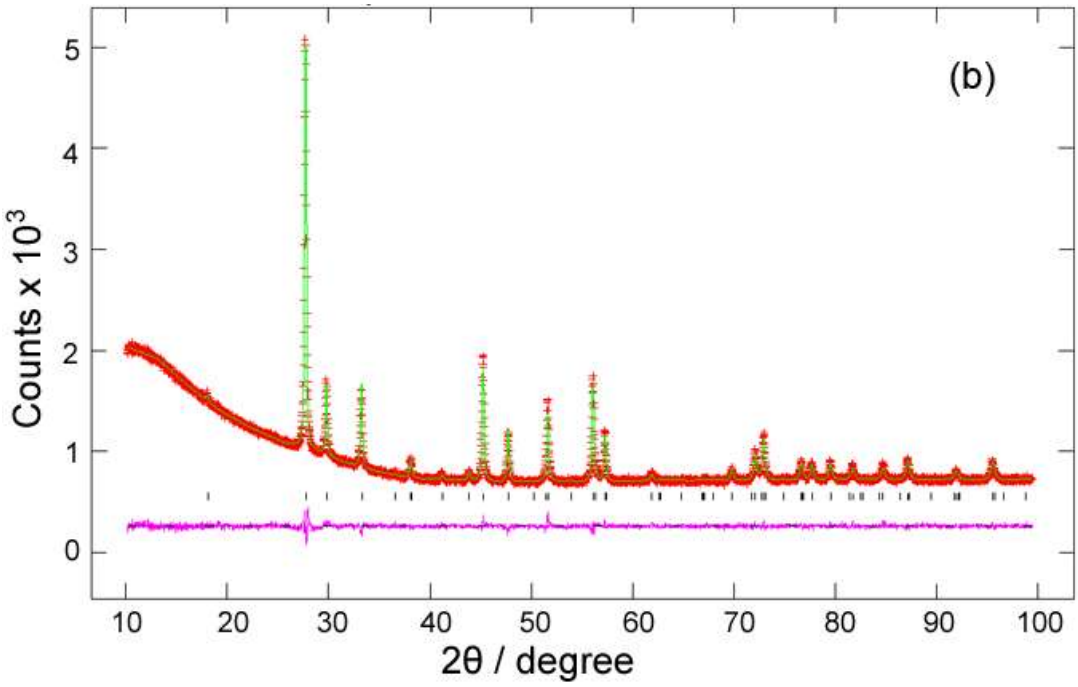

5.3.2 Thermal ammonolysis

There was no evidence of any new europium molybdenum oxynitride phase from the ammonolysis of $EuMoO_4$. The conditions covered temperatures between 550 – 1000 ^oC, reaction times from 3 – 12 hr and flow rates of ammonia gas 10 – 250 cm^3/min. The reactions either gave unreacted products at temperatures below 600 ^oC (although the scheelite phase might incorporate a small amount of nitrogen like the W analogue in Chapter 3) or decomposed products including molybdenum metal at temperatures above 600 ^oC.

The ammonolysis of $Eu_2Mo_2O_7$ at temperatures between 550 ^oC and 630 ^oC for 12 hr under ammonia gas at 250 cm^3/min produced pure phases with the pyrochlore structure in space group $Fd\bar{3}m$, which is evidenced by its characteristic [311] Bragg reflection peak at $2\theta = 37^o$ in the powder X-ray diffraction pattern, as shown in Figure 5.2. The pyrochlore superstructure of the fluorite cell was observed in all samples.

One full chemical analysis was performed on a sample of $Eu_2Mo_2O_7$ after ammonolysis at 550 ^oC for 12 hr. According to the chemical analysis results, it contained 49.3(7)wt% Eu, 31.4(7)wt% Mo, 5.4(0)wt% N and 13.9(10)wt% O, which gives the composition as $Eu_2Mo_{2.02}O_{5.36}N_{2.38}$ showing that the cation stoichiometry is preserved. According to this chemical composition, the total charge of anions in the unit cell can be calculated as -17.9(3), which is within error of -18. This indicates that the two cations are both at their maximum oxidation states, Eu^{3+} and Mo^{6+}. Hence, if fully oxidized the general formula of these oxynitride pyrochlore phases can be written as $Eu_2Mo_2O_{6-x}N_{2+2x/3}$. The compositions of the other products were evaluated from the nitrogen analyses assuming this formula. The isotropic thermal parameter Uiso were constrained to be the same for all atoms in the Rietveld refinements and the background was fitted using a linear interpolation function with

30 terms. The refinement of $Eu_2Mo_2O_{4.53}N_{2.98}$ confirms the cation ordering with 97.1(1.2)% of Eu/Mo at each site. It is not been possible to refine the accurate N/O composition or possible ordering, and neutron data would be needed for further refinement of anion occupancies. Tables 5.1 and 5.2 show the refined atomic positions and selected bond lengths/angles of the 600 ^oC ammonolysis sample. Table 5.3 shows a summary of the lattice parameters a and nitrogen contents x of ammonolysis products synthesized under ammonia gas at 250 cm^3/min for 12 hr at different temperatures. As expected, by varying the reaction temperature with constant ammonia flow rate and reaction time, N content is increased with increasing temperature. The increase in lattice parameter with increasing N content indicates the expanding effect of the substitution of O^{2-} by larger N^{3-}. Figure 5.3 shows a linear relationship of lattice parameter a against the nitrogen content x based on the chemical formula $Eu_2Mo_2O_{6-x}N_{2+2x/3}$.

Figure 5.2 (a) Powder X-ray diffraction patterns for $Eu_2Mo_2O_7$ and the pyrochlore type $Eu_2Mo_2O_{6-x}N_{2+2x/3}$ phases shown in Table 5.1. (b) Rietveld fit to the powder X-ray diffraction pattern of $Eu_2Mo_2O_{4.53}N_{2.98}$, showing the difference between the experimental and calculated points and the Bragg reflection markers.

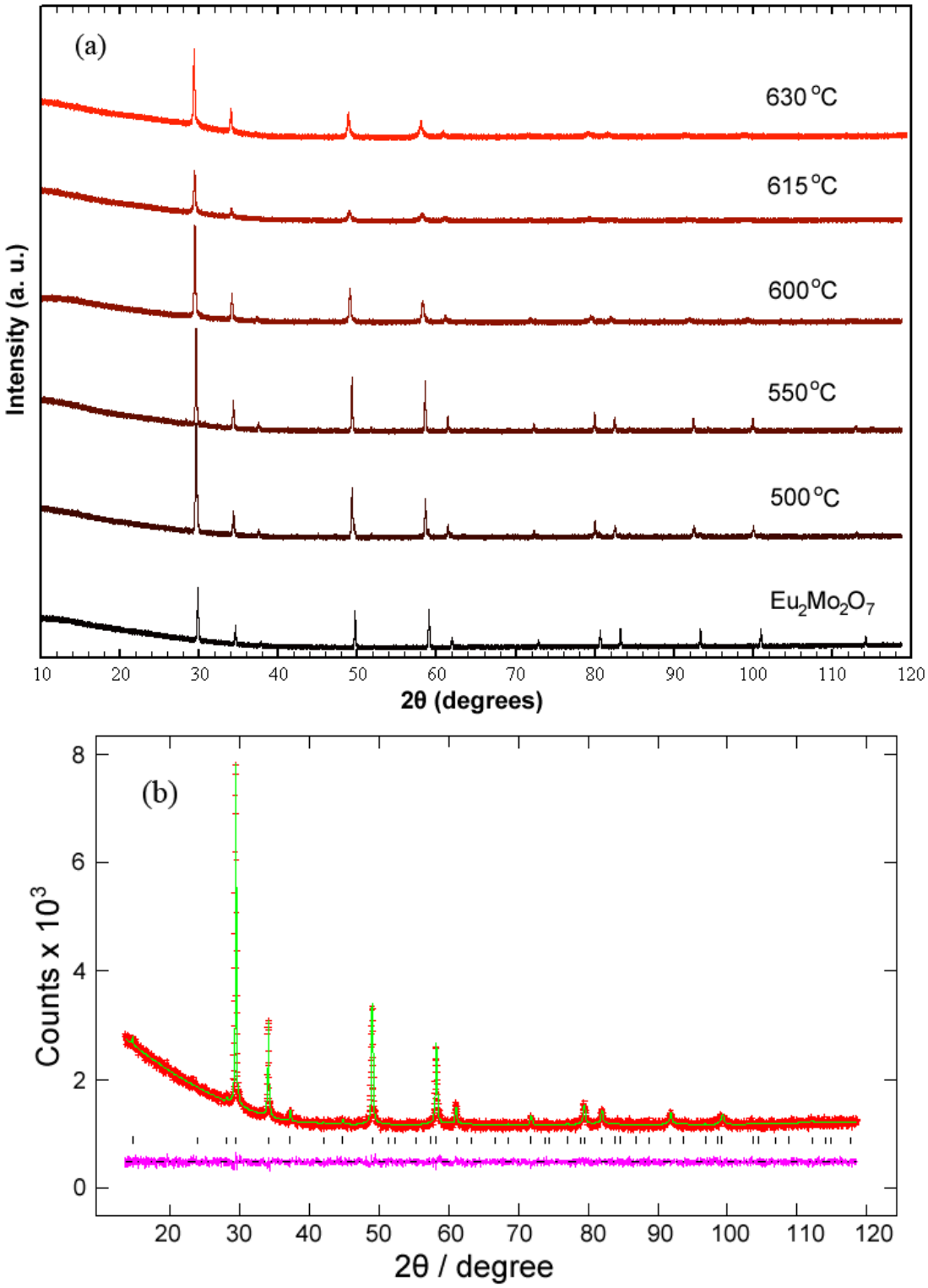

Table 5.1 Ammonolysis temperatures, analyzed N contents and phase results of $Eu_2Mo_2O_{6-x}N_{2+2x/3}$ ($0.20 \leq x \leq 2.25$).

T / °C	Average N%	x	a / Å	O:N	Comments
630	8.10	2.25	10.5386(4)	3.75:3.50	Pyrochlore
615	7.17	1.67	10.5070(2)	4.33:3.11	Pyrochlore
600	6.84	1.47	10.4979(2)	4.53:2.98	Pyrochlore
550	5.40	0.56	10.4532(1)	5.44:2.37	Pyrochlore
*500	3.91	0.20	10.4479(2)	5.80:2.13	80(1)% oxynitride
		-	10.3859(1)		20(1)% oxide
$Eu_2Mo_2O_7$	0	-	10.3832(1)		Pyrochlore

* sample is a mixture of oxynitride and oxide pyrochlore phases.

Table 5.2 Atomic coordinates for $Eu_2Mo_2O_{6-x}N_{2+2x/3}$ synthesized at 600 ℃, in space group $Fd\bar{3}m$, from refinement against powder X-ray diffraction data.

Atom	x	y	z	O/N Occup.	Uiso ×100 (Å^2)
Eu	0.5	0.5	0.5	1	2.13(4)
Mo	0	0	0	1	2.13(4)
O/N(1)	0.3404(9)	0.125	0.125	0.6/0.4	2.13(4)
O/N(2)	0.375	0.375	0.375	0.6/0.4	2.13(4)
O/N(3)	0.875	0.375	0.375	0.3/0.2	2.13(4)

$R_{wp} = 0.0281$, $R_p = 0.0222$, $\chi^2 = 1.089$

Table 5.3 Selected bond distance and angles for $Eu_2Mo_2O_7$ and $Eu_2Mo_2O_{6-x}N_{2+2x/3}$ synthesized at 600 ℃, in space group $Fd\bar{3}m$, from refinement of powder X-ray diffraction data.

	$Eu_2Mo_2O_7$		$Eu_2Mo_2O_{4.53}N_{2.98}$	
Dis. (Å)	Eu_O1 (×6)	2.526(9)	Eu_O/N1 (×6)	2.580(7)
	Eu_O2 (×2)	2.24709(1)	Eu_O/N2 (×2)	2.27287(4)
	<Eu-O>	2.456(5)	<Eu-O/N>	2.503(5)
	Mo_O1 (×6)	2.026(6)	Mo_O/N1 (×6)	2.034(4)
Ang. (deg)	Eu_O1_Eu	93.2(4)	Eu_O/N1_Eu	92.00(34)
	Eu_O2_Eu	109.471(1)	Eu_O/N2_Eu	109.471(2)
	Mo_O1_Mo	129.8(7)	Mo_O/N1_Mo	131.7(6)

Figure 5.3 Plot of cubic lattice parameter a against x for $Eu_2Mo_2O_{6-x}N_{2+2x/3}$ (red triangle) and $Eu_2Mo_2O_7$ (black circle) taken as x = -1 for comparison with the latter phases. The sample ammonolysed at 500 °C which is a mixture of phases as shown in Table 5.1, is shown as the oxide (black square) and oxynitride (red square) components. The $Eu_2Mo_2O_{6-x}N_{2+2x/3}$ materials have x/3 anion vacancies per formula unit. The errors in a and x are much smaller than the points.

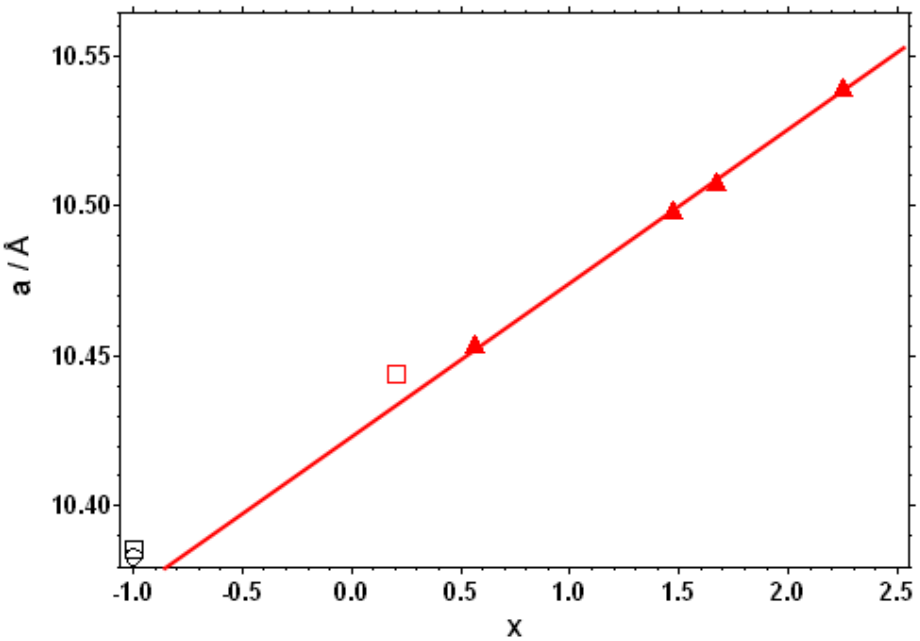

No intermediate between the Mo^{4+} parent oxide and the Mo^{6+} oxynitride pyrochlore is observed. Figure 5.4 shows the Rietveld refinement of the powder x-ray pattern at high 2θ angles of $Eu_2Mo_2O_7$ ammonolysed at 500 ^oC for 12 hr, which is fitted well with a mixture of 80(1)% : 20(1)% of oxynitride and oxide.

Figure 5.4 Rietveld fit to the powder X-ray diffraction pattern of the 500 ^oC for 12 hr ammonolysis sample $Eu_2Mo_2O_{5.80}N_{2.13}$. Oxynitride and oxide pyrochlore phases are represented by the black and red vertical bars, respectively.

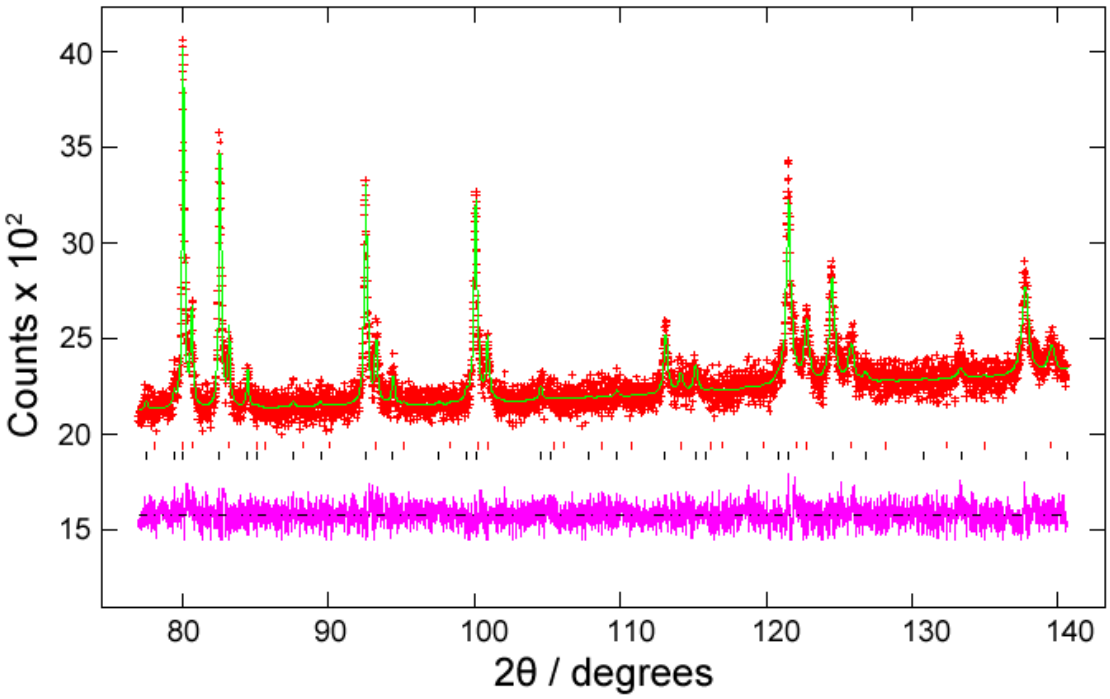

5.3.3 Ammonolysis process

According to the bond lengths in Table 5.2, the average <Eu-O/N> distance in $Eu_2Mo_2O_{4.53}N_{2.98}$ is 2.503(5) Å, compared to 2.456(5) Å for the <Eu-O> distance in the parent oxide. Compared to the relatively large difference between the ionic radii of Eu^{2+} (1.17 Å) and Eu^{3+} (0.947 Å), the small change in bond length suggests the Eu^{3+} is not reduced during ammonolysis. The ionic radii of Mo^{4+} and Mo^{6+} are 0.65 Å and 0.59 Å, respectively, which leads to a very small difference in bond length.

Hence, there is no significant structural indication of the changing oxidation states. However, the chemical analysis result suggests a reasonable chemical formula as discussed above, where the oxidation state of Mo ion is 6+. Therefore, the redox process in the initial ammonolysis reaction can be written as:

$$Mo^{4+} + \frac{1}{2}O^{2-} + NH_3 \rightarrow N^{3-} + \frac{1}{2}H_2O + H_2 + Mo \qquad (5.3)$$

According to the powder X-ray diffraction (Figure 5.4), the reaction occurs through a discontinuous pyrochlore to pyrochlore transformation. Ammonia can act as a simultaneous reducing and nitriding agent, or can bring about only one of these changes. In this case, the preservation of the cation ordering indicates that the ammonolysis of $Eu_2Mo_2O_7$ starts by filling the vacancies in the pyrochlore structure with N^{3-}, which gives a total number of eight anions without changing the structure. This process combined with some substitution of O^{2-} by N^{3-} and accompanied by the above redox reaction to give Mo^{6+} is fast. After this, there is further slow substitution of O^{2-} by N^{3-}. The whole process can be represented as:

$$Eu_2^{3+}Mo_2^{4+}O_7^{2-} \xrightarrow[\text{Fill vacancies and fast substitution}]{\text{Fast}} Eu_2^{3+}Mo_2^{6+}O_6^{2-}N_2^{3-} \xrightarrow[\text{Further substitution}]{\text{Slow}} Eu_2^{3+}Mo_2^{6+}O_{6-x}^{2-}N_{2+2x/3}^{3-}$$

5.3.4 Magnetization

The AC magnetic susceptibility of the parent oxide $Eu_2Mo_2O_7$ is shown in Figure 5.5. It shows a typical paramagnetic - ferromagnetic transition. A Curie temperature T_C ~ 52 K was estimated by extrapolating the maximum slope ($-d\chi/dT$) to zero magnetization. The Curie-Weiss fit of inverse susceptibility of the paramagnetic region gives a positive Weiss temperature θ = 75 K, which also indicates a typical ferromagnetic character. All these results are in good agreement with reported

observations.[9]

Figure 5.5 Temperature dependences of the ac magnetic susceptibility of $Eu_2Mo_2O_7$ (red points - zero field cooled (ZFC) and blue points - field cooled (FC)) under an external magnetic field of 100 Gauss, inverse (inset) of ZFC susceptibility with a Curie – Weiss fit to the paramagnetic region.

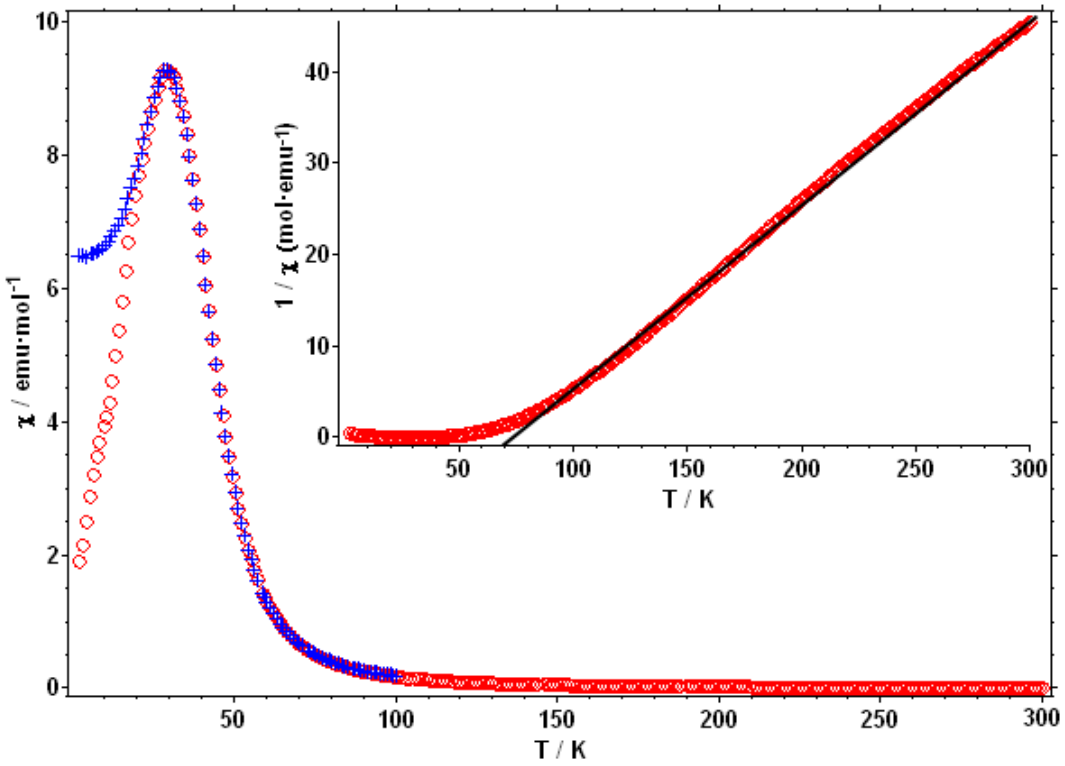

The AC magnetic susceptibilities for $Eu_2Mo_2O_{6-x}N_{2+2x/3}$ (x = 0.20, 0.56 and 1.67) are shown in Figure 5.6. The 20(1)% $Eu_2Mo_2O_7$ contributes strongly in the x = 0.20 sample, thus it shows similar curvature with a lower moment to the parent oxide with a ferromagnetic transition at $T_C \approx 52$ K. The magnetization of the x = 0.56 sample shows different curvature to the x = 0.20 sample. There are two magnetic transitions at ~ 52 K and 8 K, indicating a small magnetization contribution from $Eu_2Mo_2O_7$, although this is not observed in the powder X-ray diffraction pattern in Figure 5.2(a). For the x = 1.67 sample, the temperature dependences of zero field cooled and field cooled magnetizations are identical. A Curie-Weiss fit to the paramagnetic region (80

≤ T ≤ 300 K) yields a negative Weiss constant θ, suggesting antiferromagnetic interactions. For the x = 0.20 and 0.56 samples, Curie-Weiss fits to the paramagnetic region were made between 200 and 300 K due to the oxide impurity, both also yield a negative Weiss constant θ. For the pure oxynitride sample x = 1.67, the magnetization increases at low temperatures which indicates a ferrimagnetic ordering. The effective moments μ_{eff}, were calculated from the Curie constants C of the Curie-Weiss fits. The summary of the susceptibility measurements for $Eu_2Mo_2O_{6-x}N_{2+2x/3}$ (x = 0.20, 0.56 and 1.67) is shown in Table 5.4. The μ_{eff} values for all the samples are higher than for combinations of Eu^{3+} and Mo^{6+}, which suggests that the samples contain unoxidized Mo^{4+} d^2 or minor Eu^{2+} impurities.

Figure 5.6 Temperature dependences of the AC magnetic susceptibility of the $Eu_2Mo_2O_{6-x}N_{2+2x/3}$ (x = 0.20, 0.56 and 1.67): red points - zero field cooled (ZFC) and blue points - field cooled (FC) under an external magnetic field of 100 Gauss, inverse (inset) of ZFC susceptibility with the Curie – Weiss fit to the paramagnetic region.

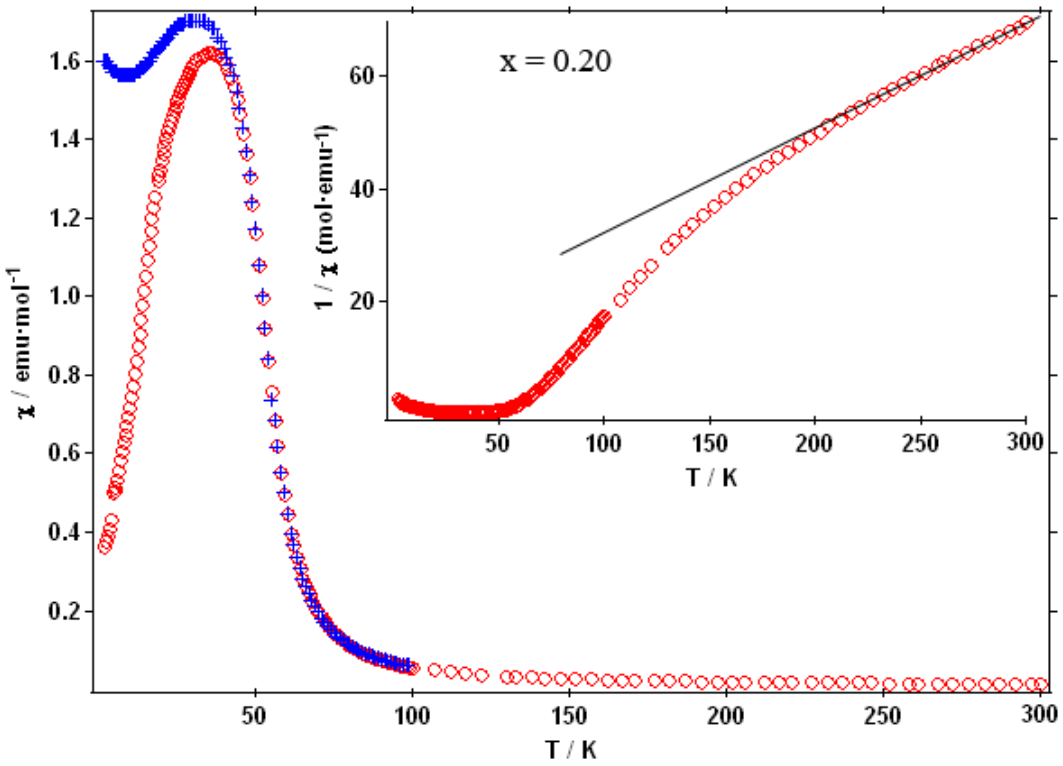

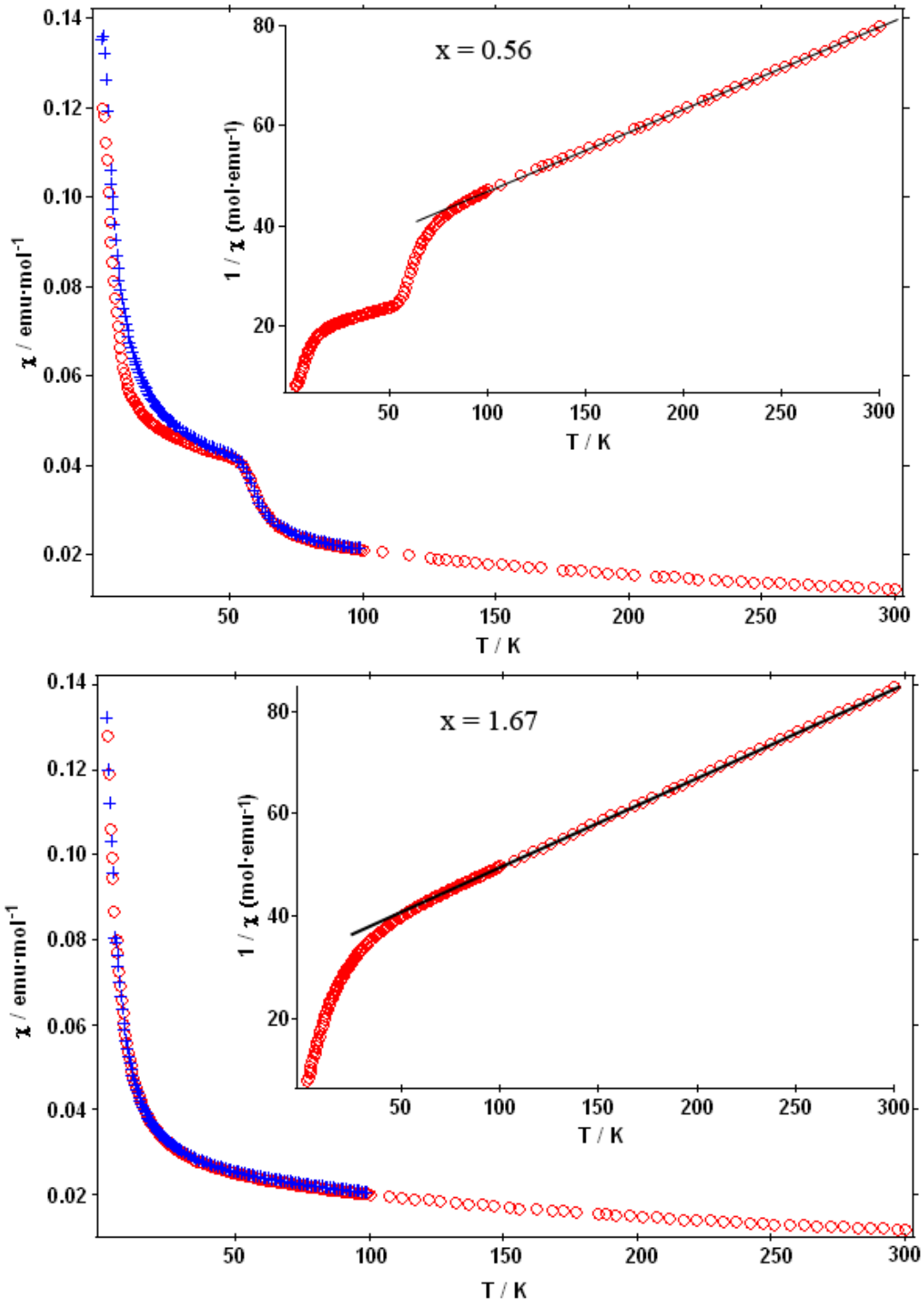

Magnetization-field loops of all three samples in Figure 5.7 show typical behaviour for a soft ferromagnet at low temperature with an additional paramagnetic background. The magnetization increases slowly and approximately linearly with

applied field after 3 T, which suggests saturation has been reached. Due to the large magnetization of the oxide impurity (S = 1 for d^2 Mo^{4+}), the μ_{sat} of the phase mixture is much higher than for the pure oxynitride phases as summarized in Table 5.4.

Figure 5.7 Magnetization curves of $Eu_2Mo_2O_{6-x}N_{2+2x/3}$ (x = 0.20, 0.56 and 1.67) at 5 K between -7 and 7 T.

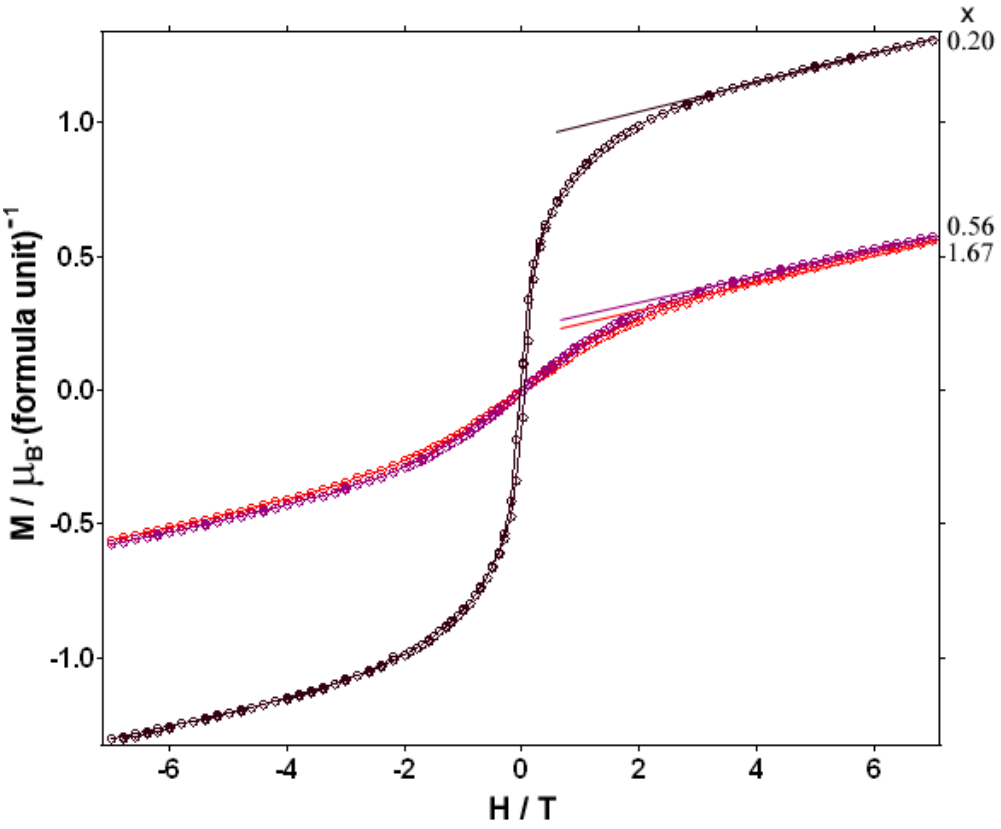

5.3.5 Conductivity

The temperature variations of the electronic resistivity of $Eu_2Mo_2O_{6-x}N_{2+2x/3}$ (x = 0.20, 0.56 and 1.67) are shown in Figure 5.8. It shows typical semiconducting behavior for all three samples as an increase in resistivity with x is observed. The summary of band gap energy E_g of the intrinsic region is shown in Table 5.4. E_g was calculated from the plot of log(resistivity) against 1/T ($55 \leq x \leq 70$) using the following equation:

$$\rho(T) = \rho_0 \cdot \exp\left(\frac{E_g}{2k_B T}\right) \qquad (5.4)$$

Figure 5.8 Temperature dependence of the electric resistivity of $Eu_2Mo_2O_{6-x}N_{2+2x/3}$ (x = 0.20, 0.56 and 1.67). The sample with x = 0.20 is a mixture of oxide and oxynitride.

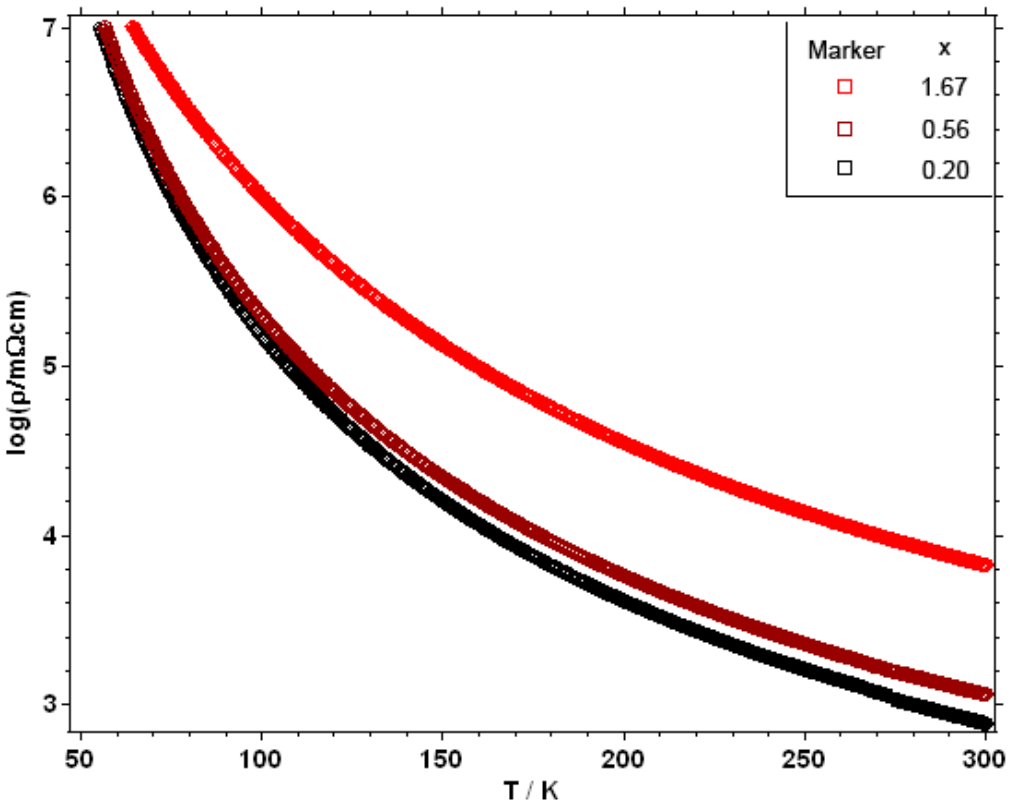

Figure 5.9 shows a good linear fit according to the 3-dimensional variable range hopping (VRH) model:

$$\rho(T) = \rho_0 \cdot \exp\left(\frac{T_0}{T}\right)^{1/4} \qquad (5.5)$$

where T_0 is related to inverse localization length α, based on:

$$k T_0 = 18\alpha^3 / 3N(E_F) \qquad (5.6)$$

where $N(E_F)$ is the density of states at the Fermi energy. This confirms that the $Eu_2Mo_2O_{6-x}N_{2+2x/3}$ samples are disordered semiconductors.

Figure 5.9 Plot of the electrical resistivity measurements against $T^{-1/4}$ of $Eu_2Mo_2O_{6-x}N_{2+2x/3}$ (x = 0.20, 0.56 and 1.67). The sample with x = 0.20 is a mixture of oxide and oxynitride.

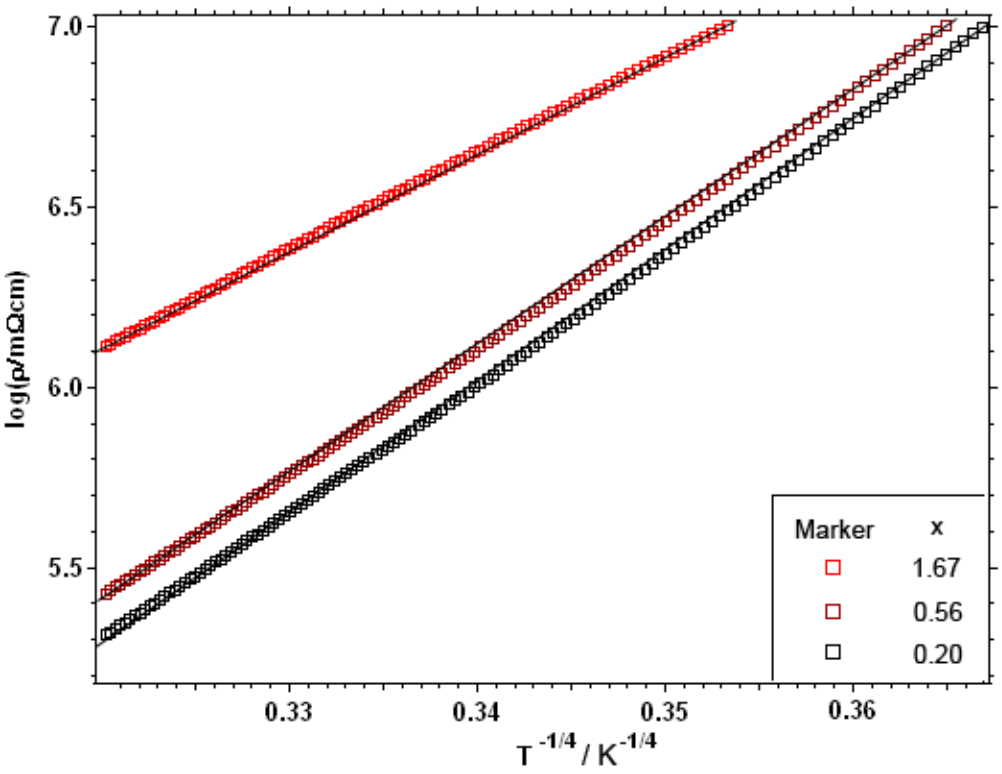

Table 5.4 Results of magnetization and electronic resistivity measurements for $Eu_2Mo_2O_{6-x}N_{2+2x/3}$ (x = 0.20, 0.56 and 1.67)

x	*0.20	0.56	1.67
C (emu·K/mol)	4.74	6.18	5.70
μ_{eff} (μ_B) / mol	6.17	7.04	6.77
θ / K	-34	-191	-183
μ_{sat} (μ_B)	0.96	0.22	0.20
T_c / K	-	7.5	8
ρ / mΩcm at 300K	0.008	0.011	0.067
E_g / eV	0.082	0.081	0.061
ρ_0 / mΩcm	3.09×10^{-3}	1.44×10^{-6}	5.76×10^{-7}
T_0 / K	2.79×10^{7}	2.57×10^{7}	1.87×10^{7}

* sample is a mixture of 20(1)% oxide and 80(1)% oxynitride.

5.4 Conclusions

A new series of oxynitrides $Eu_2Mo_2O_{6-x}N_{2+2x/3}$ ($0.20 \leq x \leq 2.25$) has been synthesized using thermal ammonolysis of $Eu_2Mo_2O_7$ in the temperature range of 500 to 630 ^oC for 12 hr. Powder X-ray diffraction shows the polycrystalline samples crystallize in the pyrochlore structure with the space group $Fd\bar{3}m$. Both Eu and Mo cations are at their maximum oxidation states of 3+ and 6+, respectively. The cubic lattice parameter increases linearly with x. $Sm_2Mo_2O_{3.83}N_{3.17}$ is the only previously reported molybdenum oxynitride pyrochlore, synthesized by ammonolysis of $Sm_2Mo_2O_7$.[6] The oxidation state of Mo was reported as an average of 5.6+. This does not agree with the conclusions of this work. Pyrochlore structures have relatively high flexibility in chemical composition, where y normally varies from 6 to 7 in the general formula $A_2B_2X_y$. However, with mixed anions and vacancies in the

Eu-Mo-O-N phases, up to 8 anions per formula unit can be obtained, as discovered by the chemical analysis on both metals and nitrogen for one sample, where a total of more than 7 anions was observed. However in the report of $Sm_2Mo_2O_{3.83}N_{3.17}$, only nitrogen was analyzed based on the assumption of a total 7 anions.[6]

Typical semiconductor behaviours have been observed in all the samples, with E_g = 61 meV for $Eu_2Mo_2O_{4.33}N_{3.11}$. A good linear fit according to the 3-dimensional variable range hopping (VRH) model suggests disordered semiconductor properties. All the samples show ferrimagnetic ordering below a Curie temperature $T_C = 8 \pm 1$ K. These physical properties are very similar to those reported for $Sm_2Mo_2O_{3.83}N_{3.17}$.[6]

5.5 References

1. A. B. Jorge, J. Oró-Solé, A. M. Bea, N. Mufti, T. T. M. Palstra, J. A. Rodgers, J. P. Attfield and A. Fuertes, *J. Am. Chem. Soc.* 2008, 130, 12572.
2. Minghui Yang, J. Oró-Solé, A. Kusmartsva, A. Fuertes and J. Paul. Attfield, *J. Am. Chem. Soc.* 2010, 132, 4822.
3. A. Kusmartsva, Minghui Yang, J. Oró-Solé, A. B. Jorge, A. Fuertes and J. Paul. Attfield, *Appl. Phys. Lett.* 2009, 95, 022110.
4. G. J. McCarthy. *Mater. Res. Bull.* 1971, 6, 31.
5. P. Maillard, F. Tessier, E. Orhan, F. Chevirél, and R. Marchand, *Chem. Mater.*, 2005, 17, 152.
6. G. M. Veith, M. Greenblatt, M. Croft and J. B. Goodenough, *Mater. Res. Bull.* 2001, 36, 7, 1521.
7. M. J. Martinez-Lope, M. T. Casais, J. A. Alonso, *Z. Naturforsch.* 2006, 61B, 164.
8. I. Kézsmárki, N. Hanasaki, K. Watanabe, S. Iguchi, Y. Taguchi, S. Miyasaka and Y. Tokura, *Phys. Rev. B* 2006, 73, 125122.
9. N. Hanasaki, K. Watanabe, T. Ohtsuka, I. Kézsmárki, S. Iguchi, S. Miyasaka, and Y. Tokura, *Phys. Rev. Lett.* 2007, 99, 086401.
10. A. C. Larson and R. B. von Dreele, "General Structure Analysis System (GSAS)", Los Alamos National Laboratory Report LAUR 86-748 (1994)

Chapter 6. Neutron diffraction study of $SrTaO_2N$ and $SrNbO_2N$

6.1 Introduction

Cation order-disorder phenomena in perovskites and other extended inorganic structures have been studied extensively, but anion orders are less well studied, in particular for isoelectronic species such as oxide and nitride. The properties of ABO_3 oxide perovskites are sensitive to small structural distortions that may arise from the tilting or Jahn-Teller distortions (orbital order) of the BO_6 octahedra. Anion order in oxynitride perovskites is expected to have a strong influence on physical properties, especially when these are sensitive to local distortions, for example in directing the cation displacements in dielectric materials, but consistent models for anion order have not been reported even for representative materials such as $SrMO_2N$ (M = Nb, Ta) where the anion content is close to the ideal stoichiometry.[1-4] In this work, anion order in $SrMO_2N$ (M = Nb, Ta) was studied by using variable temperature neutron diffraction and electron diffraction.

6.2 Experimental

6.2.1 Synthesis of $SrMO_2N$ (M = Nb, Ta)

The samples were prepared by Dr. Judith Oró-Solé at ICMAB Barcelona. Polycrystalline 2 g samples of $SrMO_2N$ (M = Nb, Ta) were prepared by reaction of stoichiometric amounts of $SrCO_3$ (Baker, 99.9 %) and Nb_2O_5 (Aldrich, 99.99 %) or Ta_2O_5 (Aldrich, 99.99 %) at 1000 ^oC in ammonia gas (Carburos Metálicos, 99.9 %)

for several cycles of 40-50 hr, with pelletizing and intermediate regrinding. The ammonia flow rate was 180 cm^3/min.

6.2.2 Neutron powder diffraction

Neutron powder diffraction data were collected using the Super-D2B diffractometer at the Institut Laue Langevin (ILL, Grenoble, France). Neutrons of wavelength 1.5943 Å were incident on an 8 mm vanadium can contained in a furnace. Patterns were collected at temperatures 25-750 ℃ in the angular range $5 \leq 2\theta \leq 160°$ with steps of 0.05 º and an overall collection times of 3 hr. The crystal structures were analysed by the Rietveld method[20] using the GSAS software package.[5]

6.2.3 Electron diffraction

Electron diffraction patterns from individual microcrystallites of $SrMO_2N$ (M = Nb, Ta) were obtained by Dr. Judith Oró-Solé using a JEOL 1210 transmission electron microscope operating at 120 kV equipped with a side-entry 60/30 ° double tilt GATHAN 646 specimen holder. The samples were prepared by dispersing the powders in ethanol and depositing of a droplet of this suspension on a carbon coated holey film supported on a copper grid. The sample stage was rotated about the c-axis of the pseudo-tetragonal (I4/mcm) superstructure in order to observe the diffraction intensities in the (100) and (010) planes.

6.3 Results

The cubic AMX_3 perovskite structure consists of a network of corner-linked MX_6 octahedra and ideally has cubic $Pm\bar{3}m$ symmetry, but this may be lowered through internal perturbations (including anion order) or rotations and tilting of the octahedra. This often leads to structural phase transitions, as seen for $SrMO_2N$ (M = Nb, Ta) in Figure 6.1 where additional superstructure diffraction peaks arising from ordered rotations of the octahedral are observed at room temperature, but only the peaks expected from a cubic perovskite are observed above 300 ℃ for $SrNbO_2N$ and above 200 ℃ for $SrTaO_2N$.

Figure 6.1 Summary of experimental D2B powder neutron diffraction patterns for $SrNbO_2N$ and $SrTaO_2N$.

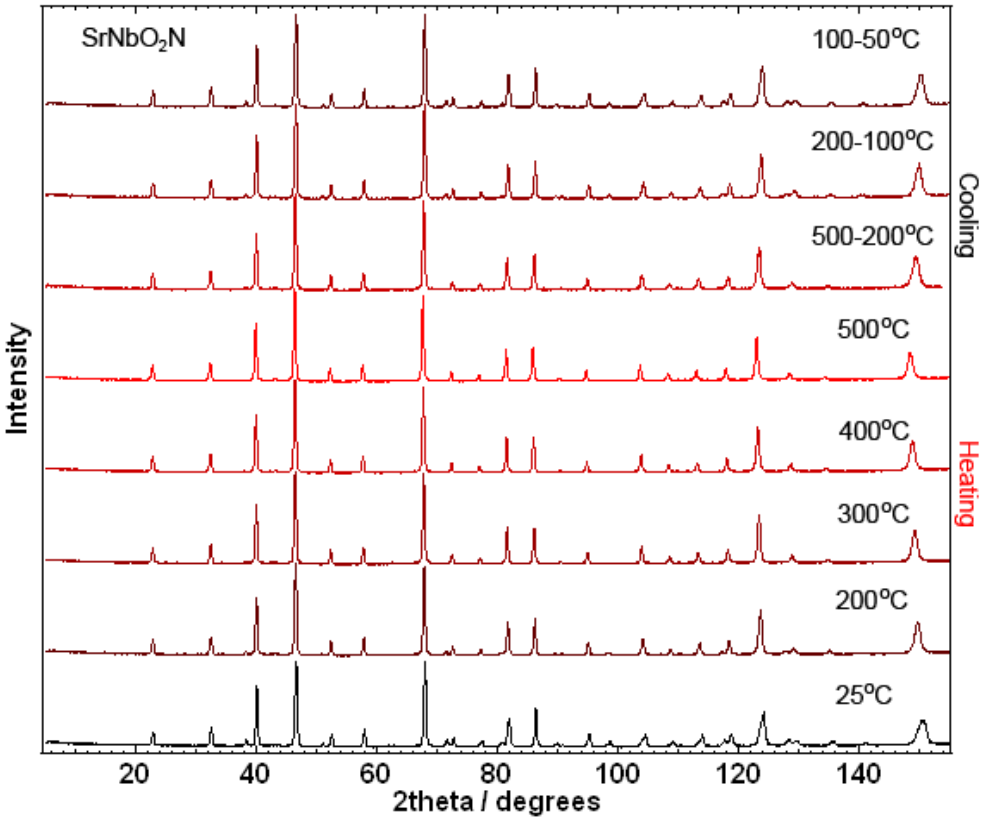

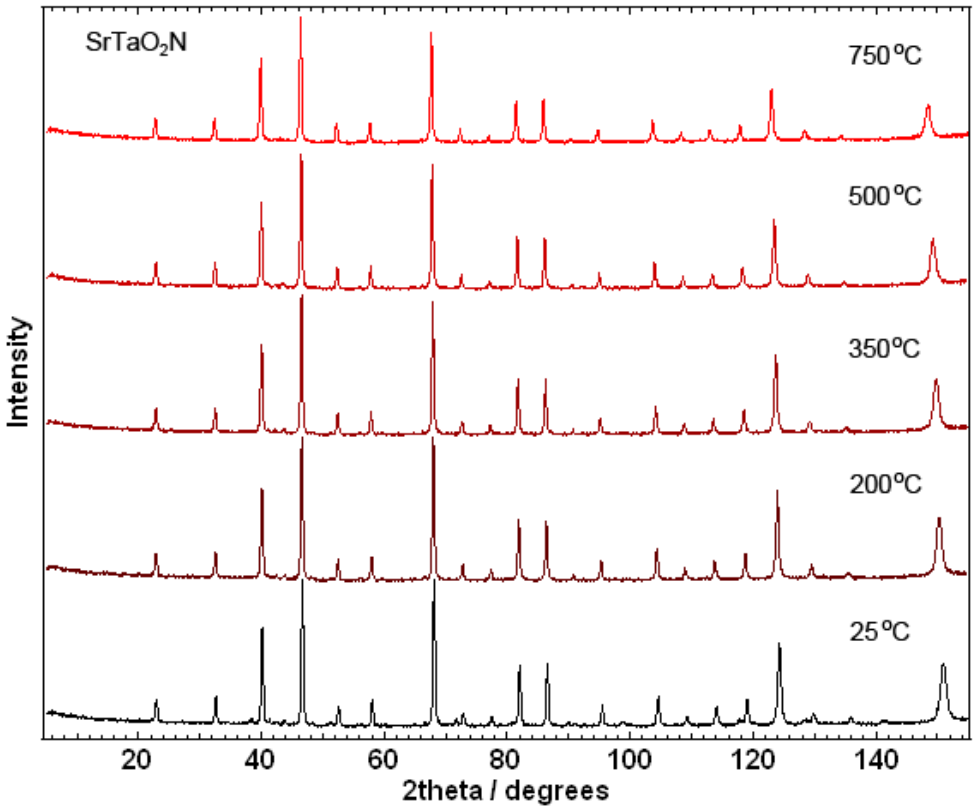

Neutron diffraction is sensitive to small anion displacements as the scattering lengths of the light and heavy atoms are comparable (b_{Sr} = 0.702, b_{Nb} = 0.705, b_{Ta} = 0.691, b_O = 0.581, b_N = 0.936 fm) and also offers high O/N scattering contrast. However, the sensitivity of powder neutron data to anion order within the perovskite arrangement strongly depends on the magnitude of the accompanying lattice distortion that broadens or splits the diffraction peaks. If the cell distortion is small then O/N ordered and disordered models give very similar net diffraction peak intensities, as confirmed by simulated patterns shown in Figure 6.2. Hence, although the high temperature $SrMO_2N$ neutron data are fitted satisfactorily by a statistically disordered cubic perovskite model in which all anion sites are equivalent, we also tested a tetragonal P4/mmm symmetry model to investigate possible long range anion order.

Figure 6.2 Simulated D2B powder neutron diffraction patterns for $SrNbO_2N$ showing the effects of different anion ordering models and tetragonal distortions in the P4/mmm model. (a) where a resolvable tetragonal distortion (c/a = 0.99) is used. (b) shows the situation when there is no distortion (c/a = 1); the intensities from the three models are virtually identical although they are not mathematically equivalent.

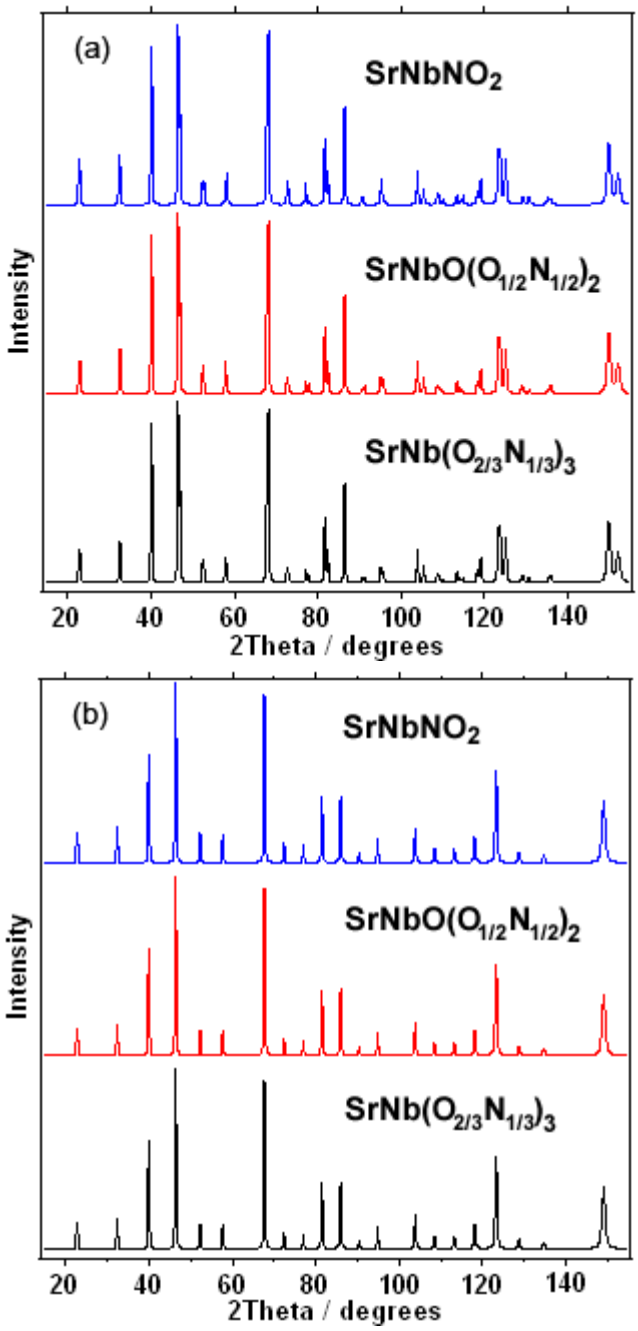

Refinements of the P4/mmm model, which allows for possible 1:2 anion order over inequivalent X1 and X2 sites, gave a striking result. For both $SrNbO_2N$ and $SrTaO_2N$, the fits converged to an ordered model with the X1 site fully occupied by O, and the X2 sites occupied by a near 50:50 O/N mixture as shown in Table 6.1. For $SrNbO_2N$ the refined anion composition of $SrNbO_{2.07}N_{0.93}$ is consistent with the chemical analysis and previous studies of this phase [1, 4] and this composition was used in the fits to the other diffraction profiles. $SrTaO_2N$ was found to be stoichiometric by analysis and neutron refinement. The slight decrease of the tetragonal c-dimension relative to a is consistent with the anion order, as oxide is slightly smaller than nitride, but the effect is too small to result in visible peak broadenings and the anion segregation in the refinement is driven by the slight difference in intensities of the composite powder diffraction peaks, as illustrated by an improvement from 5.22% to 4.96% in R_{F^2} (structure factor-squared residual) for the odd h+k+l reflections which are sensitive to the anion distribution. Figure 6.3 shows the Rietveld fits to the powder neutron diffraction patterns in pseudo-cubic (tetragonal P4/mmm) model at 300 ℃ and 200 ℃ of $SrMO_2N$ (M = Nb, Ta), respectively. Figure 6.4 shows the anion labels in the refinement models, which are X sites in the high temperature and Y sites in room temperature model (see later), respectively.

Figure 6.3 Rietveld fits to the powder neutron diffraction patterns of $SrMO_2N$ (M = Nb, Ta), with observed points as crosses, calculated profiles as full lines and the difference and reflection markers offset below.

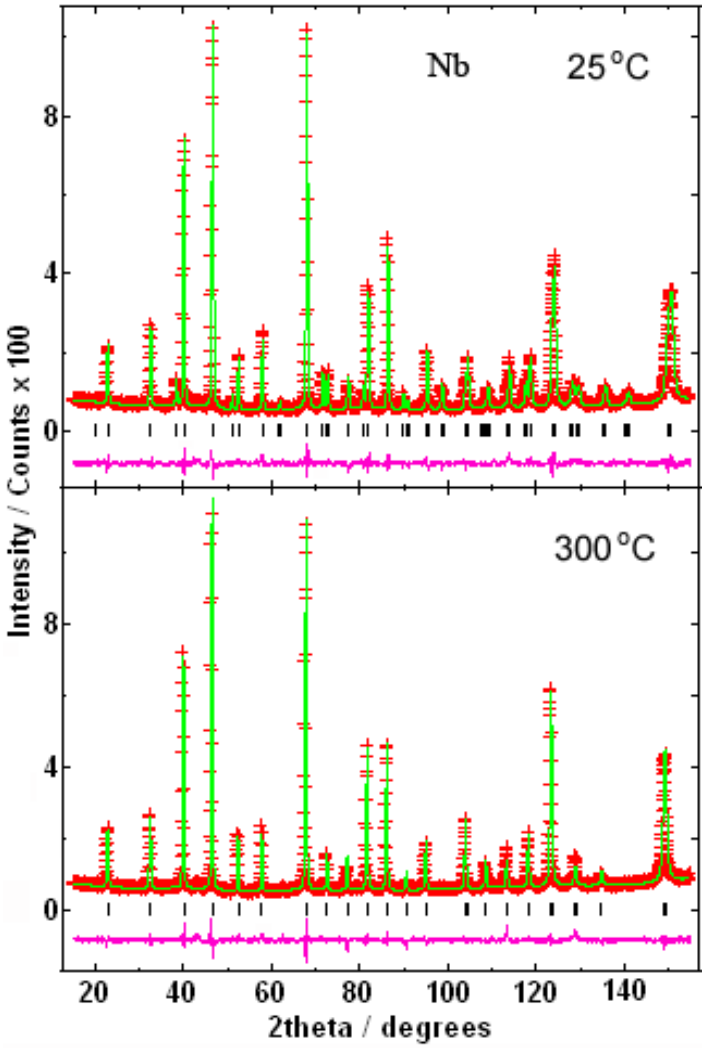

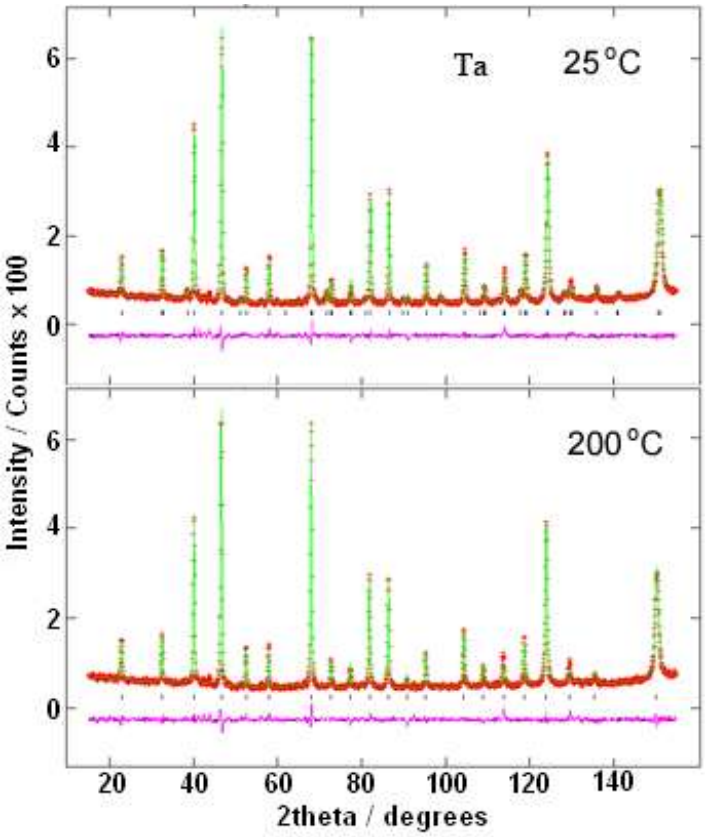

Figure 6.4 Structural model for the $SrMO_2N$ perovskites, showing the relationship between the unique axes for anion order ($\mathbf{c}_{an}$) and octahedral rotation ($\mathbf{c}_{rot}$) in the room temperature phase. The correspondence between the X1 (oxide, unshaded atoms) and X2 (50:50 O:N, half-shaded) sites produced by anion order, and the inequivalent Y1 and Y2 sites created by rotational order is shown.

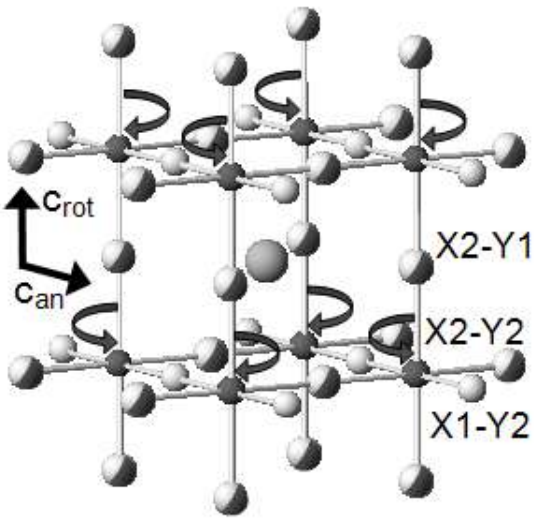

Table 6.1 Refined atomic model and selected bond distance and angles for the pseudo-cubic phases of $SrNbO_2N$ at 300 ℃ and (where different given underneath in italics) of $SrTaO_2N$ at 200 ℃, in tetragonal space group P4/mmm.

Atom	x	y	z	U_{iso} (Å^2)	O/N occupancy
Sr	0.5	0.5	0.5	0.0170(5) *0.0130(5)*	
Nb *Ta*	0	0	0	0.0082(4) *0.0052(4)*	
X1	0	0	0.5	0.0225(4) *0.0187(3)*	0.99(4)/0.01 *0.96(4)/0.04*
X2	0.5	0	0	0.0225 *0.0187*	0.54(3)/0.46 *0.51(3)/0.49*

$SrNbO_2N$: a = b = 4.0541(2)Å, c = 4.0511(4)Å, χ^2 = 4.12, R_{wp} = 5.61%, R_{F^2} = 3.30%;

$SrTaO_2N$: a=b= 4.0442(3)Å, c= 4.0421(5)Å, χ^2 = 2.81, R_{wp} = 5.25%, R_{F^2} = 3.62%

	$SrNbO_2N$		$SrTaO_2N$	
Dis. (Å)	Sr_O/N1(X2)×8	2.86563(15)	Sr_O/N1(X2)×8	2.85893(21)
	Sr_O/N2(X1)×4	2.86669(14)	Sr_O/N2(X1)×4	2.85966(19)
	<Sr_O/N>12	2.86598(15)	<Sr_O/N>12	2.85917(20)
	Nb_O/N1(X2)×4	2.02706(10)	Ta_O/N1(X2)×4	2.02208(13)
	Nb_O/N2(X1)×2	2.02555(19)	Ta_O/N2(X1)×2	2.02105(26)
	<Nb_O/N>6	2.02655(15)	<Ta_O/N>6	2.02173(15)
Ang. (deg)	Sr_O/N1(X2)_Sr	89.957(6)	Sr_O/N1(X2)_Sr	89.971(8)
	Sr_O/N1(X2)_Sr	90.042(6)	Sr_O/N1(X2)_Sr	90.029(8)

The refinement results are summarized in Table 6.2. Figure 6.5 shows the plot of the oxygen occupancies of the X1 site in pseudo-cubic model at high temperatures. The oxygen occupancies of the X1 site decrease slightly with increasing temperature but remains at ~90% up to 750 °C in $SrTaO_2N$, which approaches synthesis conditions (≥

Table 6.2 Results from the refined atomic models of the pseudo-cubic phases of $SrMO_2N$ (M = Nb, Ta) in tetragonal space group P4/mmm. The variables and atomic positions are as shown in Table 6.1.

M	Nb	Nb	Nb	Ta	Ta	Ta	Ta
T (℃)	300	400	500	200	350	500	750
χ^2	4.115	3.826	3.854	2.809	2.624	2.459	2.224
R_{wp}	0.0561	0.0541	0.0542	0.0525	0.0516	0.0504	0.0479
R_{F2}	0.0330	0.0308	0.0338	0.0363	0.0399	0.0438	0.0523
a (Å)	4.0541(1)	4.0575(0)	4.0610(2)	4.0441(2)	4.0493(1)	4.0535(3)	4.0618(2)
c (Å)	4.0511(3)	4.0552(0)	4.0589(5)	4.0421 (5)	4.0460(3)	4.0518(7)	4.0589(5)
Sr U_{iso} ($Å^2$)	0.0170(3)	0.0189(2)	0.0214(4)	0.0131(3)	0.0163(3)	0.0202(4)	0.0258(4)
M U_{iso} ($Å^2$)	0.0081(3)	0.0085(2)	0.0099(3)	0.0053(3)	0.0065(3)	0.0080(3)	0.0108(4)
X U_{iso} ($Å^2$)	0.0224(2)	0.0235(1)	0.0255(3)	0.0186(2)	0.0197(3)	0.0225(3)	0.0271(3)
X1 O/N occ.	0.535(19)/0.465	0.560(17)/0.440	0.575(26)/0.425	0.521(22)/0.479	0.533(23)/0.467	0.554(28)/0.446	0.544(26)/0.456
X2 O/N occ.	0.990(39)/0.010	0.939(34)/0.061	0.910(52)/0.09	0.959(44)/0.041	0.934(46)/0.066	0.891(57)/0.109	0.912(52)/0.088

900 °C) for this material,[6] showing that the anion order is highly robust.

Figure 6.5 The oxygen occupancies of the X1 site in the pseudo-cubic models at high temperatures.

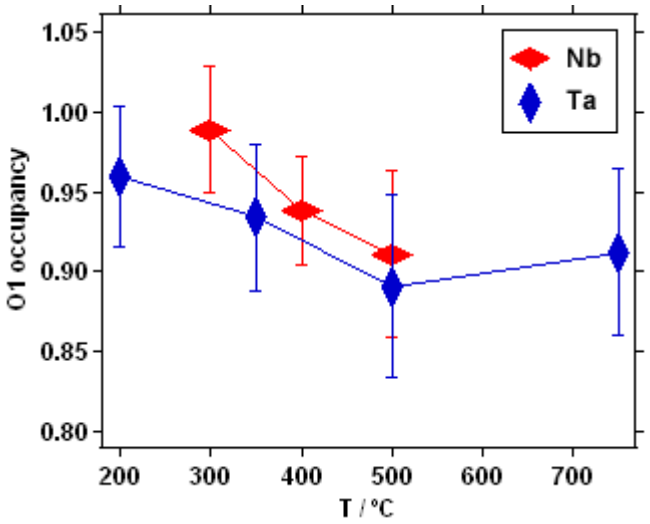

At room temperature, $SrNbO_2N$ and $SrTaO_2N$ adopt a rotationally ordered $\sqrt{2}a_p$ x $\sqrt{2}a_p$ x $2a_p$ perovskite superstructure (Figure 6.4). Rotation of the octahedra around a unique (*c*) axis creates two anion sites in a 1:2 ratio, with Y1 on the *c*-axis and Y2 in the *ab*-plane, and the M-Y2-M bridge is bent, with angle 168.5 ° from $SrNbO_2N$ refinement below. This superstructure is conventionally described by the tetragonal space group I4/mcm,[1-4] but the electron diffraction images of individual crystallites of $SrMO_2N$ (M = Nb, Ta) in Figure 6.6 consistently show the presence of very weak (h0l) and (0kl) h or k = odd reflections that should be systematically absent in I4/mcm. This lowering of symmetry may be associated with the anion ordering observed in the high temperature phase if this has an orientational relationship to the rotational order. The monoclinic space group I112/m was used in room temperature refinements to test the possibility of anion ordering, but the refined cell parameters and atom positions had to be constrained by tetragonal I4/mcm symmetry to give a stable refinement. For $SrNbO_2N$, occupancies at the three anion sites were refined independently, subject to the overall composition $SrNbO_{2.07}N_{0.93}$. This was not

possible for the $SrTaO_2N$ refinement and the two Y2 site occupancies were constrained to be equal and subject to the stoichiometry $SrTaO_{2.00}N_{1.00}$; this refinement is equivalent to an I4/mcm fit. The summary of refinement for $SrNbO_2N$ and $SrTaO_2N$ at room temperature is shown in Table 6.3.

Figure 6.6 Electron diffraction patterns showing the [100] and [010] zones from a representative crystallite of (a) $SrNbO_2N$ and (b) $SrTaO_2N$ at room temperature.

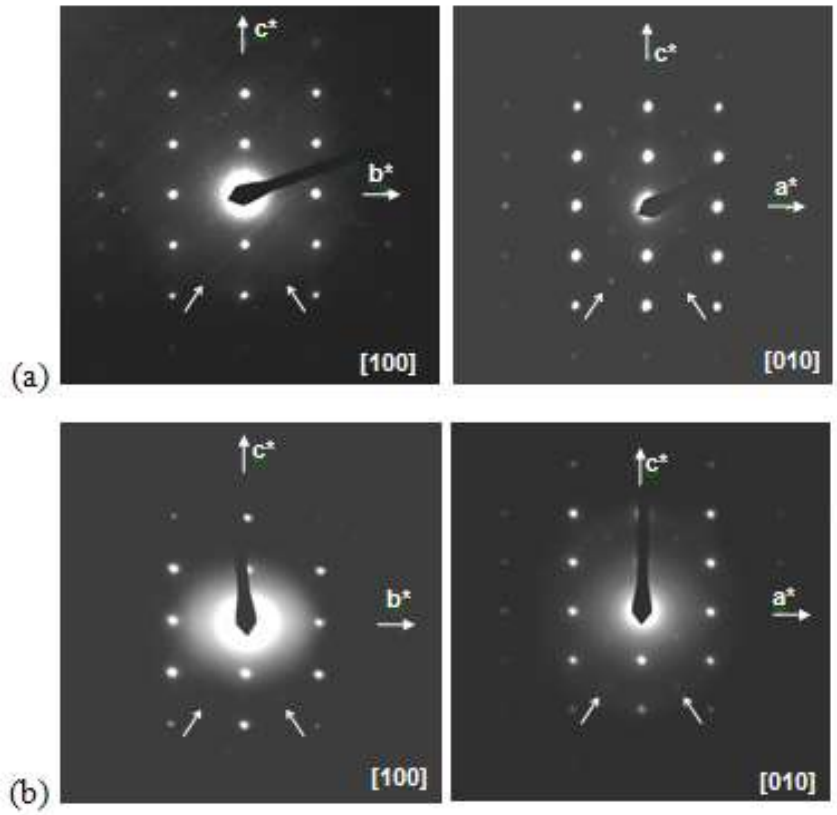

Table 6.3 Refined atomic model and selected bond distance/angles for $SrNbO_2N$ and (underneath in italics) $SrTaO_2N$ at room temperature.

Atom	x	y	z	U_{iso} (Å^2)	O/N occupancy
Sr	0	0.5	0.25	0.0094(4) *0.0085(4)*	
Nb1 *Ta1*	0	0	0	0.0069(3) *0.0039(4)*	
Nb2 *Ta2*	0	0	0.5	0.0069 *0.0039*	
Y1(X2)	0	0	0.25	0.0145(3) *0.0138(3)*	0.66/0.32 *0.48(4)/0.52*
Y2(X1)	0.7249(2) *0.7319(3)*	0.7751 *0.7681*	0	0.0145 *0.0138*	0.84(6)/0.16 *0.76/0.24*
Y2(X2)	0.7751 *0.7681*	0.2751 *0.2681*	0	0.0145 *0.0138*	0.57(6)/0.43 *0.76/0.24*

$SrNbO_2N$: a = b = 5.7077(2) Å, c = 8.1026(3) Å, γ = 90 °, χ^2 = 3.78, R_{wp} = 5.22 %, R_{F^2} = 3.78 %; *$SrTaO_2N$: a=b= 5.7063(2) Å, c= 8.0817(4) Å, γ = 90 °, χ^2 = 2.64, R_{wp} = 5.00%, R_{F^2} = 4.16%*.

	$SrNbO_2N$		$SrTaO_2N$	
Dis. (Å)	Sr_O/N2(Y1)×4	2.85385(7)	Sr_O/N2(Y1)×4	2.85312(8)
	Sr_O/N1(Y2)×4	2.7199(11)	Sr_O/N1(Y2)×4	2.7571(13)
	Sr_O/N1(Y2)×4	3.0059(12)	Sr_O/N1(Y2)×4	2.9568(14)
	<Sr_O/N>12	2.8598(1)	<Sr_O/N>	2.8556(1)
	Nb_O/N2(Y1) ×2	2.02565(6)	Ta_O/N2(Y1) ×2	2.02045(9)
	Nb_O/N1(Y2) ×4	2.02815(17)	Ta_O/N1(Y2) ×4	2.02241(14)
	<Nb_O/N>6	2.0273(1)	<Ta_O/N>6	2.0217(1)
Ang. (deg)	Sr_O/N1a(Y2)_Sr	96.28(5)	Sr_O/N1a(Y2)_Sr	94.24(6)
	Sr_O/N1a(Y2)_Sr	174.23(5)	Sr_O/N1a(Y2)_Sr	175.98(6)
	Sr_O/N1a(Y2)_Sr	89.494(5)	Sr_O/N1a(Y2)_Sr	89.774(5)
	Sr_O/N1a(Y2)_Sr	84.74(4)	Sr_O/N1a(Y2)_Sr	86.21(5)

Neutron refinement of the room temperature O/N occupancies in the I4/mcm model gave a near-50:50 population at the Y1 site, showing that this corresponds to one of the X2 sites in the high temperature structure. This implies that the two Y2 sites in the room temperature structure are not equivalent, as one is expected to correspond to the X1 site (100% O) and the other should be the remaining X2 (50:50 O:N) site, as shown in Figure 6.5. This lowers the space group symmetry from tetragonal I4/mcm to monoclinic I112/m (a non-standard setting of C2/m) and attempts were made to fit an I112/m model to the room temperature neutron data (Table 6.3). No stable monoclinic refinement was possible for $SrTaO_2N$, and the model shown is equivalent to an I4/mcm description with O:N ratios of 50:50 at the Y1 site and an average 75:25 at the two Y2 positions. The same distributions have been reported in a previous study of $SrTaO_2N$, and of $CaTaO_2N$ where further octahedral tilting lowers the apparent symmetry to orthorhombic $Pbnm^2$ and anion order is predicted to result in a monoclinic $P112_1/m$ structure. For $SrNbO_2N$, it was possible to refine the occupation factors of the three anion sites independently, subject to the fixed overall composition, and with lattice parameters and atomic positions constrained by I4/mcm symmetry. The results in Table 6.3 support the above expectation, with the Y2(X1) site having a high (87%) O occupancy while the Y2(X2) site has 51% O. This anion order leads to the loss of the c-glide plane symmetry observed in the electron diffraction patterns (Figure 6.6).

6.4 Discussion

According to the above refinements, a robust $1O:2(O_{0.5}N_{0.5})$ anion order is present over the three available sites for $SrMO_2N$ (M = Nb, Ta) up to at least 750 °C in the latter material. The anion order controls the ordering of octahedral rotations below ~200 °C, but the unique axis for anion order does not correspond to the unique axis for octahedral rotation in the room temperature structure. Although the anion order is

well-defined, it results in very small metric distortions of the high temperature $Pm\bar{3}m$ and room temperature I4/mcm structures. High resolution powder neutron diffraction data have enabled the high temperature P4/mmm (pseudo-cubic $Pm\bar{3}m$) structures to be refined freely, but this was not possible for the expected room temperature I112/m models which have I4/mcm pseudo-symmetry. Further improvements might be possible using higher resolution powder diffraction data, however, the O/N disorder over the two X2 sites results in an intrinsic strain broadening of diffraction peaks that may limit the achievable resolution.

The neutron diffraction results indicate that a robust partial anion order is present in the $SrMO_2N$ (M = Nb, Ta) perovskites over a wide temperature range, with oxide anions ordered on one axis of the pseudo-cubic cell while a 50:50 O:N mixture is present on the other two. This distribution is difficult to rationalize from electrostatic repulsions between O^{2-} and N^{3-}, but is consistent with a well-defined short range order driven by covalent effects as follows. Octahedral bis(imido) or dioxo complexes of high valent d^0 transition metal ions invariably adopt a *cis*- (90 °) configuration, e.g. in $Mo(NR)_2^{2+}$ or MoO_2^{2+} complexes,[7,8] and so the *cis*-configuration of the MN_2O_4 octahedra in the $SrMO_2N$ perovskites is expected to be more stable than the *trans*- (180 °) arrangement as nitride is more strongly bonded than oxide. This is supported by electronic structure calculations for $ATaO_2N$ which have shown that *cis*-ordered structures have lower energies, [9, 10] and by a pair distribution function analysis of the total neutron scattering from $BaTaO_2N$ which found *cis*-coordination to be more likely than *trans*.[11]

The *cis*-coordination of each M cation by two nitrides, and the linear or near-linear coordination of each nitride by two M cations, results in zig-zag -M-N- chains within the $SrMO_2N$ structures as represented in Figure 6.7. In an ideal, fully-ordered structure (Figure. 6.7(a)) the chains have a regular arrangement that would give rise

to an anion-ordered superstructure in the ab-plane. However, the zig-zag -M-N- chains, like those of organic polymers, are very susceptible to disorder as there are two choices for the 90 °turn at each M atom. This produces random chains and rings within the planes (Figure. 6.7(b)) and results in the average anion distribution observed in the neutron experiments, with an exact average 50:50 O:N composition at the X2 anion sites in the ab-plane due to the presence of two *cis*-nitrides at each M site. On heating (e.g. $SrTaO_2N$ at 750 ℃), the ~10% occupancy of the c-axis X1 site by nitride corresponds to the propagation of chains or rings between adjacent planes, as shown in Figure 6.7(c), and this could lead to complete randomization of the chains in all three dimensions at higher temperatures as shown in Figure 6.7(d). Hence, even a cubic AMO_2N perovskite with an average 67:33 O:N distribution at each site is expected to have well-defined local order with *cis*-MN_2O_4 octahedra at each site. Cubic superstructures of three-dimensionally ordered -M-N- chains are also possible although these may be difficult to realize.

Figure 6.7 Illustrations of *cis*-$(MX)_n$ (X = N,O) polymer formation arising from anion order in oxynitride perovskites. In (a) to (d), heavy lines correspond to M-N-M units in AMO_2N types or to M-O-M units in $AMON_2$ types.

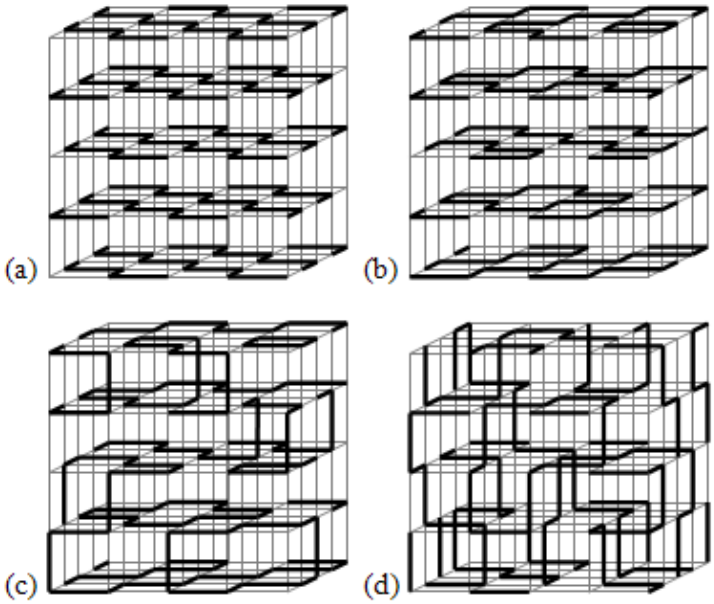

The above principle of local anion order driven by differing M-N and M-O bond strengths can be applied to predict local structures across the range of $AMO_{3-x}N_x$ perovskites. The preference for the more strongly bonded nitride ligands to be mutually *cis* results in a symmetry between nitride order in $AMO_{3-x}N_x$, and oxide order in the corresponding AMO_xN_{3-x} composition. For example, M-N covalency favours the *cis*-MN_2O_4 arrangement in AMO_2N, as described above, and also the *cis*-MN_4O_2 octahedral configuration for $AMON_2$. This is evident in coordination complexes such $MoO_2F_2(thf)_2$ [12] and $Mo(NC(CH_3)_3)_2Cl_2(py)_2$ [13] in which the two most strongly bonded anions (oxide or t-butylimido) are *cis*, as are the two most weakly bonded ligands (thf = tetrahydrofuran or py = pyridine). Hence, the representations of -M-N- chains in AMO_2N in Figure 6.7 are equally applicable to -M-O- chains in $AMON_2$. At x = 1.5, fac-MN_3O_3 octahedra are present, in which the three nitrides or oxides are mutually cis, by analogy with the fac-configuration observed in isolated $[MoO_3F_3]^{3-}$ complexes.[14] The fac-MN_3O_3 octahedra produce interpenetrating -M-N- and -M-O- networks of cis-crosslinked cis-chains in $AMO_{1.5}N_{1.5}$ perovskites. A summary of situations with different O/N ratio in $AMO_{3-x}N_x$ perovskites is shown in Figure 6.8.

Figure 6.8 The degree of polymerization of M-X-M units and the local coordinations around M cations for the range of $AMO_{3-x}N_x$ perovskites.

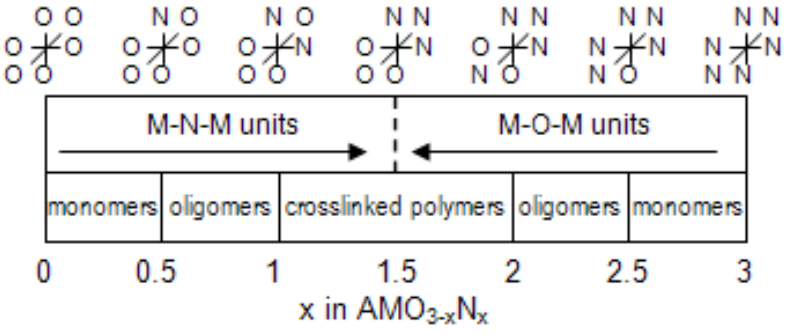

6.5 Conclusions

Structural studies of $SrMO_2N$ (M = Nb, Ta) have been performed using electron and variable temperature neutron diffraction. Partial anion order has been observed up to 750 ^oC and is consistent with *cis*-ordering of the two nitrides in each MO_4N_2 octahedron. At low temperatures, this order directs the tilting of the octahedron to form a pseudo-tetragonal superstructure. It also creates disordered zig-zag MN chains in two or three dimensions within the lattice. This principle can be used to predict the local structures of perovskite-related oxynitrides $AMO_{3-x}N_x$.

This research has led to the following publication:

Minghui Yang, J. Oró-Solé, J. A. Rodgers, A. B. Jorge, A. Fuertes and J. Paul Attfield, Anion Order in Perovskite Oxynitrides, *Nature Chemistry* 2010, Submitted.

6.6 Reference

1. S. G. Ebbinghaus, H. P. Abicht, R. Dronskowski, T. Müller, A. Reller and A. Weidenkaff, *Prog. Solid State Chem.* 2009, 37, 173.
2. E. Gunther, R. Hagenmayer and M. Jansen, *Z. Anorg. Allg. Chem.* 2000, 626, 1519.
3. S. J. Clarke, K. A. Hardstone, C. W. Michie and M. J. Rosseinsky, *Chem. Mater.* 2002, 14, 2664.
4. S. G. Ebbinghaus, A. Weidenkaff, A. Rachel, and A. Reller, *Acta Cryst.* 2004, 60c, i91.
5. A. C. Larson and R. B. von Dreele, "General Structure Analysis System (GSAS)", Los Alamos National Laboratory Report LAUR 86-748 (1994)
6. Y. Kim, P. M. Woodward, K. Z. Baba-Kishi, and C. W. Tai, *Chem. Mater.* 2004, 16, 1267.
7. K. Tatsumi and R. Hoffmann, *Inorg. Chem.* 1980, 19, 2656.
8. P. Barrie, T. A. Coffey, G. D. Forster and G. Hogarth, *J. Chem. Soc. Dalton Trans.* 1999, 4519.
9. C. M. Fang, J. A. de Wijs, E. Orhan, G. de With, R. A. de Groot, H. T. Hintzen and R. Marchand, *J. Phys. Chem. Solids* 2003, 64, 281.
10. H. Wolff, and R. Dronskowski, *J. Comput. Chem.* 2008, 29, 2260.
11. K. Page, M. W. Stoltzfus, Y-I. Kim, T. Proffen, P. M. Woodward, A. K. Cheetham, and R. Seshadri, *Chem. Mater.* 2007, 19, 4037.
12. M. Rhiel, S. Wocadlo, W. Massa and K. Dehnicke, *Z. fuer Anorg. und Allg. Chem.* 1996, 622, 1195.
13. H-T. Chiu, G-B. Chang, W-Y. Ho, S-H. Chuang, G-H. Lee, and S-M. Peng, *J. Chin. Chem. Soc.* 1994, 41, 755.
14. F. J. Brink, L. Noren, D. J. Goossens, R. L. Withers, Y. Liu and C. N. Xu, *J. Solid State Chem.* 2003, 174, 450.

Chapter 7. Conclusions

In this thesis, three new series of oxynitrides have been synthesized by using both conventional thermal ammonolysis and high pressure high temperature (HPHT) methods. A range of structure types including perovskite, scheelite and pyrochlore has been studied by X-ray, electron and neutron diffraction experiments. A variety of properties including magnetic order, mixed-valent behaviour, semiconductivity, optical properties and colossal magnetoresistances (CMR) have been observed. A general anion ordering principle for oxynitride perovskites has been derived based on a neutron diffraction study of O/N order in the typical oxynitride perovskites $SrMO_2N$ (M = Nb, Ta).

A wide range of $EuWO_{1+x}N_{2-x}$ materials ($-0.16 \leq x \leq 0.46$) has been synthesized by thermal ammonolysis of a $Eu_2W_2O_9$ precursor. A new oxynitride $EuWO_{4-y}N_y$ with the scheelite structure has been discovered as an intermediate phase, with slight mixed-valency and colours ranging from light yellow to deep orange. The overall ammonolysis reaction has emerged as $Eu_2W_2O_9 \rightarrow EuWO_{4-y}N_y \rightarrow EuWO_{1+x}N_{2-x}$. The effects of reaction condition have been studied and mapped out based on the correlation with the N content. Ferromagnetic ordering was found in all the samples below $T_C = 12 \pm 1$ K. Large negative magnetoresistances were found in all the perovskite samples. In particular, for the lowest doping sample, $EuWO_{0.96}N_{2.04}$, CMR $\geq$ 99.7% was observed at 7 K, and this material shows high low field magnetoresistance of 13% of at 0.1 T and 8 K. The variation of the physical properties with the chemical composition has been determined.

The high pressure high temperature (HPHT) method has been employed to

synthesize new oxynitride perovskites - $RZrO_2N$ (R = Pr, Nd and Sm). These materials are potentially multiferroic as they contain both magnetic R^{3+} and d^0 Zr^{4+}. They are synthesized at temperatures from 1200 to 1500 ^oC and pressures of 2 – 3 GPa. Powder X-ray diffraction shows that the $RZrO_2N$ phases have a distorted perovskite structure in orthorhombic space group Pnma. The structural distortion increases as the R^{3+} ionic radius decrease. This result demonstrates the synthesis of oxynitride perovskites using HPHT methods for the first time. However, the best material out of more than twenty syntheses is only approximately 70% pure and contains a very stable secondary pyrochlore phase. Hence, conducting and magnetic properties measurements were not made on these new phases. Crucial future work will be to make pure samples and to undertake physical property studies.

A further exploration of new oxynitrides has been made in the Eu-Mo-O-N system. There is no evidence of new oxynitride phases from ammonolysis of $EuMoO_4$ at temperatures from 550 – 1000 ^oC for reaction times of 3 – 12 hr. However, a new series of oxynitrides $Eu_2Mo_2O_{6-x}N_{2+2x/3}$ ($0.20 \leq x \leq 2.25$) has been synthesized by ammonolysis of $Eu_2Mo_2O_7$ at temperatures ranging between 500 to 630 ^oC for 12 hr. Powder X-ray diffraction shows the polycrystalline samples crystallize in the pyrochlore structure with the space group $Fd\bar{3}m$. According to chemical analysis results and magnetization measurements, both metals are in their maximum oxidation states of Eu^{3+} and Mo^{6+}. The cubic lattice parameter increases linearly with x. Semiconductor behaviour has been observed in these samples, with a band gap of 61 meV for $Eu_2Mo_2O_{4.33}N_{3.11}$. These samples appear to show ferrimagnetic ordering below $T_C = 8 \pm 1$ K.

A detailed Rietveld analysis was made on constant wavelength neutron diffraction patterns of the representative perovskites $SrMO_2N$ (M = Nb, Ta). This has revealed a robust 1O: $2(O_{0.5}N_{0.5})$ partial anion order up to at least 750 ℃ in the apparently cubic

high temperature phases, and this directs the rotations of MO_4N_2 octahedra in the room temperature superstructure. The anion distribution is consistent with local cis-ordering of the two nitrides in each octahedron driven by covalency, resulting in disordered zig-zag MN chains in planes within the perovskite lattice. Local structures for the range of $AMO_{3-x}N_x$ perovskites are predicted using the same principles.

In conclusion, this body of work demonstrates that both conventional ammonolysis and HPHT methods can be used to synthesis oxynitrides, as appropriate for the structure types of the target compounds. In the ammonolysis process, the ammonia can act as a simultaneous reducing and nitriding agent, or can bring about one of these changes, which may lead to a phase transformation with or without a re-arrangement of cations. The substitution of O^{2-} by N^{3-} can strongly alter the oxidation states of metals, the cation and anion arrangement in the crystal structure and metal-anion bonding, resulting in various useful and interesting physical properties.